

AD-A283 808



**A Study on the Wedge Cutting Force through Longitudinally Stiffened Plates:
An Application to Grounding Resistance of Single and Double Hull Ships**

by

Mark Douglas Bracco

B.A. Mathematics, San Jose State University, 1985

Submitted to the Department of Ocean Engineering and
the Department of Mechanical Engineering
in Partial Fulfillment of the Requirements for the Degrees of

NAVAL ENGINEER
and
MASTER OF SCIENCE IN MECHANICAL ENGINEERING
at the
MASSACHUSETTS INSTITUTE OF TECHNOLOGY
May 1994



© Mark Douglas Bracco. All rights reserved.

The author hereby grants to MIT and the U.S. Government permission to reproduce and to
distribute publicly paper and electronic copies of this thesis document in whole or in part.

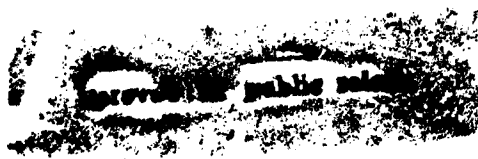
Signature of Author.....*Mark D. Bracco*.....
Department of Ocean Engineering
May 1994

Certified by.....*Tomasz Wierzbicki*.....
Tomasz Wierzbicki, Professor of Applied Mechanics
Thesis Supervisor

Certified by.....*Frank A. McClintock*.....
Frank A. McClintock, Professor of Mechanical Engineering
Thesis Reader

Accepted by.....*A. Douglas Carmichael*.....
A. Douglas Carmichael, Chairman Department Graduate Committee
Department of Ocean Engineering

Accepted by.....*Ain A. Sonin*.....
Ain A. Sonin, Chairman Department Graduate Committee
Department of Mechanical Engineering



94-27376
7998
181

94 8 25 1 8 1

A Study on the Wedge Cutting Force through Longitudinally Stiffened Plates: For
An Application to Grounding Resistance of Single and Double Hull Ships A&I

by

Mark Douglas Bracco

Submitted to the Department of Ocean Engineering and
Department of Mechanical Engineering on May 6, 1994
in partial fulfillment of the requirements for the degrees of
Naval Engineer and Master of Science in Mechanical Engineering

ABSTRACT

This paper studies the cutting by a wedge of longitudinally stiffened plates for application to the grounding resistance of single hull and double hull ships. Two types of ship hull designs were used as prototypes for the development of small scale models: a conventional longitudinally stiffened Single Hull (SH) and the Unidirectionally Stiffened Double Hull (USDH) design.

To model the cutting experiments, the complex deformation patterns observed in the damaged specimens were simplified to obtain a closed-form upper bound for the steady-state cutting force required for the USDH specimen. An existing closed-form upper bound solution, developed by Wierzbicki and Thomas, for the wedge cutting initiation force of a single plate was applied to the longitudinally stiffened single hull specimens by smearing the geometry to obtain an equivalent thickness single plate.

A total of eleven cutting experiments were conducted using six different wedge geometries.

The USDH steady-state cutting force solution was 6% above to 12% below the experimental mean steady-state force. The absolute average error is 5%.

The theoretical work required in cutting (at a distance of 0.25 m) of Wierzbicki and Thomas' initiation solution was 12% above to 4% below compared to the SH experiments. The absolute average error is 6%.

The results show that simplified closed-form solutions can be developed to estimate the force required in tearing a model that represents, with added realism, a ship hull in a grounding accident.

Thesis Supervisor: Dr. Tomasz Wierzbicki

Title: Professor of Applied Mechanics, Department of Ocean Engineering

DTIC TAB	
Unannounced	
Justification	
By	
Distribution /	
Availability Codes	
Dist	Avail and / or Special
A-1	

ACKNOWLEDGMENT

I would like to extend my gratitude to the U.S. Navy for the opportunity to further my education. This has been the fulfillment of a long-held goal.

A very special thanks are due to Professors Wierzbicki and McClintock for their patience and support, and for the many hours spent in their offices guiding me through this research. I have gained much insight into problem solving and engineering in the year I have worked them. They are truly leaders in their fields.

Thanks to the experimental team, Mohamed Yahiaoui, Pat Little, and Karrie Trauth for their help in the lab. A special thank you to Mohamed Yahiaoui for his leadership of the experimental team. He laid the groundwork, and graciously handed over to me his research efforts into the USDH model construction techniques.

Thanks to Teresa Coates for administrative support. Behind every organization, there is that one person that keeps things going. She did it to perfection.

I could not have done the experiments without the help of Arthur and Steve Rudolph. Their timely response and good ideas always helped save the day. They are not just machinists, they are artisans. They should take deep pride in the quality of their work.

Thanks to my 13A classmates for three of the most rewarding years in my naval career. Never again, could there be such a concentration of type-A personalities in one class!

To my office mate, Francis Colberg: thanks for listening. Over the last three years, we solved half of the world's problems and identified the other half.

I would not have been here had it not been for the support and mentoring of Jim Wicks, CDR, USN (retired). MIT was everything he said it was, and more.

My deep love and respect to my parents. They instilled in me perseverance and commitment. I could not have made it this far without these and the many other things they taught me.

Finally, and most importantly, to my family: We made it! I would not have survived this experience without the love, kindness, understanding, and good humor that my wife, Shona, unselfishly gave for three years, and the smiles and unconditional love that my boys, Alexander and Nicholas, always had waiting for me. Words cannot describe the love I have for my family.

Dedicated to

Shona, Alexander, and Nicholas.

Table of Contents

List of Figures	9
List of Tables	14
Nomenclature	15
Chapter 1. Background and Research Objectives	19
1.1 Background	19
1.2 Grounding Scenario	20
1.3 Theoretical Background of Ship Hull Damage Prediction Due to Grounding	21
1.4 Evolution of MIT Plate Cutting Experiments	27
1.5 Research Objectives	29
Chapter 2. Experimental Models and Apparatus	31
2.1 Ship Structural Design Considerations	31
2.2 Determination of Scale Model Geometry	33
2.2.1 Double Hull Model	33
2.2.2 Single Hull Model	35
2.3 Fabrication of the Hull Models	38
2.3.1 Welding Technique Selection	39
2.4 Wedge Geometry and Fabrication	41
2.5 Experimental Apparatus	42
Chapter 3. Experimental Results and Observations	53
3.1 Preparation of the Instron Universal Test Machine	53

3.2	Summary of Experimental Results	54
3.3	Discussion of Experimental Results	55
3.3.1	Double Hull Tests	55
3.3.2	Single Hull Tests	59
Chapter 4.	Theoretical Models and Comparison to Experimental Results	76
4.1	General Solution Approach	76
4.1.1	USDH Solution	81
4.1.1.1	Internal Work Rate in Bending	84
4.1.1.2	Internal Work Rate in Membrane Stretching	84
4.1.1.3	Internal Work Rate in Membrane Shear	86
4.1.1.4	Concertina Tearing Force	87
4.1.1.5	Contribution of Friction	88
4.1.1.6	Total Steady State Cutting Force	89
4.2	Application of Existing Solutions to the Longitudinally Stiffened Single Hull	90
4.2.1	Wierzbicki and Thomas' Plate Tearing Initiation Solution	91
4.2.2	Zheng and Wierzbicki's Steady-State Plate Cutting Solution	92
4.3	Comparison of Experiments to Theory	92
4.3.1	USDH Comparison	92
4.3.2	Single Hull Comparison	96
4.4	Parametric Study of the USDH Steady-state Cutting Force Solution	98

4.5 Alternative Failure Modes Assuming USDH Weld Failure	99
Chapter 5. Conclusions and Recommendations for Future Work	122
5.1 Conclusions	122
5.2 Recommendations for Future Work	124
References	128
Appendix A. Operation of the Test Equipment	131
A.1 Instron Universal test Machine Switch Lineup	131
A.2 Data Acquisition Program Lineup	132
A.3 Equipment Calibration	133
A.3.1 Setting the Chart Speed	134
A.4 Starting the Experiment	134
A.5 Data Reduction	135
Appendix B. Supporting Calculations	137
B.1 Calculation of Displacements u_x and u_y	137
B.2 Evaluation of the USDH Steady-State Cutting Force Equation	140
B.3 Fully Plastic Torsion of the Stiffener and Bending of the Stiffener and Plate	141
B.3.1 Fully Plastic Torsion of the Stiffener	142
B.3.2 Fully Plastic Bending Moment of the Stiffener, Plate, and Stiffener/Plate Combination	144
Appendix C. Tensile Test Results	149
Appendix D. Lazy-T Test Results	158

D.1 Purpose	158
D.2 Limit Load Calculation	158
D.3 Test Results	160
D.4 Lazy-T Test Conclusions	161

List of Figures

1.1 Plate Cutting by a Wedge	30
2.1 Concept of Unidirectionally Stiffened Double Hull (USDH) and Single Hull (SH) VLCC Midship Sections	44
2.2 USDH Model Geometry	45
2.3 T-Stiffener/Plate Combination	46
2.4 Longitudinally Stiffened Single Hull Model Geometry	47
2.5 Fillet Method of Welding the USDH Model	48
2.6 Possible Defect of Electron Beam Welding of T-Stiffener	48
2.7 Geometry of Wedges	49
2.8 Schematic of 20 kip Instron Universal Test Machine and Data Acquisition System	50
2.9 Specimen Test Fixture	51
2.10 Wedge-to-Load Cell Adapter	52
3.1 Test No. 1 (USDH, Wedge #1, $\theta=45^\circ$, Sharp Tip) - Photograph and Force-Displacement Graph	63
3.2 Test No. 2 (USDH, Wedge #2, $\theta=45^\circ$, 3/8 in. Radius Tip) - Photograph and Force-Displacement Graph	64
3.3 Test No. 3 (USDH, Wedge #3, $\theta=30^\circ$, Sharp Tip) - Photograph and Force-Displacement Graph	65
3.4 Test No. 4 (USDH, Wedge #4, $\theta=30^\circ$, 3/8 in. Radius Tip) - Photograph and Force-Displacement Graph	66
3.5 Test No. 5 (USDH, Wedge #5, Cylindrical) - Photograph and Force-Displacement Graph	67

3.6 Test No. 6 (USDH, Wedge #6, 3/4 in. Wide, $\theta=45^\circ$, 3/32 in. Radius Tip) - Photograph and Force-Displacement Graph	68
3.7 Test No. 7 (SH, Wedge #1, $\theta=45^\circ$, Sharp Tip) - Photograph and Force-Displacement Graph	69
3.8 Test No. 8 (SH, Wedge #2, $\theta=45^\circ$, 3/8 in. Radius Tip) - Photograph and Force-Displacement Graph	70
3.9a Test No. 9a (SH, Wedge #3, $\theta=30^\circ$, Sharp Tip) - Photograph and Force-Displacement Graph	71
3.9b Test No. 9b (SH, Wedge #3, $\theta=30^\circ$, Sharp Tip) - Photograph and Force-Displacement Graph	72
3.10 Test No. 10 (SH, Wedge #5, Cylindrical) - Photograph and Force-Displacement Graph	73
3.11 Test No. 11 (SH, Wedge #6, 3/4 in. Wide, $\theta=45^\circ$, 3/32 in. Radius Tip) - Photograph and Force-Displacement Graph	74
3.12 Wedge Adapter Modification	75
4.1 Decoupling the Yield Locus - Actual and Idealized (only one quadrant shown)	101
4.2 USDH Deformation Model	102
4.3 Material Element Undergoing Deformation Around Wedge	103
4.4 Plan View of USDH Wedge Cutting Process	104
4.5 Deformation Mechanisms	105
4.6 Material Element Undergoing Bending	106
4.7 Detailed Region of Membrane Stretching	107
4.8 Deformation Process for Membrane Stretching	108
4.9 Shearing of Plate for Kinematic Admissibility	109

4.10 Test No. 1 (USDH, Wedge #1, $\theta=45^\circ$, Sharp Tip) - Comparison of Experiment and Theory (Force- and Work-Displacement Graphs)	110
4.11 Test No. 2 (USDH, Wedge #2, $\theta=45^\circ$, 3/8 in. Radius Tip) - Comparison of Experiment and Theory (Force- and Work-Displacement Graphs)	111
4.12 Test No. 3 (USDH, Wedge #3, $\theta=30^\circ$, Sharp Tip) - Comparison of Experiment and Theory (Force- and Work-Displacement Graphs)	112
4.13 Test No. 4 (USDH, Wedge #4, $\theta=30^\circ$, 3/8 in. Radius Tip) - Comparison of Experiment and Theory (Force- and Work-Displacement Graphs)	113
4.14 Test No. 5 (USDH, Wedge #5, Cylindrical) - Comparison of Experiment and Theory (Force- and Work-Displacement Graphs)	114
4.15 Work-Displacement Graph Showing Transition from Initiation to Steady State Cutting	115
4.16 Test No. 7 (SH, Wedge #1, $\theta=45^\circ$, Sharp Tip) - Comparison of Experiment and Theory (Force- and Work-Displacement Graphs)	116
4.17 Test No. 8 (SH, Wedge #2, $\theta=45^\circ$, 3/8 in. Radius Tip) - Comparison of Experiment and Theory (Force- and Work-Displacement Graphs)	117
4.18 Test No. 9b (SH, Wedge #3, $\theta=30^\circ$, Sharp Tip) - Comparison of Experiment and Theory (Force- and Work-Displacement Graphs)	118
4.19 Test No. 10 (SH, Wedge #5, Cylindrical) - Comparison of Experiment and Theory (Force- and Work-Displacement Graphs)	119
4.20 Effect of Wedge Width on USDH Cutting Force (Equation 4.41)	120
4.21 Effect of Wedge Semi-angle on USDH Cutting Force (Equation 4.41)	120
4.22 Effect of Coefficient of Friction on USDH Cutting Force (Equation 4.41)	121
4.23 Effect of Plate Thickness on USDH Cutting Force (Equation 4.41)	121
5.1 Deformation and Fracture Modes of T-Joints	127

B.1 Geometry for Calculation of Displacements u_a and u_b	147
B.2 Sand Heap Analogy for Stiffener	148
C.1 ASTM A370 Flat Tensile Specimen	151
C.2 Specimen 1 - Engineering Stress-Strain Curve ($t = 0.749$ mm, 0° from roll axis)	152
C.3 Specimen 2 - Engineering Stress-Strain Curve ($t = 0.749$ mm, 0° from roll axis)	152
C.4 Specimen 3 - Engineering Stress-Strain Curve ($t = 0.749$ mm, 90° from roll axis)	153
C.5 Specimen 4 - Engineering Stress-Strain Curve ($t = 0.749$ mm, 90° from roll axis)	153
C.6 Specimen 5 - Engineering Stress-Strain Curve ($t = 1.130$ mm, 90° from roll axis)	154
C.7 Specimen 6 - Engineering Stress-Strain Curve ($t = 1.130$ mm, 90° from roll axis)	154
C.8 Specimen 7 - Engineering Stress-Strain Curve ($t = 1.130$ mm, 0° from roll axis)	155
C.9 Specimen 8 - Engineering Stress-Strain Curve ($t = 1.130$ mm, 0° from roll axis)	155
C.10 Specimen 9 - Engineering Stress-Strain Curve ($t = 1.829$ mm, 0° from roll axis)	156
C.11 Specimen 10 - Engineering Stress-Strain Curve ($t = 1.829$ mm, 0° from roll axis)	156
C.12 Specimen 11 - Engineering Stress-Strain Curve ($t = 1.829$ mm, 90° from roll axis)	157
C.13 Specimen 12 - Engineering Stress-Strain Curve ($t = 1.829$ mm, 90° from roll axis)	157

D.1 T-Stiffener Geometry and Free Body Diagram	162
D.2 Bending Moment at the Web Joint	163
D.3 Lazy-T Test Results for Specimen #1	164
D.4 Lazy-T Test Results for Specimen #2	164
D.5 Lazy-T Test Results for Specimen #3	165

List of Tables

2.1 USDH Model Cell Size Options	35
2.2 VLCC Prototype Stiffener and Plate Dimensions	36
2.3 Stiffener/Plate Thickness Ratios for VLCC Prototype and Model	37
2.4 Single Hull Model and Plate Dimensions	38
2.5 Geometry of Wedges	42
3.1 Summary of Cutting Experiments Results	55
4.1 Comparison of USDH Experiments and Theory	95
4.2 Comparison of Single Hull Experiments and Theory	97
4.3 Force Level Comparison for Alternative USDH Failure Modes	100
5.1 Contribution of Membrane, Bending, and Friction of the USDH Steady-State Cutting Force Solution (not including concertina tearing)	123
A.1 Instron Universal Test Machine Switch Settings	131
B.1 USDH Steady-State Cutting Force Equation Values	141
B.2 Fully Plastic Moments of Stiffener and Plate Structural Members	146
C.1 Tensile Test Specimen Properties	149
C.2 Tensile Test Specimen Averaged Properties	150
D.1 T-Stiffener Dimensions	160

Nomenclature

Chapter 1:

δ_i	Crack opening displacement (COD)
$\bar{\delta}_i$	Dimensionless COD parameter
α, β	Unknown exponents determined experimentally
μ	Friction coefficient
ϕ	plate tilt angle
θ	Wedge semi-angle
σ_o	Material flow stress
σ_y	Yield stress
a, b	Experimentally determined constants
A	Area of deformed plate, $A = l^2 \tan \theta$
A_s	Total area of tearing, $A_s = p_s t_s$
B	Wedge width
C	Experimentally determined dimensionless constant
E	Energy per unit volume of displaced material
F_c	Plate cutting force
F_{ss}	Steady-state cutting force
F_t	Plate tearing force
K_T	Kinetic energy
l, p_s	Depth of penetration of wedge into plate
M_o	Fully plastic bending moment
R_T	Resistance factor
S	Energy function per unit length
t, t_s	Thickness of plating
u	Distance of wedge travel
V_s	Volume of displaced material, $V_s = p_s^2 t_s \tan \theta$
W	Total work in cutting a plate
W_B	Work in bending a plate
W_C	Work in cutting of a plate
W_D	Work of bending, membrane, and shear
W_F	Work due to friction
W_s	Total work to penetrate a side structure by a wedge shaped bow
\dot{W}_b	Rate of bending work
\dot{W}_m	Rate of membrane work

Chapter 2:

θ	Wedge semi-angle
b	Longitudinal Spacing
b_f	Width of flange
b_w	Height of web
h	USDH longitudinal girder height
I_M	Moment of inertia of model plate and stiffener
I_{pM}	Moment of inertia of model plate
I_{pVLCC}	Moment of inertia of prototype plate
I_{VLCC}	Moment of inertia of prototype plate and stiffener
N	Number of cells in USDH model
t, t_p	Plate thickness
t_f	Flange thickness
t_w	Web thickness
w	Effective width of test specimens

Chapter 3:

θ	Wedge semi-angle
r	Wedge tip radius

Chapter 4:

$\bar{\delta}_i$	Dimensionless COD parameter
$\dot{\theta}_i$	i^{th} stationary hinge rotation rate
μ	Friction coefficient
Δ	Lateral distance of USDH plate deformation
ζ	Progressive wedge cutting distance
θ	Wedge semi-angle
$\kappa_{\alpha\beta}$	Curvature tensor ($\alpha, \beta=1,2$)
α_1, α_2	New angles of deformed material in USDH cutting
η_1	Stationary bending hinge line 1
η_2	Stationary bending hinge line 2
ϵ_{ave}	Average strain in USDH cutting model
ϵ_b	Strain in bending
ϵ_{ij}	General strain tensor ($i,j=1,2,3$)
ϵ_{sh}	Strain in shear
ϵ_{str}	Strain in stretching

σ_{ij}	General stress tensor
σ_o	Material flow stress
σ_{oF}	Material flow stress of flange
σ_{oP}	Material flow stress of plate
σ_{oW}	Material flow stress of web
(ξ, η)	Local coordinate system
A	Cross sectional area of stiffener
A_F	Area of flange
A_W	Area of web
b	Longitudinal spacing
B	Wedge width
F	Total steady-state force for USDH cutting
$F_{concertina}$	Concertina tearing force
F_{exp}	Instantaneous experimental force level
F_i	General applied forces
F_m	Experimental mean force level
F_p	Internal force due to plastic work
F_{pf}	Internal force of plastic work and friction
F_t	Tearing force
l	Length of wedge cut
l_i	Length of i^{th} plastic hinge line
l_f	Final length of cut
l^*	Transition from initiation to steady-state cutting
$M_{\alpha\beta}$	General bending moment
M_o	Fully plastic bending moment
$N_{\alpha\beta}$	General force
N_o	Fully plastic force
R	Fracture parameter (fracture toughness)
r_1	Radius of bending about stationary hinge η_1
r_2	Radius of bending about stationary hinge η_2
t, t_p	Plate thickness
t_{eq}	Smear. equivalent plate thickness
u_a, u_b	USDH model displacements
u_i	General displacements
V	Velocity of material element
\dot{W}_b	Bending work rate
\dot{W}_{ext}	External work rate
\dot{W}_{int}	Internal work rate
\dot{W}_m	Membrane work rate
\dot{W}_{sh}	Membrane shear work rate

\dot{W}_{str}	Membrane stretching work rate
W_{ss}	Work in steady-state cutting
W_t	Work in plate tearing

Abbreviations

EBW	Electron beam welding
HAZ	Heat affected zone
LBP	Length between perpendiculars
NSWC	Naval Surface Warfare Center
SH	Longitudinally stiffened single hull
USDH	Unidirectionally stiffened double hull
VLCC	Very large crude carrier

Chapter 1

Background and Research Objectives

1.1 Background

The March 1989 grounding of the supertanker, *Exxon Valdez*, in the pristine waters of Prince William Sound, Alaska resulted in the loss of nearly 11 million gallons of crude oil. This accident provided the impetus for action in the prevention of oil spills in an effort to protect the environment. The United States Congress passed the *Oil Pollution Act of 1990* (OPA 90) mandating that petroleum product cargo ships operating in U.S. waters will be of double hull construction (or designs providing equivalent protection) by January 1, 2015. A recent U.S. Coast Guard Report to Congress (1992) concluded that there are currently no suitable equivalent designs to the double hull tanker for the prevention of oil outflow due to grounding.

While a significant amount of research over the past three decades has been conducted on the structural response of ships due to collisions, it has only been in the past fifteen years or so that structural damage due to ship grounding accidents has been investigated. Early work in grounding prediction has been to perform plate cutting experiments which produced empirical formulas for the work to cut a flat plate. More recently studies of the kinematics of plate cutting have resulted in closed form expressions for upper bound solutions for the plate cutting force. These efforts have been quite significant in quantifying the force required to cut a single plate, but do not account for the effects of stiffeners and inner hull that exist in the actual geometry of ships.

In order to adequately predict the lift and drag forces in a ship undergoing a grounding accident and the subsequent extent of damage, further research is required to

account for the interaction of ship structural members with one another. This has provided the motivation for the work contained herein. This research supports the *Joint MIT-Industry Program on Tanker Safety* project. The ultimate goal of the project is to provide to the industry a computer program that will assist the ship designer/owner in assessing the survivability (by predicting a length of damage) of a particular design or existing ship as it undergoes a grounding accident. The overall approach to the project in meeting this final goal is:

- Study actual grounding accidents,
- Determine the predominate failure modes,
- Develop computational models of the failure modes leading to closed form solutions,
- Conduct small scale experiments to reproduce the failure modes and validate theoretical solutions,
- Finally, combine the results into a damage assessment computer program.

1.2 Grounding Scenario

A grounding model of longitudinally framed Very Large Crude Carrier (VLCC) ships has been developed by Wierzbicki, Peer, and Rady (1993). They identified four basic mechanisms that account for the energy dissipated during the grounding:

- global lifting of the ship against gravitational forces,
- friction forces between the bottom hull plating and the grounding surface,
- plastic deformation of the hull girder, and
- forces required to fracture the hull structure.

In grounding, the ship initially lifts and rides over the rock causing only hull indentation. Once the force due to the weight of the ship overcomes the plating membrane strength, the hull plating ruptures. Kinetic energy of the ship is given up to friction forces, plastic deformation, and fracture as tearing over a length of the hull plating ensues. The work in this thesis does not account for the lifting and subsequent rupture of the ship, but assumes that the tearing of the hull plating is well progressed. The indentation and rupture of a ship hull subjected to a vertical load is considered a separate mechanism and has been investigated by Thunes (1993).

1.3 Theoretical Background of Ship Hull Damage Prediction due to Grounding

The literature is consistent in crediting Minorsky (1959) with the pathfinding work in the area of structural damage prediction due to ship collisions. His approach, as summarized by Jones (1983), was to use the conservation of momentum for the inelastic collision of two ships. Minorsky was able to develop an empirical relationship between the loss of kinetic energy, K_T , and the resistance factor (relating the volume of damaged material), R_T , by correlating the data for 26 ship collisions. The straight line relation of Equation 1.1 fits the data.

$$K_T = 414.5 R_T + 121900 \quad (1.1)$$

R_T and K_T have units of ft²-in and lton-knot², respectively. This relationship holds quite accurately for collisions where K_T is large. However, it does not hold well for minor collisions where K_T is small and the damage is relatively minor.

It is from this study that others have progressed into the area of grounding damage. Vaughan (1978) developed empirical equations relating damage to absorbed energy for ship collisions, and then extended that work for grounding damage. He postulated that in the side collision of a ship by a wedge shaped bow there are two independent contributions of work. Some of the work goes to distorting the volume of material and the remaining in fracture of an area of plate. The bow is idealized as a wedge that cuts into plating representing a side deck structure as shown in Figure 1.1. He determined that there are six independent variables describing the physics of the problem, with two fundamental dimensions, force and cut distance, which are expressed functionally in Equation 1.2.

$$F(W_s, S, E, p_s, \theta, t_s) = 0 \quad (1.2)$$

Using dimensional analysis, Vaughan was able to derive a relationship for total work to penetrate the side of a ship. Equation 1.3 holds for steel structures where the first term relates to the work in fracturing an area of plate, A_s , and the second for work in bending and stretching a volume of plate, V_s .

$$W_s = aA_s + bV_s \quad (1.3)$$

The constants, a and b , were determined by using experimental results of bow structures penetrating into transversely framed side structures. Vaughan was able to measure A_s and V_s , deduce $b=9.5$ tonf/m-mm from R_T in Minorsky's formula, and thus determine $a=3.4$ tonf/mm. For ship collisions, Equation 1.3 correlates very well to Equation 1.1. In grounding, the volume distortion of the plate is small, thereby setting V_s and R_T equal to

zero, giving significant discrepancies between the equations. Therefore, Vaughan was able to find the work required in grounding by starting from the collision problem, whereas, Minorsky's work did not intend to capture this type of damage.

Vaughan (1980) followed up his preceding work by conducting experiments to investigate the effect of plate thickness in the absorption of energy due to the cutting by a sharp wedge. Drop hammer experiments involved four different plate thicknesses ($t=1.867, 1.181, 0.958, \text{ and } 0.752 \text{ mm}$), and three wedge semi-angles, θ (5, 15, and 30 degrees). Vaughan proposed that the energy can be decomposed into work in cutting and work in bending the plate, as in Equation 1.4. The unknown exponents and material coefficients were to be determined experimentally.

$$W = Sl \ t^{\alpha} + EA t^{\beta} = W_C + W_B \quad (1.4)$$

He argues that the work in cutting is dominant for small penetrations of the wedge into the plate, and the bending energy becomes significant as the cutting length increases. This is because $W_C \propto l$ and $W_B \propto l^2$. These wedges cut a short distance into the plate, therefore Vaughan investigated the work in cutting only. The results of nearly 70 drop hammer tests produce a series of graphs that allowed the investigator to determine the values for S and α . Vaughan uses the results of Minorsky's work to determine the bending energy term. Since the fully plastic bending moment is proportional to t^2 , Vaughan takes $\beta = 2$. Equation 1.4 takes the form

$$W = 5500l \ t^{1.5} + 4400 A t^2 = W_C + W_B \quad (1.5)$$

where t is measured in millimeters, l in meters, and A is the damaged area of the plate in square centimeters.

Several years later, Jones and Jouri (1987) conducted a new series of drop hammer experiments which investigated the energy required to cut plates that were thicker by as much as three times than those used by Vaughan. They also derive empirical expressions, much like those by Vaughan, for the total work in tearing a plate. Included are the work in cutting and distortion, as well as the work due to the friction between the wedge and the plate, given as

$$W = W_C + W_D + W_F \quad (1.6)$$

where W_D includes bending, membrane, and shear effects, and W_F the friction effect. The results of this study showed that for thin plates (on the order of 1.5 mm) the results correlated well to those of Vaughan. However, for the thicker plates, Vaughan's formula (Equation 1.5) overpredicted the absorbed energy for a given cut length for the thicker plates. This showed that geometric similitude is not observed when going from models to the prototype.

Lu and Calladine (1990) also conducted plate cutting experiments, but in their setup the wedge was driven into the plate in a quasi-static manner, using a universal testing machine rather than a drop hammer. They investigated the effects of varying the plate thicknesses (0.7 to 2 mm), wedge semi-angles, and plate angles of attack, ϕ . They derived an empirical relationship using dimensional analysis that showed the work required to cut the plate W was a function of the distance the wedge traveled, $u=l\cos(\phi)$, the plate thickness, t , and the yield stress, σ_y , of the material, where the plate angle of

attack to the wedge and the wedge semi-angle have been specified. The resulting equation is

$$W = C\sigma_y l^{1.3} t^{1.7} \quad (1.7)$$

valid for $5 < l/t < 150$, and where C is a dimensionless constant obtained from the experimental data. They found that C has strong dependence on the angle of attack of the plate to the wedge, but is insensitive to the wedge semi-angle. Lu and Calladine used their empirical formula and the results of Jones and Jouri's drop hammer experiments to compare the value of C for steel plates. They found that this value was 35% greater for the dynamic tests than for their quasi-static tests.

Up until this point, investigators had conducted plate cutting experiments and then, from the data, determined an empirical relationship for the work required. Wierzbicki noticed that there are two possible modes of failure in the plate separation problem. There is tearing of the plate in which the wedge does not contact the plate crack opening, and cutting in which the wedge does contact the plate crack opening. Wierzbicki and Thomas (1993) approached the problem by developing a kinematic model of the plate tearing initiation process by a wedge. By assuming kinematically admissible velocity and displacement fields that satisfied the boundary conditions, they were able to derive an upper bound closed form equation for the force required for a wedge to tear a plate. Equation 1.8 shows the force required to tear the plate, F_t , as a function of the plate thickness, t , length of cut, l , plate material flow stress, σ_o , wedge geometry function, $g(\theta)$, and the dimensionless crack opening displacement parameter, $\bar{\delta}_t = \frac{\delta_t}{t}$.

$$F_t = 1.67 \sigma_o (\bar{\delta}_t)^{0.2} l^{0.4} t^{1.6} g(\theta) \quad (1.8)$$

where

$$g(\theta) = (\cos \theta)^{-0.8} \left[(\tan \theta)^{0.4} + \mu (\tan \theta)^{-0.6} \right] \quad (1.9)$$

By plotting Equation 1.9, they were able to see that there is weak dependence on the wedge semi-angle, θ . The function $g(\theta)$ was minimized by solving for θ in $\frac{\partial g(\theta)}{\partial \theta} = 0$ resulting in the approximation for the tearing force as

$$F_t = 3.28 \sigma_o (\bar{\delta}_t)^{0.2} l^{0.4} t^{1.6} \mu^{0.4} \quad (1.10)$$

valid for $10^\circ < \theta < 30^\circ$, and where μ is the wedge-plate friction coefficient. Comparison of this result with the experimental work of Lu and Calladine showed very good agreement.

The solution for the plate cutting force was carried out in much the same way by Wierzbicki and Zheng (1993). The plate cutting force is given by

$$F_c = \frac{4}{3} \sigma_o l^{0.5} t^{1.5} g(\theta) \quad (1.11)$$

where

$$g(\theta) = (\sin \theta)^{0.5} (\cos \theta)^{-1} + \frac{1}{2} \mu (\sin \theta)^{-0.5} \quad (1.12)$$

The same minimization process as above yields the approximate result for plate cutting:

$$F_c = 1.92 \sigma_o l^{0.5} t^{1.5} \mu^{0.51} \quad (1.13)$$

Notice that the cutting force solution has eliminated the crack opening displacement parameter.

The closed form solutions by Wierzbicki, *et al.* are of the same functional form as the empirical relationships developed by Lu and Calladine. They are explicit in that the material parameters and geometry are entered directly into the formula, whereas in previous methods, the experimentally derived constants contained much of that information.

Zheng and Wierzbicki (1994) have recently formulated closed form solutions for the steady state plate cutting force. Their simplified model gives the following equation:

$$F_{ss} = M_o \left(2 \frac{B}{t} \sin \theta \tan \theta + 3\pi \right) (1 + \mu \cot \theta) \quad (1.14)$$

where M_o the fully plastic bending moment, and B is the wedge width.

1.4 Evolution of MIT Plate Cutting Experiments

There have been three generations of cutting experiments conducted at MIT. The first two were conducted by Thomas (1992) and Maxwell (1993), the details of which are contained in their respective theses. The third generation is described in this thesis.

The purpose of the first generation of tests was to determine the validity of the closed form solution in Equations 1.8 through 1.10. Thomas conducted eight experiments with two different wedge semi-angles and four plate thicknesses on both aluminum and cold rolled steel specimens. The specimen dimensions were 19 in. by 16.5 in. The plate

tilt angle of 20° was constant throughout all the tests. The theory correlated very well with the experimental results. One drawback to this set of tests was that the test machine was limited to a 100 mm stroke. This required that the tests be accomplished in three consecutive strokes.

The second generation of tests were designed to further explore the validity of Wierzbicki and Thomas' plate tearing solution, as well as the cutting solution of Wierzbicki and Zheng (Equations 1.11 through 1.12) by varying the plate thickness, angle of attack, and wedge geometry. To overcome the difficulty of the short cutting stroke of the previous experiments, Maxwell used a screw driven test machine that provided a continuous cutting stroke. There were nineteen tests conducted on three thicknesses of cold rolled steel. Three wedge semi-angles and a cylindrical wedge were used at four plate tilt angles. Maxwell designed and built a new test fixture to hold the 22 in. by 16.25 in. specimens. Maxwell investigated the central separation (i.e. central cutting and tearing) and the concertina tearing modes. The theory showed generally good correlation with the experimental results. All the existing tests and theoretical developments were concerned with unstiffened plates.

Paik (1994) recently conducted cutting experiments of longitudinally stiffened plates and used Wierzbicki and Thomas' plate cutting solution of Equation 1.8 by smearing the plate and stiffeners into an equivalent thickness plate. Paik compared two experiments to Equation 1.8 which underestimated the final work in cutting by 19.5% and 32.1%.

1.5 Research Objectives

This research expands the progression of experiments to include longitudinal structural members. The objectives of this research are:

(a) Design and perform cutting experiments of longitudinally stiffened single hull and double hull models. This will produce new experimental data in the area of ship grounding research.

(b) Develop new or modify existing kinematic models leading to closed form solutions of the force required to cut the *longitudinally stiffened structures* and compare to experimental results.

The geometry of the single and double hull models and wedges, and the experimental apparatus are discussed in Chapter 2. The experimental results are in Chapter 3. In Chapter 4, computational kinematic models are formulated producing upper bound force-displacement solutions which are compared to experiments. Chapter 5 concludes and makes recommendations for future work.

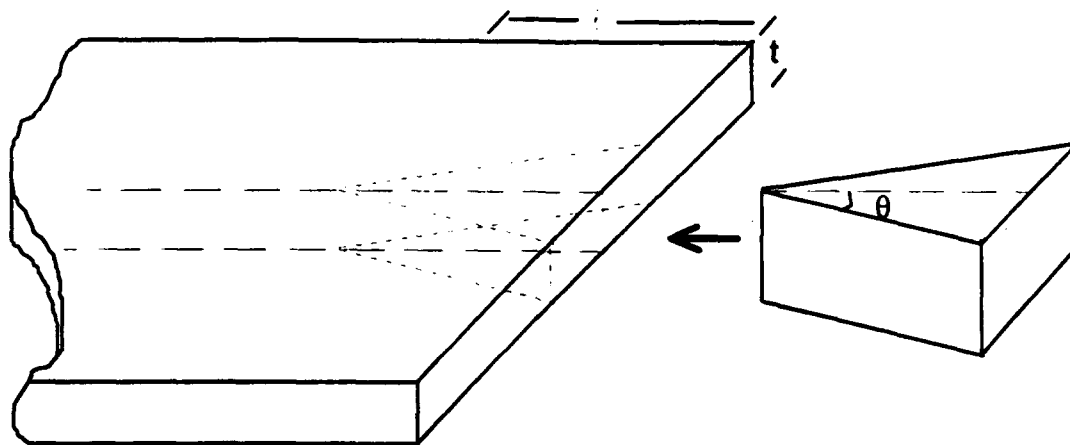


Figure 1.1 Plate Cutting by a Wedge.
(Vaughan (1978).)

Chapter 2

Experimental Models and Apparatus

The previous chapter discussed the state of the art in ship grounding research. This chapter describes the structural design considerations and geometry of longitudinally stiffened single hull VLCC and the Unidirectionally Stiffened Double Hull (USDH) design. From this, the geometry of the scale model specimens is determined. Also the design of the wedges that simulate various rock geometries is discussed, and the experimental apparatus is described.

2.1 Ship Structural Design Considerations

The structural design of a ship typically starts by determining the loading conditions that the ship will be experiencing during its service life. Normal operation includes loading conditions such as bending of the hull girder (hogging, sagging, and still water), cargo live loads, structural dead loads, liquid loads, cyclic fatigue, and exterior hydrostatic loads. The ship is also subjected to infrequent loads such as flooding and drydocking, and in the case of naval vessels, combat loads such as underwater explosions. The structure is designed, analyzed, and optimized to withstand the normal loads to some allowable stress level, and to remain intact under extreme loads. (The author was unable to find any ship design practices or references that consider grounding loads when designing ship structures.)

Mission characteristics such as payload capacity and endurance determine the size of the ship. This in turn, establishes the length, beam, and depth of the ship, and, hence, the structural dimensions. These dimensions are then analyzed under the loading

conditions. Ships that have similar size and function will have similar structural geometry.

The USDH design was first introduced by Okamoto, *et al* (1985) for use in bulk oil product carriers. The USDH employs longitudinal girders between the inner and outer hull plating. According to Okamoto, the primary advantages of the USDH design are:

- Reduced number of structural discontinuities which minimize stress concentrations,
- Improved structural integrity by increased torsional rigidity and more efficient load transmission,
- The structural simplicity allows for more complete analysis.
- Increased producibility and potential for automated welding due to the lack of closely spaced transverse members.
- Ease of inspection and maintenance between the hulls due to improved access in the cellular structure.

Beach (1991) expressed the interest of the U.S. Navy in the USDH design primarily for improved survivability of warships due to weapons effects, as well as the benefits listed above. The *Naval Surface Warfare Center* (NSWC) is conducting research in this design for use in naval ships.

Figure 2.1 shows the concept of the typical midship geometry of longitudinally stiffened single hull VLCC and the USDH design. The major disadvantages of the double hull compared to the single hull design are:

- Increased structural weight,
- Potential decrease in the ship's initial stability, and

- Increased inspection and maintenance requirements.

All of these lead to increased cost, but the cost may be recoverable by the significant advantage of the double hull in oil outflow protection (in the case of oil product carriers) and survivability (in the case of warships).

2.2 Determination of Scale Model Geometry

Ship structural designs vary depending on the function of the ship and design philosophy of the naval architect, thus making it difficult to pick the exact design geometry on which to base scale test models. Therefore, a representative design or design guidance was used to scale the USDH and longitudinally stiffened single hull models.

For the experiments, several constraints exist that had to be accounted for in scaling the models. The goal was to use as much as possible of the existing test fixtures, equipment, and steel sheet inventory on-hand in the lab in order to save time and expense.

2.2.1 Double Hull Model

The geometry for the USDH model was determined with the cooperation of NSWC. For simplicity, square cells were selected. To find the geometry of the model, three major constraints were considered:

1. The selected welding technique¹ required a minimum plate thickness of approximately 0.5 mm (0.02 in.).

¹ The technique used was electron beam welding. This is discussed further in Section 2.3.1.

2. The fixture that holds the model was designed for a maximum plate thickness of 2 mm (0.08 in.).
3. NSWCC recommended a cell width to plate thickness ratio, b/t , of 62.

Plate thicknesses of 0.406, 0.749, 1.130, and 1.829 mm were evaluated. The 0.406 mm plate failed to meet the minimum thickness for welding criteria. The 1.130 and 1.829 mm plates were not used since the combined thickness of two plates in the double hull design exceeded the 2 mm constraint. The 0.749 mm plate met the minimum thickness for welding and the 2 mm constraint, and therefore was selected for dimensioning of the USDH model.

The next task was to determine the number of cells in the model. It was desired that the center cell be symmetric about the plate longitudinal axis so that the wedge would begin to cut between two longitudinal stiffeners. This required an odd number of cells. Several other factors drove the dimensioning of the cells:

- The wedge shoulder width was to be approximately $2b$. This would ensure that the longitudinals would interact with the wedge.
- The test fixture designed by Maxwell only accommodates a single plate. The addition of the second plate in the double hull model would require that spacers be added to the fixture to ensure the model was fully clamped at the edges.
- The effective width of the model, w , when installed in the test fixture is bounded at 11.5 in. (292.1 mm).

A discrete number of cells can be fitted into the 11.5 in. width. A reasonable number of cells would be 3, 5, 7, or 9. Table 2.1 shows that the number of cells drives cell

dimensions, spacer size, and the wedge shoulder width, which in turn determines the size of the wedge. Since the wedges and spacers are fabricated out of solid blocks of steel, it was desired to keep the weight and machining cost down. However, it was desired to have the model dimensions large enough so that interaction of the longitudinals with the plating can be studied. Therefore, seven cells were selected, which gave the cell dimensions of $h=b=1.64$ in. (note that there are 5 actual cells in the model plus two cells when the frame spacers are added). This selected cell spacing gives $b/t=55.7$, which is considered satisfactory. Figure 2.2 shows the final USDH model geometry.

Table 2.1 USDH Model Cell Size Options.

N (number of cells)	$w/N = b$ (cell spacing)	Wedge Shoulder Width ($\approx 2b$)
3	3.83 in. (97.3 mm)	7.66 in. (194.6 mm)
5	2.30 in. (58.4 mm)	4.6 in. (116.8 mm)
7	1.64 in. (41.7 mm)	3.28 in. (83.4 mm)
9	1.28 in. (32.5 mm)	2.56 in. (65.0 mm)

2.2.2 Single Hull Model

The geometry of the single hull model was based on the midship section taken from a 140,000 dwt VLCC², provided by Fernandez (1993), who considered this ship of typical modern VLCC design. The VLCC prototype has a length between perpendiculars (LBP) of 269.0 m and a beam of 43.2 m.

² Plan No. 71147-10-1001-MOD1, Astilleros Espanoles, S. A., Factoria de Puerto Real, Hull C. 56, 15 March 1988.

For the plate cutting experiments, a representative uniform section from the VLCC prototype was selected to be modeled. This section has only longitudinally stiffeners attached to the plating. No transverse members or major longitudinal girders were included. The clamped boundary condition at the bottom of the test fixture acts as a transverse member. The task was to determine the proper parameters to scale the model from the prototype VLCC section. The geometry of a single stiffener/plate combination is shown in Figure 2.3. For the VLCC prototype, the dimensions of the stiffener and plate are given in Table 2.2.

Table 2.2 VLCC Prototype Stiffener and Plate Dimensions.

plate:	$t_p = 18 \text{ mm (0.71 in.)}$
	$b = 850 \text{ mm (33.46 in.)}$
web:	$t_w = 11 \text{ mm (0.43 in.)}$
	$b_w = 525 \text{ mm (20.67 in.)}$
flange:	$t_f = 30 \text{ mm (1.18 in.)}$
	$b_f = 180 \text{ mm (7.09 in.)}$

The initial parameters for scaling from the prototype to the model were based on the section moment of inertia. Since the longitudinal section design is based largely on primary bending stresses due to hogging and sagging of the ship hull girder, it was thought that this was the proper scaling method. It turned out that this was probably not the best method since many different model stiffener/plate dimension combinations could give the same section moment of inertia as the prototype. This was unsatisfactory since it was desired that the model have similar stiffener/plate interaction when cut by a wedge as

the prototype would upon grounding. It is expected that the stiffeners will inhibit plate bending and, in turn, the bending of the plate will cause tripping of the stiffeners. So, the thickness ratios of the web, flange, and hull plate of the VLCC prototype were used as scaling parameters.

As mentioned above, there was an inventory of steel sheets on-hand in the lab, with thicknesses $t_1 = 0.749$ mm (0.030 in.), $t_2 = 1.130$ mm (0.044 in.), and $t_3 = 1.829$ mm (0.072 in.). These three thicknesses were used in some combination so that the model would scale with the prototype geometry. Using t_1 for the web, t_2 for the plating, and t_3 for the flange gives the thickness ratios shown in Table 2.3.

Table 2.3 Stiffener/Plate Thickness Ratios for VLCC Prototype and Model.

VLCC Prototype	Scale Model	Relative Error
$t_f / t_w = 2.73$	$t_3 / t_1 = 2.44$	-10.6 %
$t_p / t_w = 1.64$	$t_2 / t_1 = 1.51$	-7.9 %
$t_p / t_f = 0.60$	$t_2 / t_3 = 0.62$	+3.3 %

Scaling by these thickness ratios gives a reasonable model of the prototype based on the relatively small errors. A further check was conducted by calculating the ratio of moments of inertia of the plate/stiffener combination to hull plating for both the model and the prototype as shown in Equation 2.1.

$$\frac{I_M}{I_{pM}} = 4.006 \times 10^3 \quad \frac{I_{VLCC}}{I_{pVLCC}} = 3.452 \times 10^3 \quad (2.1)$$

The relative error between the ratios is 16%. The selected steel sheet thicknesses for the model and the associated prototype b/t ratios from Table 2.2 give the model geometry shown in Table 2.4.

Table 2.4 Single Hull Model Stiffener and Plate Dimensions.

plate:	$t_p = 1.130 \text{ mm (0.044 in.)}$
	$b = 53.36 \text{ mm (2.1 in.)}$
web:	$t_w = 0.749 \text{ mm (0.030 in.)}$
	$b_w = 35.75 \text{ mm (1.41 in.)}$
flange:	$t_f = 1.829 \text{ mm (0.072 in.)}$
	$b_f = 10.97 \text{ mm (0.442 in.)}$

With $b = 2.1$ in. from Table 2.4, six longitudinals could be fitted onto each plate. Since the wedge shoulder width is approximately 3 in. (as determined by sizing the USDH model), it was surmised that the outermost longitudinals would not be affected during cutting. Furthermore, if the longitudinals were affected, they probably would interfere with the sides of the test fixture. Therefore, four longitudinals spaced symmetrically about the longitudinal center line of the plate were selected for the single hull model as shown in Figure 2.4.

2.3 Fabrication of the Hull Models

Determining the joining technique to be used for the double hull model proved to be the most difficult task. Unlike full scale ships, where access to the joint is possible, the

models were so small that access to all the joints was nearly impossible. Three possible welding schemes were evaluated. The first method consisted of fillet welding one of the outermost longitudinals to both plates. Subsequent longitudinals would have been inserted in between the plates, but only one side would have been welded as shown in Figure 2.5. The second method consisted of welding I-beam sections together to achieve the desired double hull geometry. The final method was to join the longitudinals to the plates from the plate side opposite of the joint (i.e. the blind side). Two such joining methods were investigated: electron beam welding (EBW) and brazing.

2.3.1 Welding Technique Selection

Several machine shops at MIT were consulted to determine the feasibility of these joining methods. The machine shops were deemed to have inadequate equipment to perform what they characterized as a difficult task. The Ocean Engineering (OE) and the Nuclear Engineering (NE) Welding Laboratories, two specialized laboratories at MIT, were consulted for further assistance.

Both labs rejected the option of the I-beam method primarily because of the unavailability of the desired dimensioned I-beam. Manufacture of custom I-beams would have been expensive and difficult. Even if such I-beams were available, residual stresses due to welding would have been introduced which might have caused considerable distortion of the double hull model.

The welding labs were unable to apply conventional welding techniques to the model due to the joint access restrictions. The OE lab suggested the use of electron beam or brazing. The electron beam technique is a fusion joining process in which the workpiece is bombarded with a dense stream of high velocity electrons in an evacuated

chamber. A major advantage of EBW is the very deep penetration that is achieved. Brazing coalescence is produced by using a nonferrous filler metal having a melting point below that of the base metal. The filler metal is distributed between the closely fitted joint surfaces by capillary action.

Two outside specialists were consulted for assistance in the joining problem. *Hooven Metal Treating Incorporated* recommended use of nickel braze to allow relaxation of the tight joint tolerances. However, *Hooven* still had reservations about the success of the process. Joint fitup tolerances in brazing must be very tight, otherwise the filler metal will not flow and gaps will ensue. This will result in a weakened bond. The MIT machine shops determined that even the relaxed tolerances were tighter than their capability to machine. The *Applied Energy Company* was asked to assess the feasibility of manufacturing the double hull models using the electron beam welding (EBW) technique. A "T" specimen was successfully welded from the flange side of the specimen. However, due to the very narrow electron beam, weak points at the "T" joint between the longitudinal and the plate could be introduced as shown in Figure 2.6. There was concern in maintaining as much welding similitude of the model to the full scale prototype, so, the electron beam was oscillated at 60 Hz laterally as the beam traveled longitudinally. This simulated a fillet weld (as well as possible for this technique) in the specimen and served to minimize the weak points in the weld. The EBW method produced very little distortion of the specimens. This method proved to be the best for welding of the double hull models, and was also used for joining the single hull models. For the interested reader, Becket (1991) gives a good overview of the EBW process.

2.4 Wedge Geometry and Fabrication

Rocks in the ocean are as varied as what is seen on land. They could be characterized by the basic shapes of cones, spheres, or ledges. A study of rock geometries for use in modeling of wedge geometry has not been done. The dilemma was to select a wedge geometry that makes analysis of the experiments easier, while trying to capture what happens in a real ship grounding. Previous plate cutting experiments by Thomas and Maxwell focused mainly on the use of sharp wedges. Both investigated the use of wedges with semi-angles of 20° and 30° . Maxwell also used a cylindrical wedge.

It was decided early on, that for this research, the narrow 20° wedge was not thought to represent any nominal rock geometry, so, much broader semi-angles of 30° and 45° were selected. A radius was applied to some of the wedge tips to model a more blunt rock. A cylindrical wedge was also fabricated to ensure a completely blunt surface where no machining-type cutting could be applied to the plate by the wedge. A narrow wedge (i.e. shoulder width less than the longitudinal spacing) was fabricated to be used to determine the force in cutting the plate between longitudinals (as explained in Chapter 3.). Table 2.5 and Figure 2.7 summarize the six wedges used in the experiments.

The wedges were machined from solid blocks of cold rolled mild steel. Subsequent use of two of the wedges showed that the wedge surfaces scarred quite easily at the point of contact between the wedge and plate. It was feared that continued use would machine a groove into each wedge, thus causing the plate to preferentially stay in the groove during cutting. To avoid this, each wedge was surface hardened to a depth of 0.030". The hardening was done by the *BoMak Corporation*, of Woburn, Massachusetts. *BoMak* treated each wedge in a cyanide solution at 1650°F for three hours.

Table 2.5 Geometry of Wedges.

Wedge No.	Wedge Semi-angle (θ)	Tip Shape	Shoulder Width
1	45°	sharp	3 in.
2	45°	3/8 in. radius	3 in.
3	30°	sharp	3 in.
4	30°	3/8 in. radius	3 in.
5	cylinder	1.5 in. radius	3 in.
6	45°	3/32 in. radius	3/4 in.

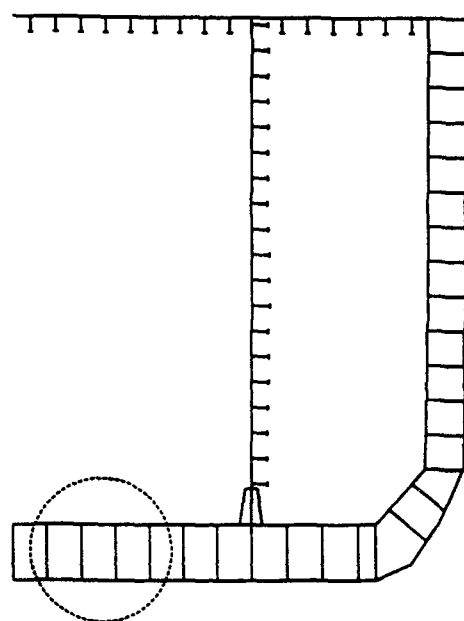
2.5 Experimental Apparatus

The experiments were conducted on the same equipment as that used by Maxwell. It was desired to use as much of the existing equipment and steel stock as possible to minimize the costs of the experiments. Modifications to the fixtures were made as required to support the current series of tests. The test apparatus consists of the following equipment shown in Figure 2.8:

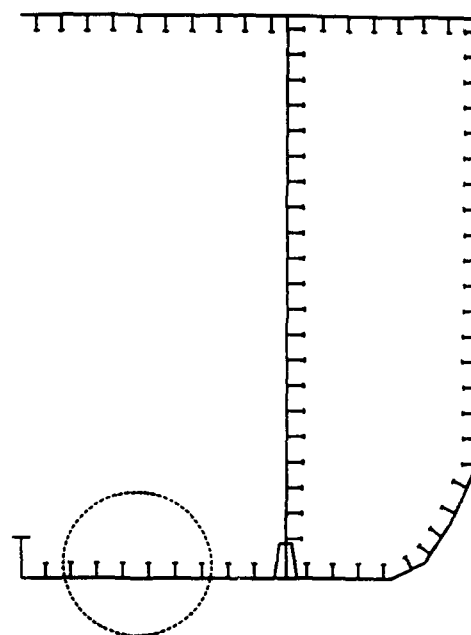
- Instron (Model TTDL) Universal Test Machine (screw driven, 20 kip capacity)
- Zenith 386-SX Personal Computer (IBM compatible)
- National Instruments Data Acquisition Software Program (NI-DAQ version 4.2)
- Specimen Test Fixture
- Various Wedges
- Wedge-to-Load Cell Adapter

The specimen test fixture is shown in Figure 2.9. The 16.5 in. width of the fixture was limited by the crosshead width. Spacers were fabricated to hold the double hull specimens in a clamped boundary condition on both plates. The long rods in the fixture act as drawing beads to give a uniform zero displacement boundary condition. The bolts provide the clamping force. The wedge adapter is shown in Figure 2.10. The adapter is attached directly to the load cell located at the top of the machine. The wedge is attached to the bottom of the adapter. The fixture and adapter provide an effective cutting stroke of approximately 13.5 in.

Appendix A explains the procedure for the operation of the Instron test machine, data acquisition program, and the subsequent data reduction.



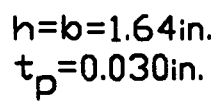
USDH



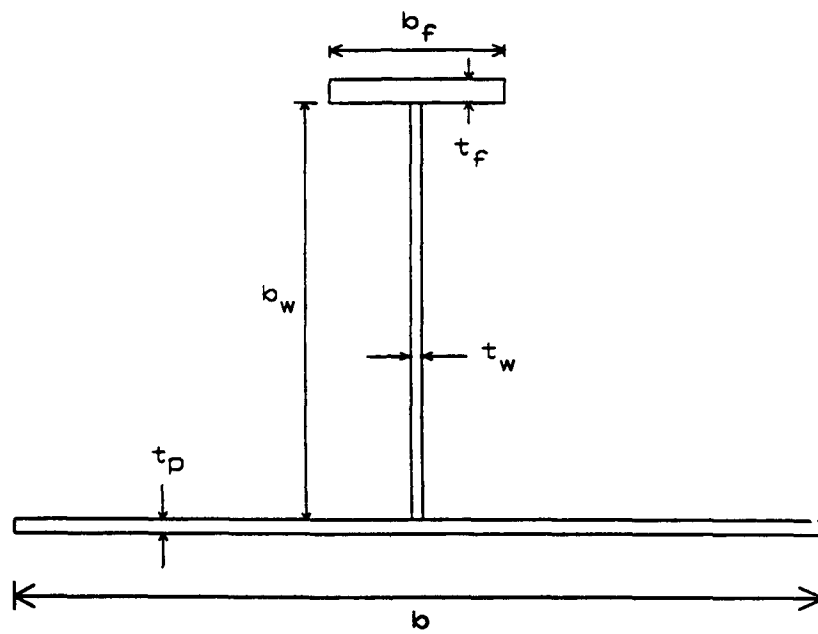
Single Hull

(Circled sections represent the structural members for the experimental models.)

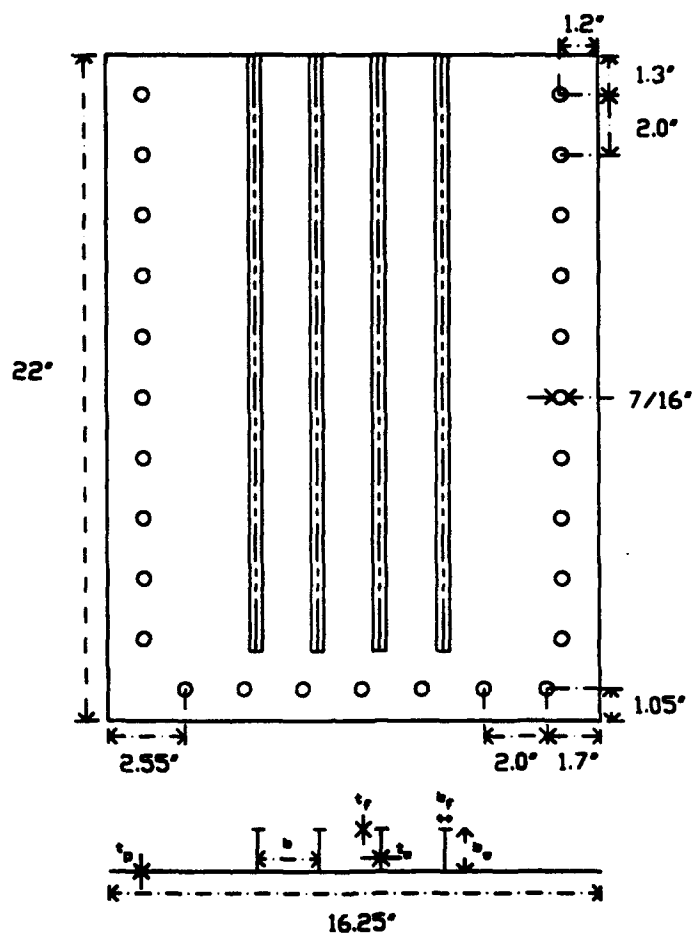
Figure 2.1 Concept of Unidirectionally Stiffened Double Hull (USDH) and Single Hull (SH) VLCC Midship Sections.



45



2.3 T-Stiffener/Plate Combination.



$$t_p = 0.044 \text{ in.} \quad t_w = 0.030 \text{ in.} \quad t_f = 0.072 \text{ in.}$$

$$b = 2.1 \text{ in.} \quad b_w = 1.41 \text{ in.} \quad b_f = 0.442 \text{ in.}$$

2.4 Longitudinally Stiffened Single Hull Model.

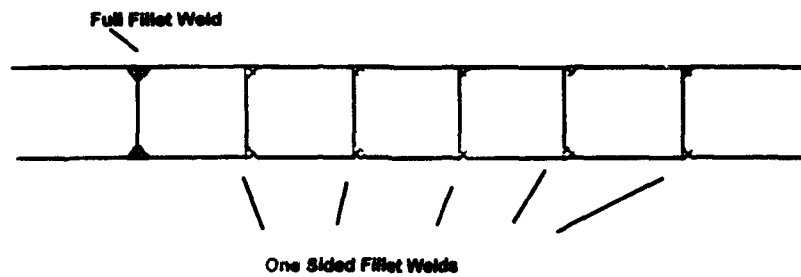


Figure 2.5 Fillet Method of Welding the USDH Model.
(Concept by M. Yahiaoui.)

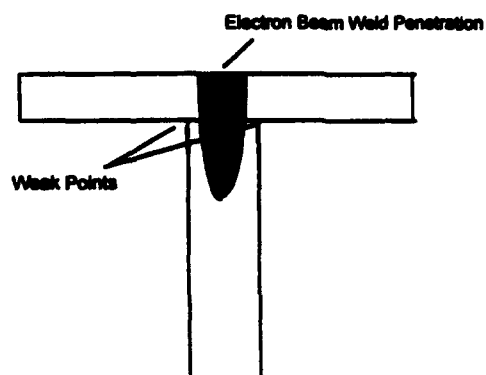
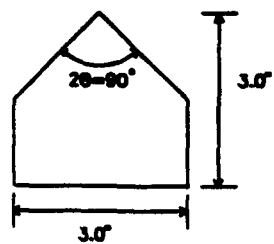
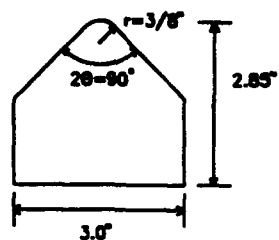


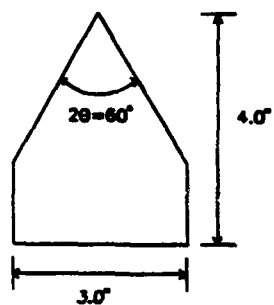
Figure 2.6 Possible Defect of Electron Beam Welding of T-stiffener.
(Concept by M. Yahiaoui.)



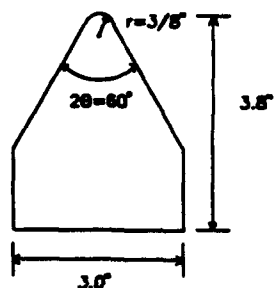
Wedge 1



Wedge 2



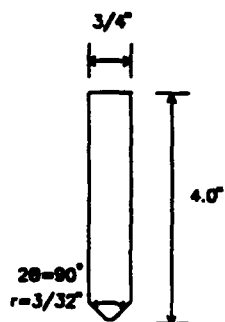
Wedge 3



Wedge 4

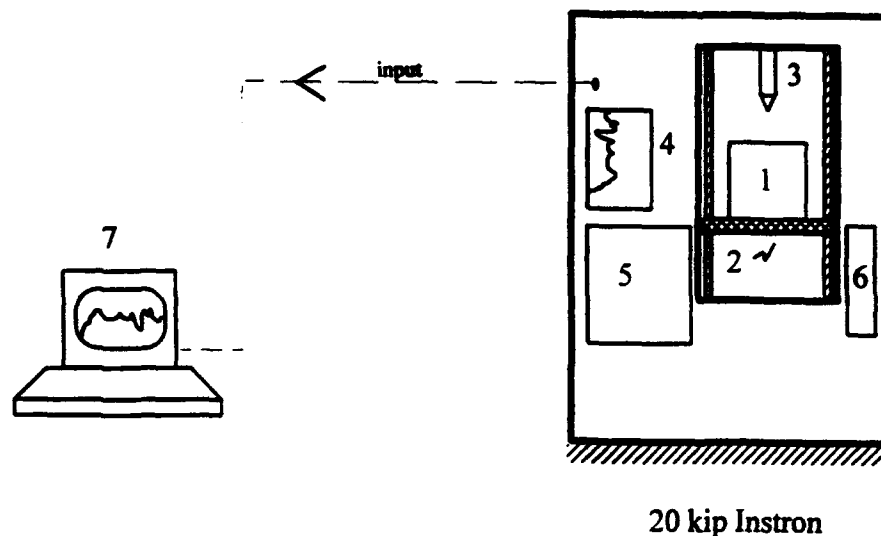


Wedge 5



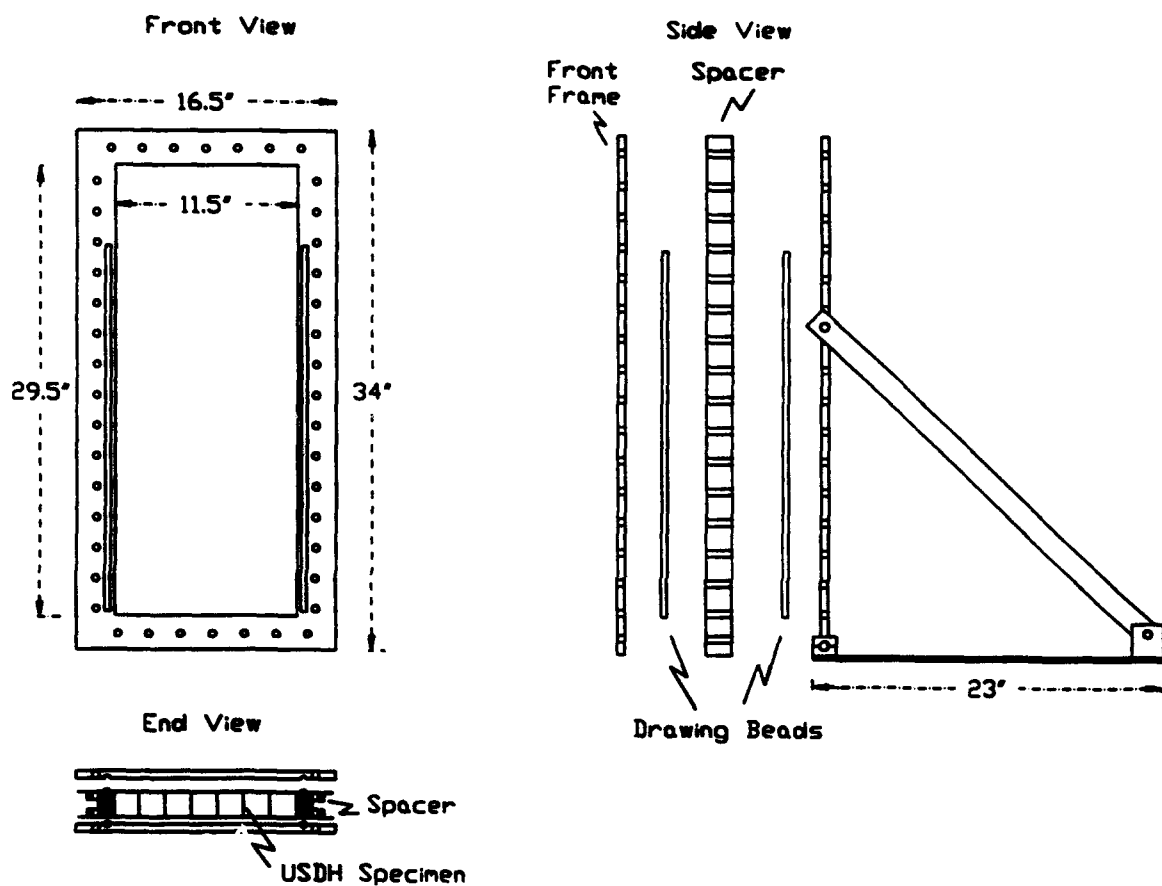
Wedge 6

2.7 Geometry of Wedges (section view).

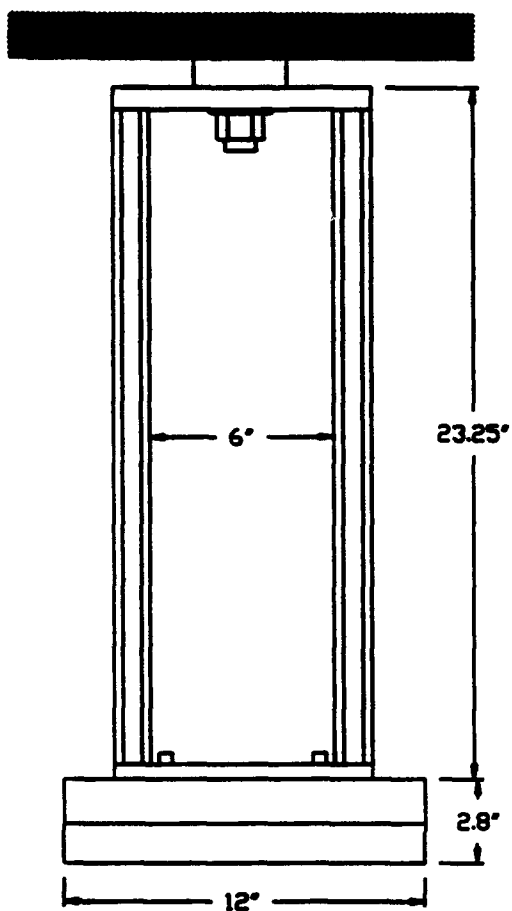


- Legend:**
- 1. Specimen
 - 2. Crosshead
 - 3. Wedge and Adapter
 - 4. Built-in Chart Recorder
 - 5. Machine and Chart Recorder Control Panel
 - 6. Crosshead Control Panel
 - 7. Data Acquisition Computer

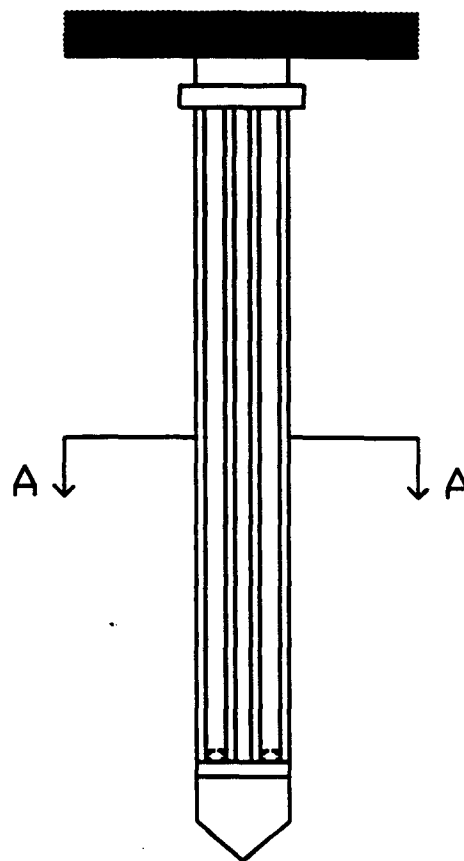
Figure 2.8 Schematic of 20kip Instron Universal Test Machine and Data Acquisition System.



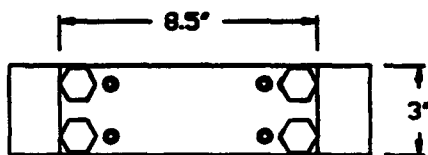
2.9 Specimen Test Fixture.



Side View



Front View



Section A-A

2.10 Wedge-to-Load Cell Adapter.
(Drawn by P. Little.)

Chapter 3

Experimental Results and Observations

3.1 Preparation of the Instron Universal Test Machine

The experiments were carried out on the Instron 20 kip screw driven universal testing machine as discussed in Chapter 2. A 386 personal computer with a National Data Acquisition software package was used to process the output from the test machine. There had been concern that the data acquisition program may not be set up properly or that there may be some problem with the test machine since some of the force-displacement graphs from previous experimental work were showing cut off of the data. Nurick (1993) recommended that a verification of the machine output be conducted.

The approach to verification was to conduct tensile tests on a 1 kip Instron machine (that was known to give good results) and the 20 kip Instron machine, and then compare the results.

To prepare the 20 kip Instron machine, the connections between the data acquisition computer and the Instron were rewired. The rewiring was required since some of the connections were frayed. This cleared up the data cut off problem. The built-in strip chart recorder was returned to working order. The strip chart recorder was to be used as a backup to the data acquisition program, and would serve to verify the results of the computer program.

The tensile specimens used were in accordance with ASTM section A370 specifications. Two tests were conducted on each Instron machine. There was little variation of the force-displacement graphs between the 1 kip Instron machine, the chart

recorder output and data acquisition program output of the 20 kip Instron machine. The conclusion was that the setup and output of the 20 kip Instron machine was satisfactory and ready for use in the cutting experiments.

3.2 Summary of Experimental Results

The results, observations, problems, and resolutions during the wedge cutting of the longitudinally stiffened double and single hull models are presented. A total of twelve experiments were conducted on the single and double hull models as summarized in Table 3.1. The force-displacement curves and accompanying photographs are referenced by the figure numbers in the table. The primary failure modes listed in the table are explained as follows and can be observed in the photographs:

- "Cutting" - the plate curls and flaps are formed as it is cut by the wedge.
- "Concertina" - the plate tears and folds in the concertina mode.
- "Shear" - the longitudinals and the attached plating deform in shear buckling as the wedge progresses.

The results are not presented in the actual order that the tests were conducted, rather they are presented in a manner that makes it easier for the reader to assimilate the information.

The Instron machine was setup and operated according to the procedure shown in Appendix A. The equipment parameters were the same for each experiment. All of the experiments were conducted with the models at a zero degree angle of attack from the vertical, and the crosshead traveled at a displacement rate of 1 inch/minute.

Table 3.1 Summary of Cutting Experiments Results.

Test No.	Test Date	Model	Wedge No.	Primary Failure Modes	Force Curve and Photo
1	1/27/94	USDH	#1 : $\theta = 45^\circ$, sharp tip	Cutting, Shear	Fig 3.1
2	10/5/93	USDH	#2 : $\theta = 45^\circ$, $r=3/8$ in.	Concertina, Shear	Fig 3.2
3	9/30/93	USDH	#3 : $\theta = 30^\circ$, sharp tip	Cutting, Concertina, Shear	Fig 3.3
4	1/31/94	USDH	#4 : $\theta = 30^\circ$, $r=3/8$ in.	Concertina, Shear	Fig 3.4
5	2/8/94	USDH	#5 : cylindrical	Cutting, Concertina, Shear	Fig 3.5
6	2/2/94	USDH	#6 : $3/4$ in., $r=3/32$ in.	Concertina Only	Fig 3.6
7	1/5/94	SH	#1 : $\theta = 45^\circ$, sharp tip	Cutting	Fig 3.7
8	2/4/94	SH	#2 : $\theta = 45^\circ$, $r=3/8$ in.	Cutting	Fig 3.8
9	1/3/94	SH	#3 : $\theta = 30^\circ$, sharp tip	Cutting	Fig 3.9 (a), (b)
10	2/8/94	SH	#5 : cylindrical	Cutting, Concertina	Fig 3.10
11	12/10/93	SH	#6 : $3/4$ in., $r=3/32$ in.	Concertina Only	Fig 3.11

3.3 Discussion of Experimental Results

3.3.1 Double Hull Tests

All of the double hull model tests were accomplished with the wedges cutting through both plates. In every test, a characteristic shear wave pattern was observed as shown in the photographs of Figures 3.1 through 3.5. As the wedge cut into the plate the longitudinal and attached plating buckled and folded out of plane. In all tests, the electron

beam welds did not fail. In the concertina tearing mode, the plates tore in what appears to be the HAZ due to the EBW process. There was no tearing of the longitudinals; rather they buckled and folded due to the shear forces of the wedge-plate interaction. Some shear buckling can be seen on the specimens at a distance of 1 to 1.5 cells away from the center cell, but the bulk of the damage is localized to the vicinity of the wedge width.

Test 1 - (Wedge #1, $\theta=45^\circ$, sharp tip) The primary failure modes were cutting of the both plates at the wedge tip, and the characteristic shear buckling of the plating and longitudinals. The force level climbed rapidly as the wedge shoulders made contact with the inner longitudinals. Once this contact was made, then the average force level increased at a constant rate. The final average force was approximately 23 kN at 0.31 m cut length. Figure 3.1 shows the photograph and force-displacement curve.

Test 2 - (Wedge #2, $\theta=45^\circ$, $r=3/8$ in.) The model failed in concertina tearing of both plates due to the blunt tip of wedge #2. The force-displacement curve of Figure 3.2 showed periodic oscillations in the force level. This was due to the local effects of concertina tearing. The final average force level was approximately 26 kN at 0.31 m of cut length.

Test 3 - (Wedge #3, $\theta=30^\circ$, sharp tip) In this first test on the double hull models, it was noticed that as the cutting of the specimen progressed to about two inches in depth, a significant out-of-plane bending moment was placed on the adapter connecting the wedge to the load cell. The adapter was cylindrical and approximately two feet in length. The cause was that the frame holding the specimens had to be offset so that it could pass next to the adapter during the cutting stroke. The offset was on the order of three inches

from the center of loading. A bending moment ensued due to the large force encountered in cutting both plates of the double hull specimen and the offset. The test was stopped for fear of damaging the load cell. To correct this condition, a new adapter was designed consisting of four rods bolted to a plate. This plate was then connected to the load cell. This configuration allowed the double hull specimen to be aligned directly under the center of loading and thus the rods would straddle the plate as the wedge progressed deep into the plate. The double hull test was resumed and this configuration proved successful with no applied moments on the adapter. Figure 3.12 shows the adapter configurations.

The force-displacement curve in Figure 3.3 showed that the force reaches a high level at a short cut distance into the specimen. This force was close to the mean force throughout the entire cutting process. This explains the bending of the adapter shortly after starting the first test. The specimen exhibited two distinct failure modes: cutting of one plate, and concertina tearing of the other. The cutting mechanism showed the curled flaps as in the single infinite plate cutting experiments except that, when the flap reached the longitudinal, it folded over. This continued throughout the cutting length. On the other side the concertina mode progressed throughout with the longitudinals as the boundary. The force level reached approximately 20 kN near the end of the test.

Test 4 - (Wedge #4, $\theta=30^\circ$, $r=3/8$ in.) The primary failure modes were concertina tearing of both plates and shear buckling. Figure 3.4 shows the periodic oscillations due to the concertina tearing. The final average force level was approximately 20 kN at 0.34 m of cut length. Thirty-five concertina folds were observed.

Test 5 - (Wedge #5, cylindrical, 3" diameter) This test represents the more realistic failure modes that would be expected in an actual ship grounding. Concertina

tearing of one plate and cutting of the other plate along with shear buckling was observed. There was fracture of the plate being cut running ahead of the wedge face. There was off-center travel of the wedge as it progressed down the specimen because there was no sharp wedge angle to keep it centered. The off-center travel tore both plates away from one of the longitudinals (the second longitudinal from centerline). This tearing near the longitudinal was again in the HAZ of the weld. Figure 3.5 shows the photograph of the specimen and the force curve. The large drop-offs of the force level are due to the plate fracture. Once the wedge face caught up with the crack tip, the force level began to increase. This rise and fall of force due to cracking continued throughout the test. The smaller periodic oscillations are due to the concertina tearing of one plate. The final force level reached approximately 30 kN, and was the largest force level of the double hull tests.

Test 6 - (Wedge #6, 3/4" width, $\theta=45^\circ$, $r=3/32$ in.) The purpose of this test was to determine the force level in the concertina tearing mode. The wedge width being less than the longitudinal spacing, and the round tip ensured that the concertina tearing mode was observed with no interaction between the wedge and longitudinals. Figure 3.6 shows the photograph of the concertina folds and the force curve shows the periodic oscillations. The thirty-five peaks on the force curve correlate to the number of folds observed in the specimen. The average force level is constant at approximately 8 kN (note that this is the force level for the concertina tearing of both plates).

3.3.2 Single Hull Tests

In general, the single hull cutting experiments exhibited complex failure mechanisms. Various modes of bending and membrane stretching are observed in the plate and the web and flange of the longitudinal members. In all tests, no failure of the EB welds was observed. The rolling of the plate flaps is evident as would be expected from the numerous unstiffened plate cutting experiments conducted by other investigators (see Chapter 1). Significant friction between the wedge and the rolled plate flaps was observed as shown by scoring and rubbing marks on the test specimens. The stiffener flanges are thought to have significant elastic energy stored as evidenced by little to no folding of the flanges into small radii of curvature.

Test 7 - (Wedge #1, $\theta=45^\circ$, sharp tip) The primary failure mode was central cutting with rolling of the plate flaps and longitudinals. Figure 3.7 shows the test results. As the test began, the characteristic flaps curled inward towards the longitudinals. The sharp rise in the force level occurring at approximately 0.025 m was due to the wedge shoulders making contact with the flanges. At a force level of about 17 kN, oscillations occur due to cracks periodically running laterally across the plate as the wedge progressed. The plate tore and the crack would run towards the longitudinals. Once the crack tip neared the welded joint, it stopped and the wedge would catch up and begin cutting the plate. During this time, the longitudinals were rolling up with the plate. At a cut length of about 0.1 m, the inner two longitudinals, made contact with the outer two longitudinals. This accounted for the rise in force to a level to about 23 kN. The cutting continued until fracture again occurred at 0.2 m. The force level to climbed to about 25 kN before the test was stopped.

Test 8 - (Wedge #2, $\theta=45^\circ$, $r=3/8$ in.) The primary failure mode was central cutting. Figure 3.8 shows the force-displacement curve and specimen photograph. At the start of the test, a tear of the plate near one of the outer longitudinals occurred in the HAZ. This tear was approximately two inches. This caused the wedge to cut off-center, which in turn caused the plate flap to fold in a sheared concertina mode. The drop in force at approximately 0.1 m of cut length was due to plate tearing in the weld HAZ near one of the outer longitudinals. The drop in force at 0.15 m was due to plate cracking ahead of the wedge. The subsequent rise in force level is due to the buckling of one of the inner longitudinals. Cracking of the plate ahead of the wedge tip again occurred at approximately 0.22 m.

Test 9 - (Wedge #3, $\theta=30^\circ$, sharp tip). This was the first single hull experiment and, as in the first double hull test, a bending moment on the load cell occurred. This happened because the wedge began to drift off center as the cutting started, causing the wedge to make contact with only one of the longitudinals. The stiffness of the longitudinal pushed the wedge off center even more. As the wedge traveled, the plate began to fracture, rather than being cut by the wedge. A lateral bending moment developed on the wedge adapter, and the test was stopped for fear of damaging the load cell. Figure 3.9(a) shows the partial results of this test. From the figure, it can be seen that up to approximately 0.025 m, the force was increasing as the plate flaps developed. After that, the force drops off dramatically to near zero as the plate began to crack. Around 0.05 m of cutting distance, the wedge made contact with the longitudinal and the force increased.

Rather than discard the single hull model, the damaged portion of the model was cut off, leaving a shorter specimen for testing. To prevent a bending moment on the

wedge adapter from developing, a precut notch of 0.5" was made to this modified specimen. The test was continued with the same wedge. The precut was successful in that the wedge stayed in the center of the plate and both shoulders of the wedge contacted the longitudinals at nearly the same instant. The force-displacement curve shown in Figure 3.9 (b) shows that the force increases up to a cut length of approximately 0.125 m with some drop-offs at approximately 0.05 and 0.1 m. The webs of the longitudinals were being rolled up with the plate flaps. From about 0.125 m to 0.15 m the force appears to level off as if it were to begin steady state cutting, however, the force drops off rapidly as the plate flaps begin to roll in the opposite direction. The plate begins to be pushed out away from the longitudinals, and since the longitudinals were no longer being rolled up, the force level dropped. At 0.2 m cut length, the force began to increase as the longitudinals started to buckle and try to trip in towards the wedge. As can be seen from the graph, the force level climbs to its previous level of about 15 kN (before the flap direction change) just prior to completing the test.

Test 10 - (Wedge #5, cylindrical, 3" diameter). The primary failure mode was concertina tearing and rolling of the plate flaps and longitudinals. Figure 3.10 shows the test results. Concertina tearing began immediately after starting the test. At approximately 0.08 m of cut length, the force jumps because one of the inner longitudinals had completely tripped and was now being pushed into its neighboring outer longitudinal. As the test continued, the wedge began to drift off centerline, and the peak force of approximately 26 kN at 0.15 m is due to the wedge riding nearly directly over a longitudinal. Due to this off-center travel, the mass of concertina folds slipped from under the wedge. The blunt cylindrical wedge now caused the plate to fracture ahead of

the wedge face. This accounts for the dip in force level to below 10 kN. The wedge then caught up to the crack tip and folding of the plate began causing the force to increase.

Test 11 - (Wedge #6, 3/4 in. width, $\theta=45^\circ$, round tip). This test was conducted to determine the force required in concertina tearing of the plate between the longitudinals. Figure 3.11 shows the force displacement curve. It was thought that the concertina tearing mode would be observed in the other single hull tests, but this turned out not to be the case (except for some partial concertina tearing in Test 10).

The last single hull experiment was to use wedge #4 ($2\theta=60^\circ$, $r=3/8$ in.). This experiment was not accomplished since the results of the previous single hull tests showed similar failure modes. It was determined that no new information would be gained from conducting this last experiment.

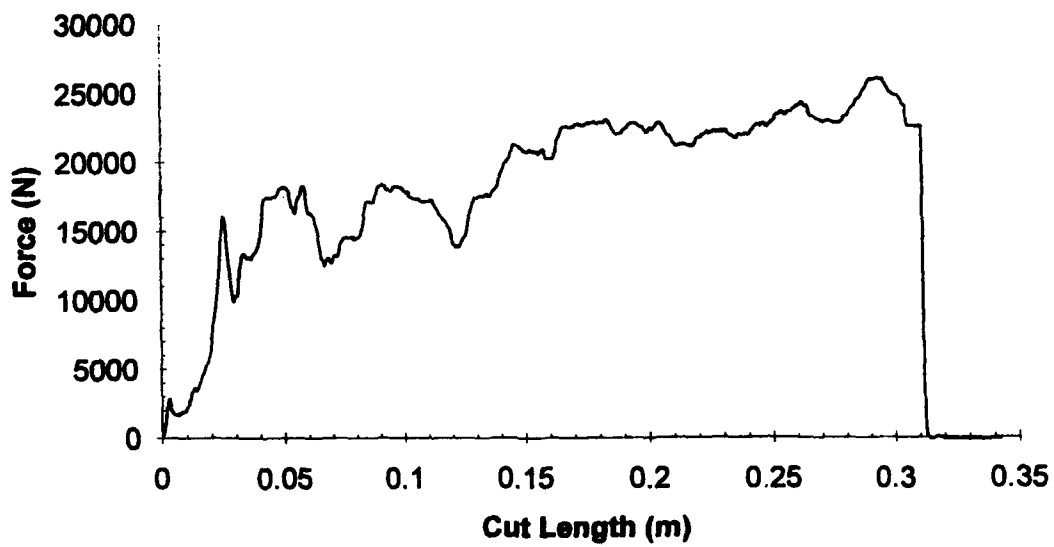
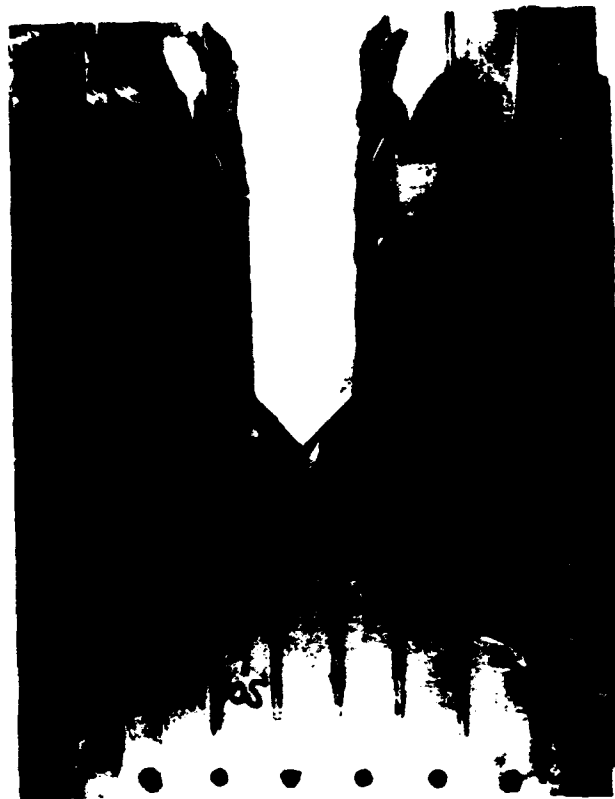


Figure 3.1 Test No. 1 (USDH, Wedge #1, $\theta=45^\circ$, Sharp Tip) - Photograph and Force-Displacement Graph.

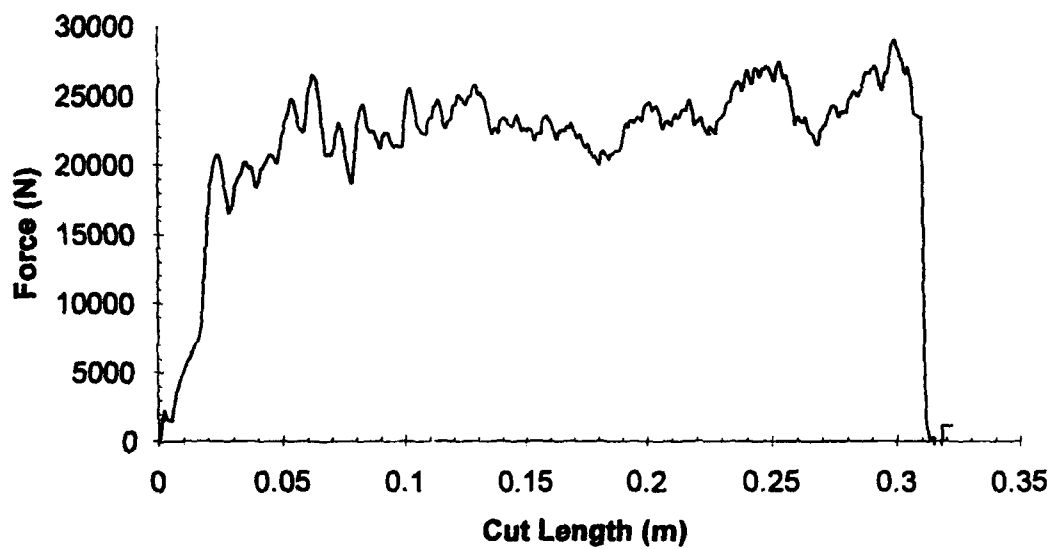


Figure 3.2 Test No. 2 (USDH, Wedge #2, $\theta=45^\circ$, 3/8 in. Radius Tip) - Photograph and Force-Displacement Graph.

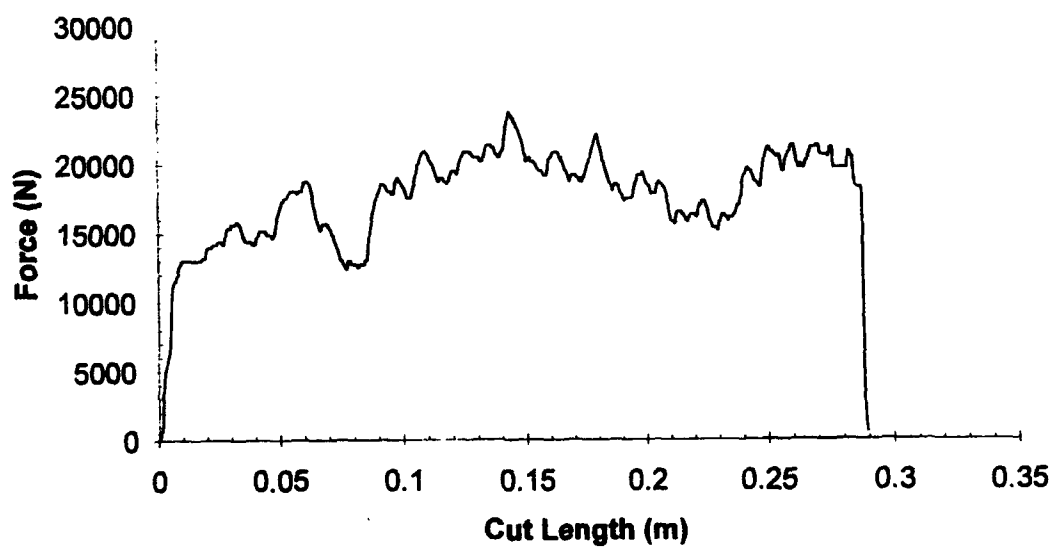


Figure 3.3 Test No. 3 (USDH, Wedge #3, $\theta=30^\circ$, Sharp Tip) - Photograph and Force-Displacement Graph.

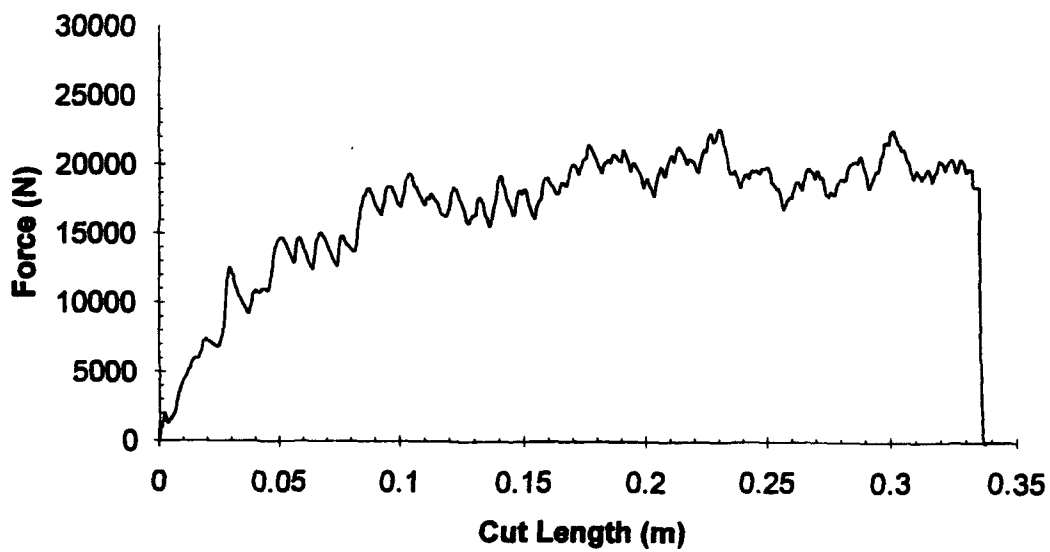


Figure 3.4 Test No. 4 (USDH, Wedge #4, $\theta=30^\circ$, 3/8 in. Radius Tip) - Photograph and Force-Displacement Graph.

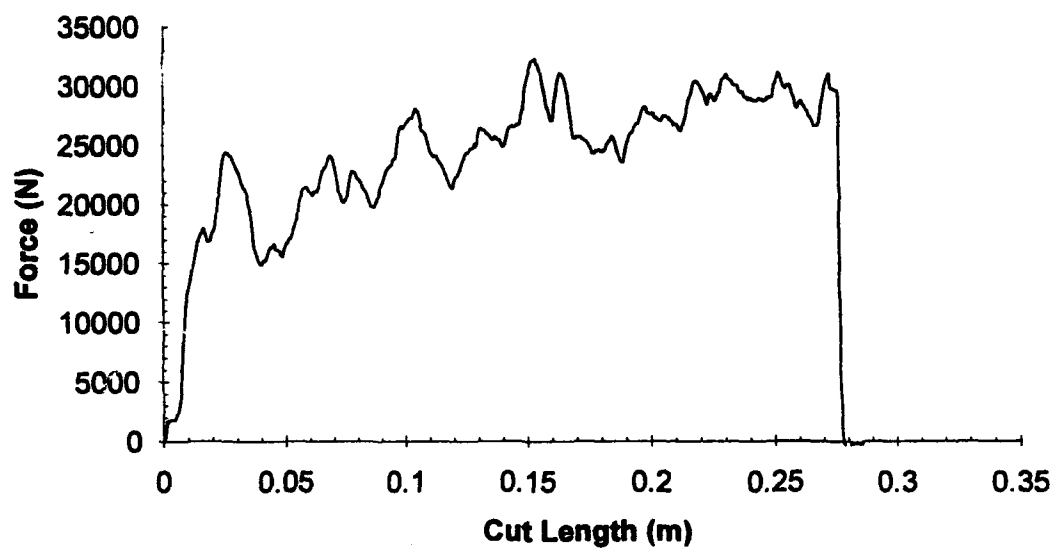


Figure 3.5 Test No. 5 (USDH, Wedge #5, Cylindrical) - Photograph and Force-Displacement Graph.

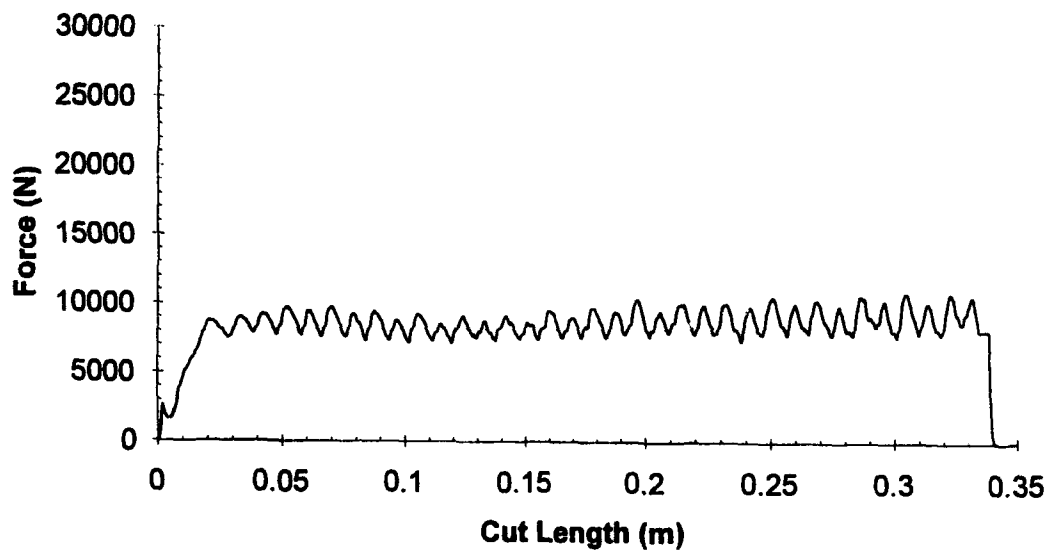
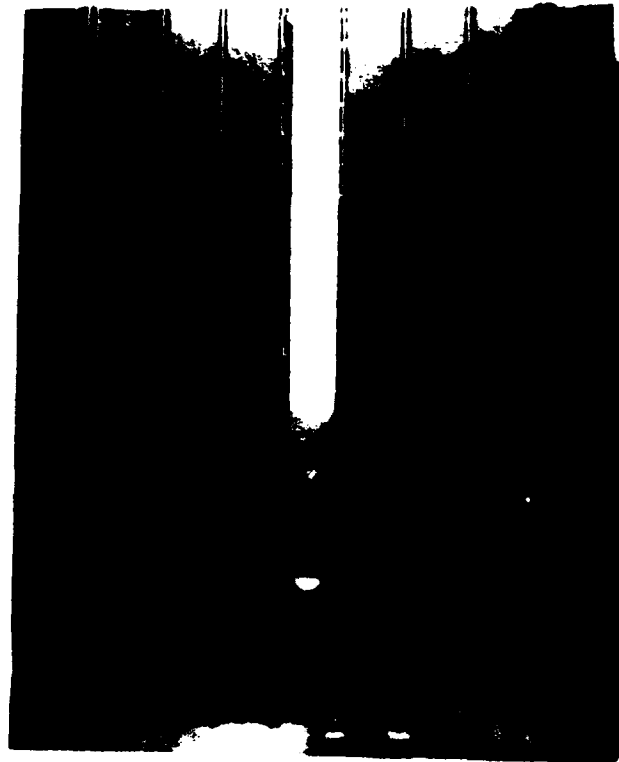


Figure 3.6 Test No. 6 (USDH, Wedge #6, 3/4 in. Wide, $\theta=45^\circ$, 3/32 in. Radius Tip) - Photograph and Force-Displacement Graph.

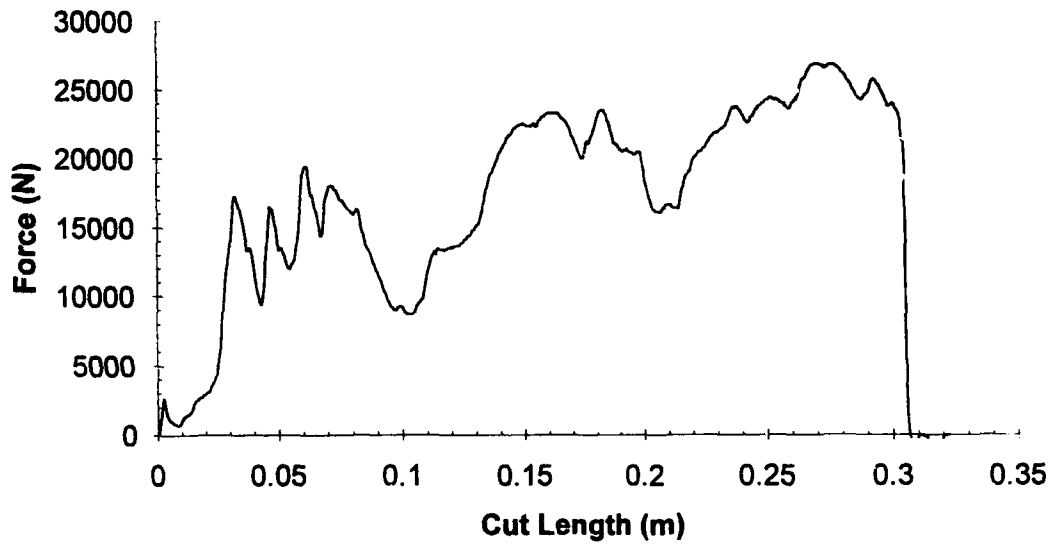


Figure 3.7 Test No. 7 (SH, Wedge #1, $\theta=45^\circ$, Sharp Tip) - Photograph and Force-Displacement Graph.

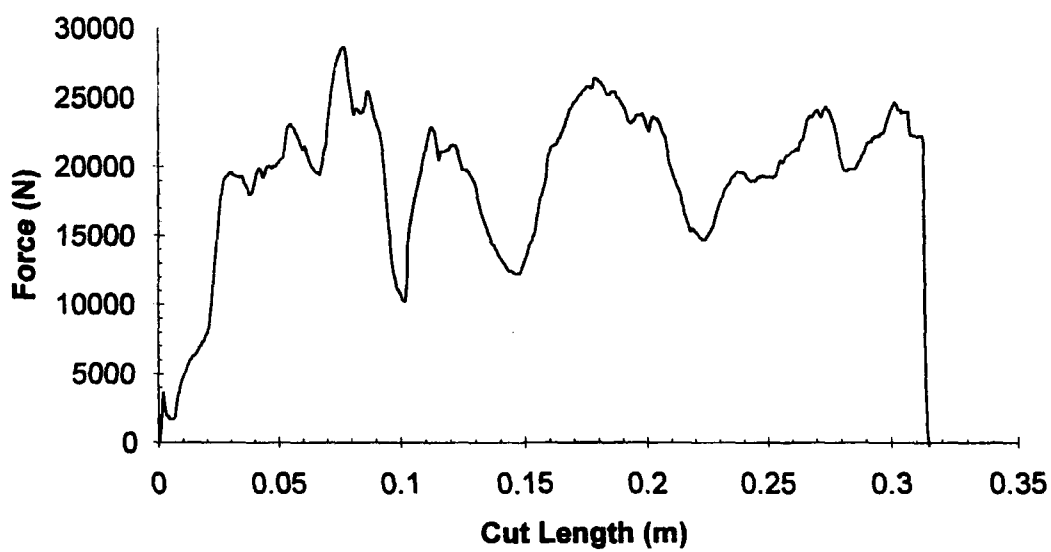


Figure 3.8 Test No. 8 (SH, Wedge #2, $\theta=45^\circ$, 3/8 in. Radius Tip) - Photograph and Force-Displacement Graph.

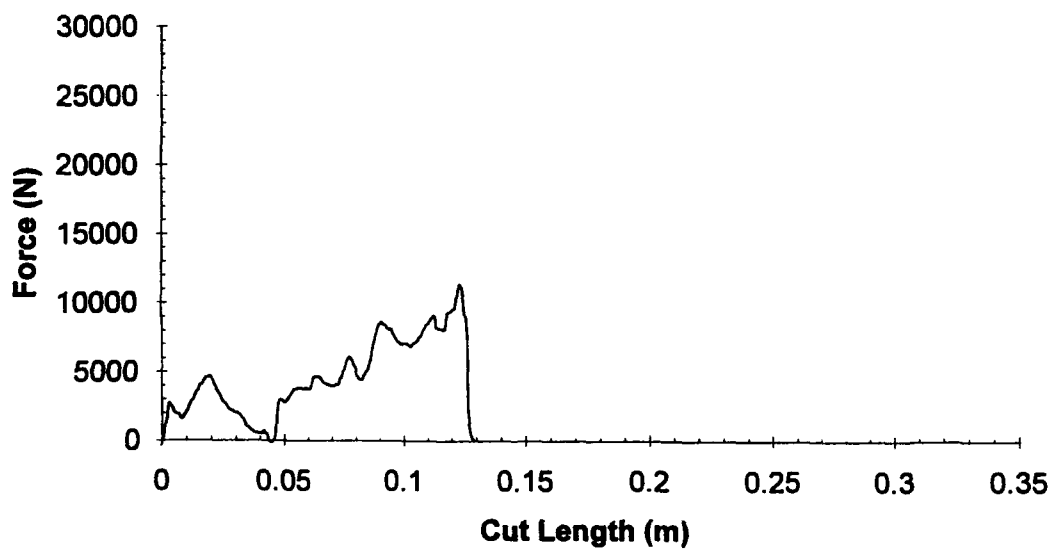
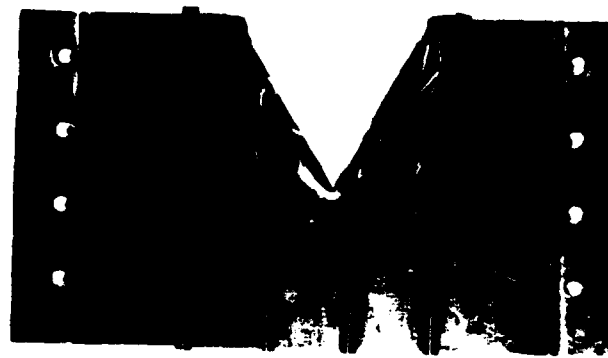


Figure 3.9a Test No. 9a (SH, Wedge #3, $\theta=30^\circ$, Sharp Tip) - Photograph and Force-Displacement Graph.

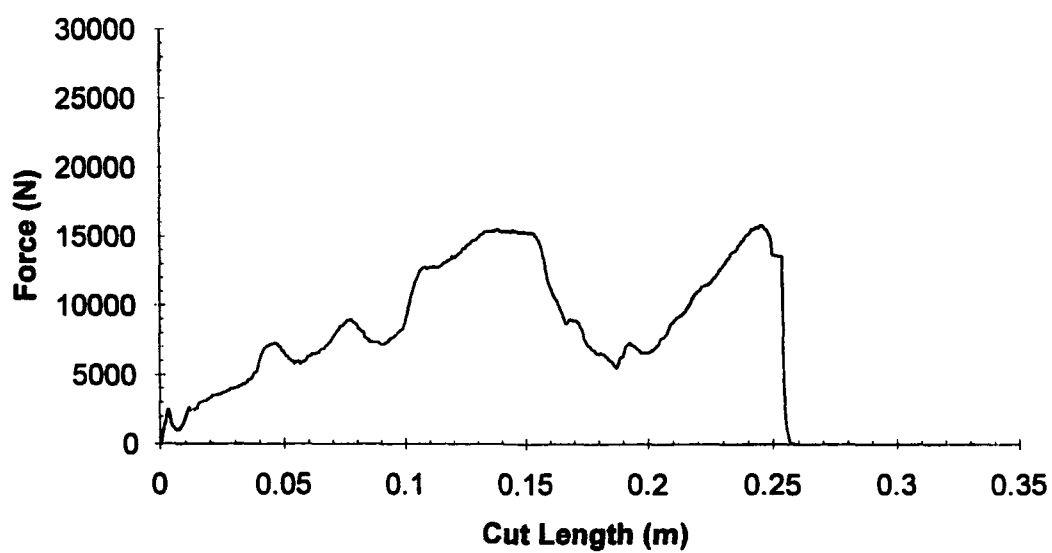
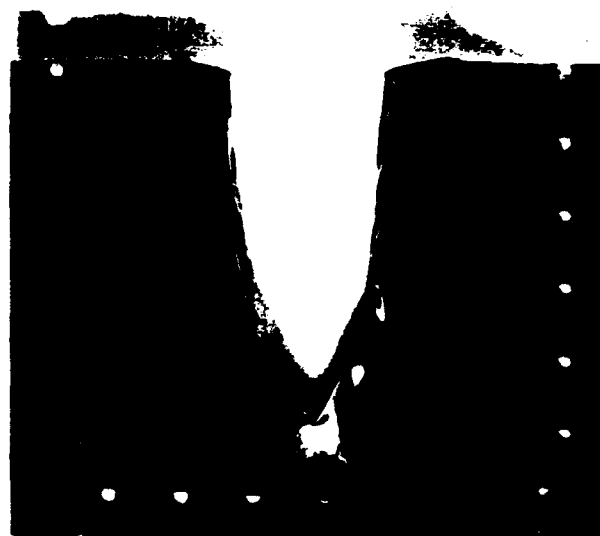


Figure 3.9b Test No. 9b (SH, Wedge #3, $\theta=30^\circ$, Sharp Tip) - Photograph and Force-Displacement Graph.

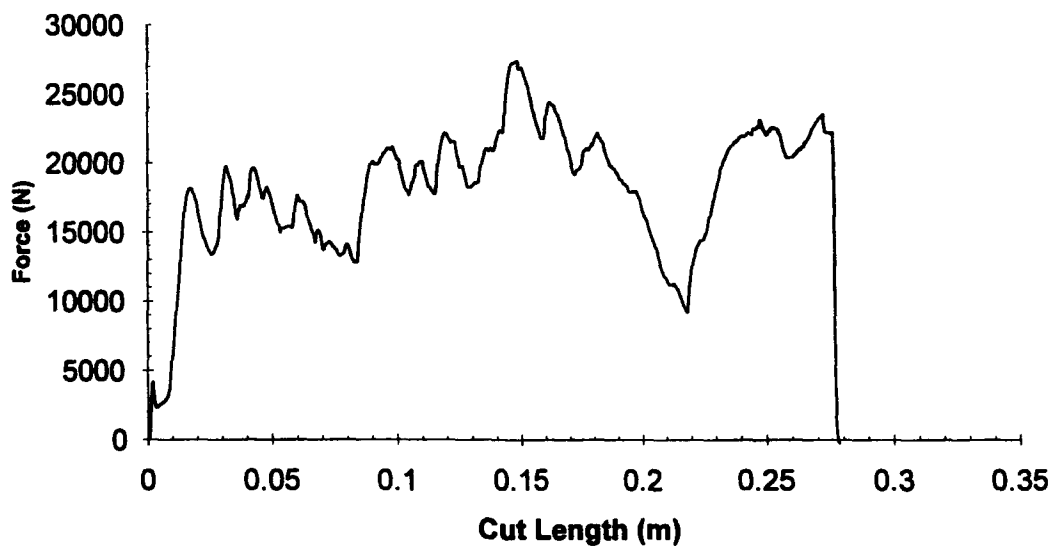


Figure 3.10 Test No. 10 (SH, Wedge #5, Cylindrical) - Photograph and Force-Displacement Graph.

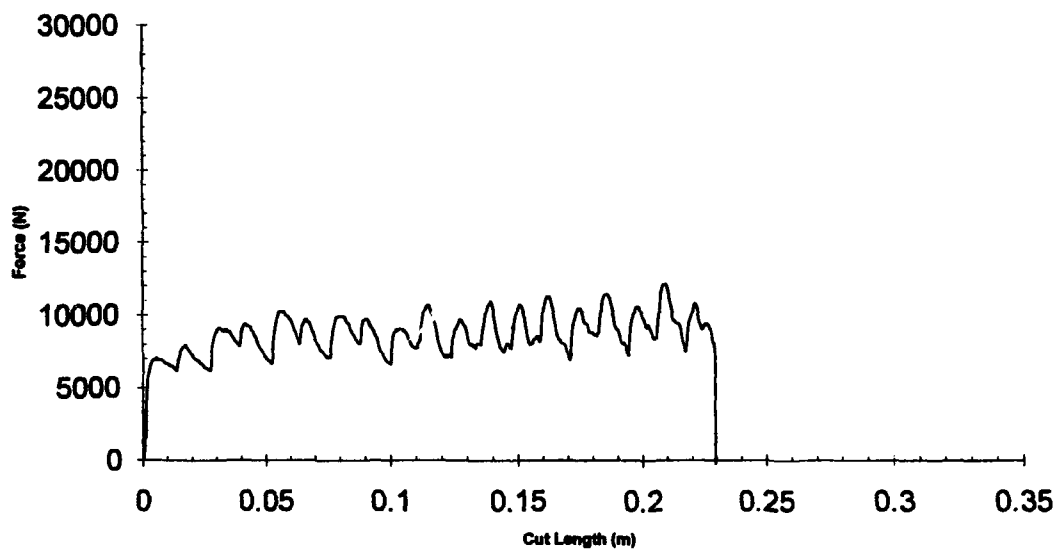


Figure 3.11 Test No. 11 (SH, Wedge #6, 3/4 in. Wide, $\theta=45^\circ$, 3/32 in. Radius Tip) - Photograph and Force-Displacement Graph

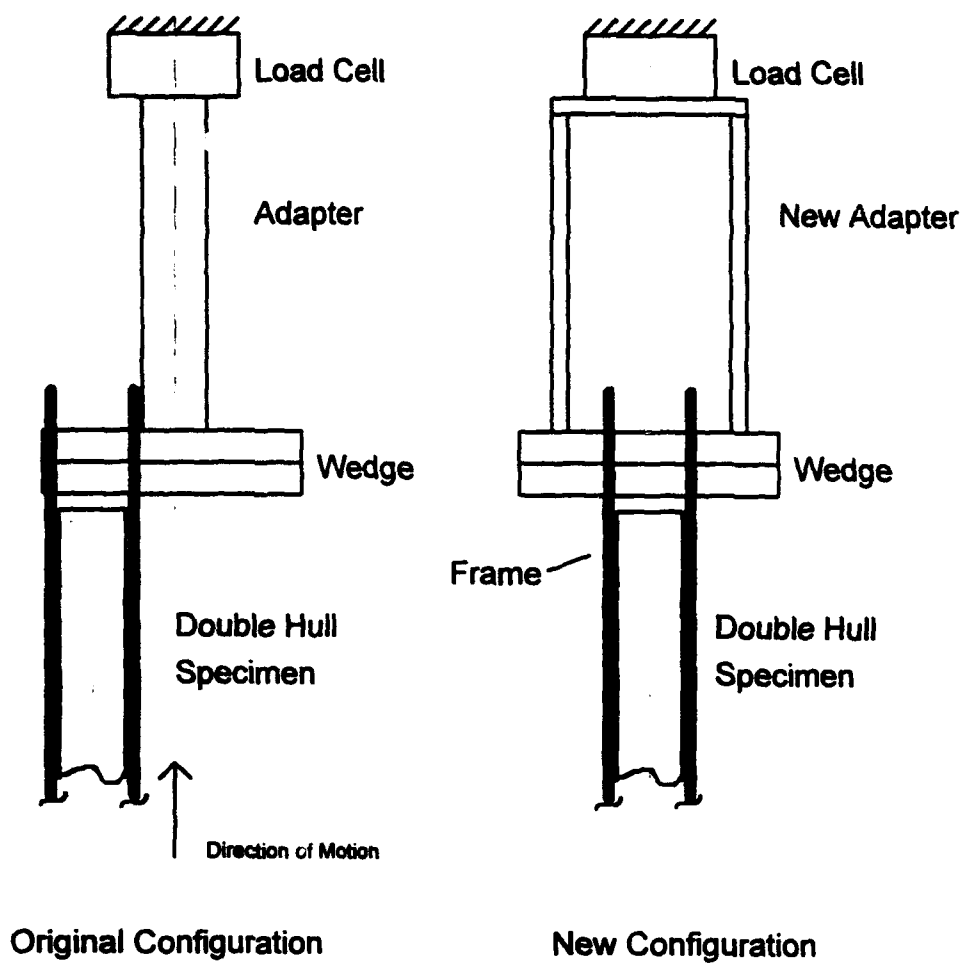


Figure 3.12 Wedge Adapter Modification.

Chapter 4

Theoretical Models and Comparison to Experimental Results

This chapter discusses the formulation of a closed-form analytical solution to the force required to cut a USDH model by a wedge, and applies existing analytical force cutting solutions to the Single Hull model. The results are given here and compared to the experimental results. Supporting calculations are provided in Appendix B.

4.1 General Solution Approach

The approach to finding a closed-form solution for the cutting force is to start by assuming a steady-state deformation mode, and using an incremental deformation in that mode, to find an upper bound to the force required. The following will first consider a Lagrangian formulation which follows a material element, then the results will be expressed in an Eulerian coordinate system which considers material flowing by a fixed point. The knowledgeable reader can skip ahead to the results for internal work rate in bending and membrane of Equation 4.14.

McClintock and Argon (1966) state the upper bound theorem as follows:

In a rigid-plastic continuum, deformation must occur under any system of loads, F_i , for which a distribution of incremental displacements, \dot{u}_i , can be found such that

(a) the displacement boundary conditions, if any, are satisfied,

(b) the displacements can be differentiated to give a strain, $\dot{\epsilon}_{ij}$, with no change in volume anywhere, and

(c) the resulting plastic work done throughout the volume, V , of material, found from the resulting strain, is less than (or equal to) the work done by the external loads acting through the assumed displacements:

$$\int_S F_i \dot{u}_i dS \geq \int_V \sigma_{ij} \dot{\epsilon}_{ij} dV$$

where σ_{ij} are the components of the stress tensor, and $i, j=1,2,3$ in indicial notation.

If it is assumed that in the plate there are no out-of-plane components of displacement or gradient ($u_3 = 0, \frac{\partial}{\partial x_3} = 0$), then $i, j \rightarrow \alpha, \beta = 1, 2$. It turns out that the volume integral can be rewritten in terms of the bending moment times the rate of curvature, $M_{\alpha\beta} \dot{\kappa}_{\alpha\beta}$, and the axial force times the strain rate, $N_{\alpha\beta} \dot{\epsilon}_{\alpha\beta}$, over an area, S , as

$$\int_S F_i \dot{u}_i dS \geq \int_S (M_{\alpha\beta} \dot{\kappa}_{\alpha\beta} + N_{\alpha\beta} \dot{\epsilon}_{\alpha\beta}) dS. \quad (4.1)$$

Note that the bending moment and force tensors, $M_{\alpha\beta}$ and $N_{\alpha\beta}$, are coupled through the yield criterion of the functional form $f(M_{\alpha\beta}, N_{\alpha\beta}) = 0$. It is assumed that in regions experiencing high bending stresses, there are small membrane stresses. Likewise, in regions of high membrane stresses, there are small bending stresses. This decoupling of $M_{\alpha\beta}$ and $N_{\alpha\beta}$ is accomplished by inscribing the yield locus inside a rectangle as in Figure 4.1.

The right hand side of (4.1), can be expressed in the form

$$\dot{W}_{in} = \int_S M_{\alpha\beta} \dot{\kappa}_{\alpha\beta} dS + \int_S N_{\alpha\beta} \dot{\epsilon}_{\alpha\beta} dS. \quad (4.2)$$

The rate of internal plastic work is now the sum of internal bending work rate and membrane work rate, that is

$$\dot{W}_{int} = \dot{W}_b + \dot{W}_m. \quad (4.3)$$

Expansion of the tensor notation in (4.2) gives expressions for the rate of bending and membrane work terms as

$$\dot{W}_b = \int_S (M_{xx} \dot{\kappa}_{xx} + 2M_{xy} \dot{\kappa}_{xy} + M_{yy} \dot{\kappa}_{yy}) dS + \sum_i M_o \dot{\theta}_i l_i \quad (4.4)$$

$$\dot{W}_m = \int_S (N_{xx} \dot{\epsilon}_{xx} + 2N_{xy} \dot{\epsilon}_{xy} + N_{yy} \dot{\epsilon}_{yy}) dS$$

For a rigid-perfectly plastic material, the bending expression contains a continuous deformation field as well as a discontinuous field, where $M_o = \frac{2}{\sqrt{3}} \frac{\sigma_o t^2}{4}$ is the fully plastic bending moment, $\dot{\theta}_i$ is the rate of rotation at the i^{th} plastic hinge and l_i is the length of the hinge line.

In most practical applications, simplified velocity fields are constructed so that plastic bending deformations are contained only in plastic hinges and plane deformations between them. Consequently, the plane rate tensor in the continuous deformation region, S , vanishes ($\dot{\kappa}_{\alpha\beta} = 0$) and (4.4) simplifies to

$$\dot{W}_b = \sum_i M_o \dot{\theta}_i l_i \quad (4.5)$$

$$\dot{W}_m = \int_S (N_{xx} \dot{\epsilon}_{xx} + 2N_{xy} \dot{\epsilon}_{xy} + N_{yy} \dot{\epsilon}_{yy}) dS.$$

Assuming no strain in the y-direction ($\dot{\epsilon}_{yy} = 0$) the associated flow rule gives the yield criterion for the membrane response:

$$\frac{3}{4} N_{xx}^2 + 3 N_{xy}^2 = N_o^2 \quad (4.6)$$

which describes a closed yield curve in the (x,y) plane, where $N_o = \sigma_o t$. To decouple N_{xx} and N_{xy} , idealize the yield curve by inscribing it inside a rectangle as shown in Figure 4.1. Equation 4.5 now becomes

$$\dot{W}_b = \sum_i M_o \dot{\theta}_i l_i \quad (4.7)$$

$$\dot{W}_m = \frac{2}{\sqrt{3}} N_o \int_S \dot{\epsilon}_{xx} dS + \frac{1}{\sqrt{3}} 2 N_o \int_S \dot{\epsilon}_{xy} dS.$$

Conversely, if the largest possible rectangle is inscribed in the yield curve, the stretching and shear coefficients in the membrane term of (4.7) become $2/\sqrt{6}$, and $1/\sqrt{6}$, respectively. Taking the average values of the two idealized yield loci, gives coefficient values of 0.986 and 0.493, respectively. This now provides an estimate rather than a bound.

In the steady-state process, it is convenient to follow a material element along its path relative to the wedge in an Eulerian coordinate system. Consider following an elemental strip over the entire process of bending and membrane. The results comparable

to (4.7) are written in terms of a local (ξ, η) coordinate system, the velocity of the material element, V , the jump in curvatures on both sides of the hinge, $[\kappa] = (\kappa^+ - \kappa^-)$, and the strains as the element stretches on entering and leaving a region, $[\varepsilon] = (\varepsilon^+ - \varepsilon^-)$.

The derivation of the membrane shear term, for example, starts by re-writing the shear strain rate, using a chain rule, as

$$\dot{\varepsilon}_{\xi\eta} = \frac{d\varepsilon_{\xi\eta}}{dt} = \frac{d\varepsilon_{\xi\eta}}{d\xi} \frac{d\xi}{dt}. \quad (4.8)$$

The velocity of the material element can be written as $V = \dot{\xi} = \frac{d\xi}{dt}$, and is constant for a steady-state process for all material elements. Thus,

$$\dot{\varepsilon}_{\xi\eta} = \dot{\xi} \frac{d\varepsilon_{\xi\eta}}{d\xi} = V \frac{d\varepsilon_{\xi\eta}}{d\xi}. \quad (4.9)$$

From the definition, the membrane shear work rate is

$$\dot{W}_{sh} = \frac{2}{\sqrt{3}} N_o \int_S \dot{\varepsilon}_{\xi\eta} dS = \frac{2}{\sqrt{3}} N_o \iint \dot{\varepsilon}_{\xi\eta} d\xi d\eta. \quad (4.10)$$

Substitution of (4.9) into (4.10) and integrating gives

$$\dot{W}_{sh} = \frac{2}{\sqrt{3}} N_o \iint V \frac{d\varepsilon_{\xi\eta}}{d\xi} d\xi d\eta = \frac{2}{\sqrt{3}} N_o \iint V d\varepsilon_{\xi\eta} d\eta = \frac{2}{\sqrt{3}} N_o \int \varepsilon_{\xi\eta} \Big|_{\xi_o}^{\xi_f} V d\eta. \quad (4.11)$$

The strain term is evaluated at the initial and final values of the stretched region as a jump in the strain:

$$\epsilon_{\xi\eta}\big|_{\xi_o}^{\xi_f} = (\epsilon_{\xi\eta}(\xi = \xi_f) - \epsilon_{\xi\eta}(\xi = \xi_o = 0)) = [\epsilon_{\xi\eta}] \quad (4.12)$$

where ξ_f is the end of the zone of active plastic deformation. Substitution of (4.12) into (4.11) gives the final expression for membrane shear work rate

$$\dot{W}_{sh} = \frac{2}{\sqrt{3}} N_o \int [\epsilon_{\xi\eta}] V d\eta. \quad (4.13)$$

Similar derivations are carried out for the remaining terms giving the final result for bending and work rate for steady flow as

$$\dot{W}_b = \sum_i M_o[\kappa]_i V \eta_i \quad (4.14)$$

$$\dot{W}_m = \frac{2}{\sqrt{3}} N_o \int [\epsilon_{\xi\xi}] V d\eta + \frac{2}{\sqrt{3}} N_o \int [\epsilon_{\xi\eta}] V d\eta.$$

In the case of a single applied load F moving at a velocity, V , the external work rate is

$$\dot{W}_{ext} = FV \quad (4.15)$$

4.1.1 USDH Solution

The relatively constant forces of experimental curves of Chapter 3 suggest that the cutting of the USDH specimen is nearly steady-state. The increasing force in the

beginning of the curve is considered a transition region and is ignored. The USDH specimens were examined after testing to determine an acceptable model. Many models could be devised, but the goal was to pick a model that would enable the analysis to be simplified. A key assumption is made in the geometry of the USDH structure: the thickness of the longitudinal girder is of the same order of magnitude as the hull plating, and the longitudinal girder height is of the same order as the spacing between longitudinals.

Zheng and Wierzbicki (1994) showed, in the steady-state cutting force solution of a single plate, that a simplified model of deforming flat material segments approximates the more rigorous solution of continuously deforming material to within 5%. (However, their formulation appears to assume a batch type process, whereas the method here is to assume a steady flow process.) The final USDH model is shown in Figure 4.2, where the shaded region is the deformed area to be analyzed. The model assumes that the material between the inner two longitudinals folds in the concertina mode under the wedge tip. The gap is a conceptual representation of the accumulation of material due to membrane stretching as the wedge progresses. The plate has clamped boundary conditions at the ends and sides. If one follows a material element past the wedge in Figure 4.3, one sees that the material bends at hinge lines and then is stretched as it passes around the wedge shoulder. In the assumed strain field, the material must then return to its original length by recompression or buckle out of plane after it passes the shoulder.

As shown in Figure 4.4, the wedge progresses into the specimen, cutting symmetrically down the center of one cell, laterally pushing the inner two longitudinals and deforming the associated plating. The deformed section is shown in Figure 4.5. The wedge width is B , and the longitudinal spacing is b . The lateral distance that the wedge deforms the plate and longitudinal is given by

$$\Delta = \frac{1}{2}(B - b). \quad (4.16)$$

In this analysis, the wedge width is constrained by $b < B < 3b$, ensuring only three cells are deformed by the wedge.

The plating is damaged in three sections. The first section is the concertina tearing of the plate between the inner two longitudinals. The second section is triangular with a opposite side length of Δ , an adjacent side length of ζ , and an undeformed angle equal to the wedge semi-angle, θ . This triangle is bent and folded out-of-plane forming two new triangles each having an opposite side length of $\Delta/2$. The angles formed are α_1 and α_2 , where $\theta = \alpha_1 + \alpha_2$. The third section is parallel to the wedge shoulder and is bent out of plane and folded into two segments each $\Delta/2$ high by ζ long. Figure 4.5 shows the idealized model compared to the photograph of the end view of a deformed USDH specimen.

Given B , b , and θ , the following parameters can be determined from the geometry of the problem:

$$\begin{aligned} \zeta &= \frac{\Delta}{\tan \theta} \\ \alpha_1 &= \tan^{-1} \left(\frac{\Delta}{2\zeta} \right) \\ \alpha_2 &= \theta - \tan^{-1} \left(\frac{\Delta}{2\zeta} \right) \end{aligned} \quad (4.17)$$

4.1.1.1 Internal Work Rate in Bending

The internal work rate in bending assumes that the material flows and is bent and unbent through some curvature at two stationary hinge lines, η_1 and η_2 , as shown in Figure 4.6. The material region can be divided into regions 1 and 2. Using the bending term of (4.14), the bending work rate is written as

$$\dot{W}_b = M_o (\eta_1 [\kappa]_1 V_1 + \eta_2 [\kappa]_2 V_2). \quad (4.18)$$

Following a material element moving at velocity $V = \dot{\xi}$ in region 1, the material must first bend at η_{1a} , then again at η_2 . The material in region 2 bends only at η_{1b} . The velocity components normal to the hinge lines contribute in (4.18). From the geometry, and in terms of the radii of the bends, r_1 and r_2 (which are estimated later), (4.18) becomes

$$\dot{W}_b = M_o \left(2 \frac{\Delta}{\sin \theta} \left(\frac{1}{r_1} - \frac{1}{-r_1} \right) V \sin \theta + \frac{\Delta}{2 \sin \alpha_1} \left(\frac{1}{r_2} - \frac{1}{-r_2} \right) V \sin \alpha_1 \right), \quad (4.19)$$

which upon simplification gives a final expression for the rate of work in bending

$$\dot{W}_b = \frac{2}{\sqrt{3}} \frac{\sigma_o t^2}{4} V \Delta \left(\frac{4}{r_1} + \frac{1}{r_2} \right). \quad (4.20)$$

4.1.1.2 Internal Work Rate in Membrane Stretching

The membrane stretching is shown as the shaded area in Figure 4.7. The internal work rate in stretching from (4.14) is

$$\dot{W}_{str} = \frac{2}{\sqrt{3}} N_o \int [\epsilon_{\xi\xi}] \dot{\xi} d\eta. \quad (4.21)$$

The displacement function $u(\eta)$, describing the stretched region, varies along the η axis. The velocity of the material $\dot{\xi}$ is written can be written as $\dot{\xi} = V$. The jump in strain is the displacement over the original length ζ , that is, $[\epsilon] = (\epsilon^+ - \epsilon^-) = \frac{u(\eta)}{\zeta}$. Substitution of these results and $N_o = \sigma_o t$ into (4.21) gives

$$\dot{W}_{str} = \frac{2}{\sqrt{3}} \sigma_o t \frac{V}{\zeta} \int_0^{\Delta} u(\eta) d\eta. \quad (4.22)$$

The maximum displacements between points A and B is u_a , and between points C and D is u_b , as shown in the projected segment view in Figure 4.8 are determined to be

$$u_a = \zeta \left(\frac{1}{\cos\theta \cos\alpha_2} - \frac{1}{\cos\alpha_1} \right) \quad (4.23)$$

$$u_b = \sqrt{\left(\frac{\Delta}{2} - \zeta \frac{\sin\alpha_2}{\cos\alpha_1} \right)^2 + \left(\zeta \left(\frac{1}{\cos\theta} - \frac{\cos\alpha_2}{\cos\alpha_1} \right) \right)^2}$$

The displacement over the stretched area is expressed as

$$u(\eta) = \frac{1}{\Delta} \left[\int_0^{\Delta/2} u_1(\eta) d\eta + \int_{\Delta/2}^{\Delta} u_2(\eta) d\eta \right] \quad (4.24)$$

where $u_1(\eta)$ and $u_2(\eta)$ are determined from the geometry as

$$u_1(\eta) = \left(\frac{u_a - u_b}{\Delta/2} \right) \eta + u_b \quad (4.25)$$

$$u_2(\eta) = \frac{-u_a}{\Delta/2} (\eta - \Delta).$$

Substitution of (4.25) into (4.24) and integrating results in

$$u(\eta) = \frac{1}{2} u_a + \frac{1}{4} u_b. \quad (4.26)$$

Substituting this result into (4.22) and integrating gives the final expression for the internal rate of work in membrane stretching

$$\dot{W}_{sr} = \frac{1}{\sqrt{3}} \sigma_o t V \frac{\Delta}{\zeta} \left(u_a + \frac{1}{2} u_b \right). \quad (4.27)$$

4.1.1.3 Internal Work Rate in Membrane Shear

To ensure kinematic admissibility of the model, the gap between points *C* and *D* must be closed. One way to do this is by shearing of the plate. Figure 4.9 shows the geometry of the material that is assumed to be under shear. The shear work rate is given from (4.14) as

$$\dot{W}_{sh} = \frac{2}{\sqrt{3}} N_o \int [\varepsilon_{\xi\eta}] V d\eta. \quad (4.28)$$

The jump in shear strain is approximated as

$$[\varepsilon_{\xi\eta}] = (\varepsilon_{\xi\eta}^* - 0) = \varepsilon_{\xi\eta} = \frac{1}{2}(u_{\xi,\eta} + u_{\eta,\xi}) \cong \frac{1}{2}\phi \quad (4.29)$$

where $\phi = \tan^{-1}\left(\frac{u_b}{b-\Delta}\right)$. Substituting (4.29), and $N_o = \sigma_o t$, in (4.28) gives

$$\dot{W}_{sh} = \frac{2}{\sqrt{3}}\sigma_o t \int_0^{(b-\Delta)} \frac{1}{2}\phi V d\eta, \quad (4.30)$$

which upon integration, gives the final expression for the work rate in shear as

$$\dot{W}_{sh} = \frac{\sigma_o t}{\sqrt{3}}(b-\Delta)V \tan^{-1}\left(\frac{u_b}{b-\Delta}\right) \quad (4.31)$$

4.1.1.4 Concertina Tearing Force

Wierzbicki (1994) has solved for the force required for concertina tearing mode of a plate. The mean concertina indentation force has been calculated as

$$F_{concertina} = 4\sigma_o t^{5/3} b^{1/3} + \frac{8}{3}Rt \quad (4.32)$$

where R is the specific work of fracture (i.e. fracture toughness), characterizing the tearing resistance of plates and sheet metal structures, reported by Wierzbicki from the work of Atkins (1988). For mild steel, the specific work of fracture is in the range

$$R \approx 300 \text{ to } 1000 \text{ N/mm.}$$

The actual value of R , for a particular material, must be determined experimentally. This is not done here, rather a value in the range is assumed.

4.1.1.5 Contribution of Friction

Inspections of the USDH specimens showed scored and rubbed surfaces where the wedge made contact. This leads to the conclusion that friction must be included in the formulation of cutting force. It is obvious that there is no friction in the concertina tearing mode. The contribution of friction to the total force is found by finding the force tangent to the wedge face and then projecting that force in the direction of applied force:

$$F_f = \frac{\mu F_p}{\sin \theta} \cos \theta \quad (4.33)$$

where F_p is the force determined from the plastic work in bending, membrane, and shear as

$$F_p = \frac{1}{V} (\dot{W}_b + \dot{W}_{str} + \dot{W}_{sh}), \quad (4.34)$$

and μ is the coefficient of sliding friction. The total internal resistance to cutting becomes the sum of the force to plastically deform the section and the friction force

$$F_{pf} = F_p + F_f = F_p \left(1 + \frac{\mu}{\tan \theta} \right) = \frac{1}{V} (\dot{W}_b + \dot{W}_{str} + \dot{W}_{sh}) \left(1 + \frac{\mu}{\tan \theta} \right). \quad (4.35)$$

4.1.1.6 Total Steady-State Cutting Force

The total cutting force is determined by assembling the above expressions. There is only a single applied load in the cutting of the specimens, therefore the rate of external work is greater than or equal to the total rate of internal work:

$$FV \geq F_{pf} V, \quad (4.36)$$

which upon substitution of (4.35) yields

$$FV \geq (\dot{W}_b + \dot{W}_{str} + \dot{W}_{sh}) \left(1 + \frac{\mu}{\tan \theta} \right). \quad (4.37)$$

The minimum upper bound force of bending, membrane, and shear (excluding the concertina tearing force) can be expressed as

$$F = \frac{1}{V} (\dot{W}_b + \dot{W}_{str} + \dot{W}_{sh}) \left(1 + \frac{\mu}{\tan \theta} \right) \quad (4.38)$$

which, when the force in concertina tearing is added, becomes

$$F = \frac{1}{V} (\dot{W}_b + \dot{W}_{str} + \dot{W}_{sh}) \left(1 + \frac{\mu}{\tan \theta} \right) + F_{concertina}. \quad (4.39)$$

In the experiments there were four identical deformed sections, and two concertina tearing surfaces, so the total force becomes

$$F = \frac{4}{V} (\dot{W}_b + \dot{W}_{str} + \dot{W}_{sh}) \left(1 + \frac{\mu}{\tan \theta} \right) + 2F_{concertina} \quad (4.40)$$

Substitution of (4.20), (4.27), (4.31), and (4.32) into (4.40), and noting that the velocity, V , cancels out, gives a final expression for the total steady-state cutting force for the USDH model

$$F = 4\sigma_o t \left(1 + \frac{\mu}{\tan \theta} \right) \left[\frac{2}{\sqrt{3}} \frac{t}{4} \Delta \left(\frac{4}{r_1} + \frac{1}{r_2} \right) + \frac{1}{\sqrt{3}} \frac{\Delta}{\zeta} \left(u_a + \frac{1}{2} u_b \right) + \frac{(b - \Delta)}{\sqrt{3}} \tan^{-1} \left(\frac{u_b}{b - \Delta} \right) \right] + \left[8\sigma_o t^{5/3} b^{1/3} + \frac{16}{3} R t \right] \quad (4.41)$$

valid for $b < B < 3b$.

If $b \geq B$, then it is required that $\Delta \equiv 0$ (from geometry), resulting in $\dot{W}_b = \dot{W}_{str} = \dot{W}_{sh} = 0$ which reduces Equation (4.40) to $F = 2F_{concertina}$.

4.2 Application of Existing Solutions to the Longitudinally Stiffened Single Hull

In the longitudinally stiffened single hull model, both a plate tearing initiation solution (Wierzbicki and Thomas (1993)) and a steady-state plate cutting solution (Zheng and Wierzbicki (1994)) is applied. Both are for single plates, but will be applied by smearing the stiffened single hull into a plate with equivalent thickness. (Wierzbicki and Zheng's (1993) cutting initiation solution with cutting at the crack tip rather than tearing is not used since the specimens were observed to tear at the wedge tip rather than being cut.)

An attempt was made to estimate the wedge force from the fully plastic torsion of a single longitudinal. An order-of-magnitude comparison of the fully plastic twisting moment of a stiffener compared to the fully plastic bending moment of the stiffener, plate, and stiffener/plate combination showed that the bending of the stiffener/plate combination is nearly two orders-of-magnitude greater than the torsion of the stiffener (see Appendix B). This order-of-magnitude analysis shows that the stiffener and plate cannot be modeled independently, but must be modeled as a unit. Inspection of the tested single hull specimens showed very complex failure modes with double curvatures in bending and tripping of the longitudinals, therefore, a simple theoretical model was not attempted. Instead a simplified approach was used based on the concept of an equivalent thickness.

4.2.1 Wierzbicki and Thomas' Plate Tearing Initiation Solution

The stiffeners and plating can be smeared to give an equivalent plate thickness, t_{eq} , by the equation

$$t_{eq} = \frac{A}{b} + t_p \quad (4.42)$$

where A is the cross sectional area of the stiffener, b is the spacing between stiffeners, and t_p is the hull plating thickness. The single hull model force-displacement curves, of Chapter 3, exhibit much variation in the force level over the length of cut, l , so they were integrated to obtain a work-displacement curve. Equation 1.8 was integrated to give the energy as

$$W_t = 1.19 \sigma_o (\bar{\delta}_t)^{0.2} l^{1.4} t_{eq}^{1.6} (\cos \theta)^{-0.8} \left[(\tan \theta)^{0.4} + \mu (\tan \theta)^{-0.6} \right] \quad (4.43)$$

4.2.2 Wierzbicki and Zheng's Steady-State Plate Cutting Solution

In a similar manner, the steady-state force from (1.14) was multiplied by the length of cut, l , to give an expression for the steady-state work required in cutting

$$W_{ss} = \frac{2}{\sqrt{3}} \frac{\sigma_o t_{eq}^2}{4} \left(2 \frac{B}{t_{eq}} \sin \theta \tan \theta + 3\pi \right) \left(1 + \frac{\mu}{\tan \theta} \right) l \quad (4.44)$$

4.3 Comparison of Experiments to Theory

This section compares the experimental results to the theoretical solutions of the USDH steady-state cutting force Equation 4.41, the single hull plate tearing initiation solution of (4.43), and the single hull steady-state cutting solution of (4.44).

4.3.1 USDH Comparison

Only two USDH experiments, Tests 2 and 4, exhibited the pure concertina cutting mode of the plate material under the wedge tip. The remaining tests resulted in mixed modes of central separation on one side and concertina on the other, or just pure cutting of both plates. However, the theoretical result of (4.41) is compared to all the experiments. The detailed calculations are shown in Appendix B.

For the experiments, the cell spacing b , wedge width B , and plate thickness t , are

$$\begin{aligned}
b &= 41.7 \text{ mm} \\
B &= 76.2 \text{ mm} \\
t &= 0.749 \text{ mm}
\end{aligned}$$

The coefficient of sliding friction is typically 0.15 to 0.3, and is assumed to be $\mu=0.3$. The local specific work of fracture in the concertina mode is assumed to be $R = 650 \text{ N/mm}$, which is the average value over the range. The flow stress is given by estimating the average strain in membrane and bending and using the stress-strain curves of Appendix C, as follows.

For membrane stretching, the average strain is estimated as

$$\epsilon_{str} = \frac{u(\eta)}{\zeta}. \quad (4.45)$$

For membrane shear, the average strain is estimated from (4.29) as

$$\epsilon_{sh} = \frac{1}{2} \phi. \quad (4.46)$$

For bending, the average strain is estimated as

$$\epsilon_b = \frac{t}{4r}, \quad (4.47)$$

where r is the bending radius. Assuming the strain contributions are equal, the total average strain throughout the deformation process is then estimated as

$$\epsilon_{ave} = \frac{\epsilon_{b1} + \epsilon_{b2} + \epsilon_{str} + \epsilon_{sh}}{4} = \frac{1}{4} \left(\frac{t}{4r_1} + \frac{t}{4r_2} + \frac{u(\eta)}{\zeta} + \frac{1}{2} \phi \right). \quad (4.48)$$

The unknown radii are estimated from inspection of the USDH specimens as

$$\begin{aligned} r_1 &= 10t \\ r_2 &= 3t. \end{aligned} \tag{4.49}$$

Wedge Semi-angle, $\theta=45^\circ$ - The average strain is calculated as

$$\epsilon_{ave} = \frac{0.025 + 0.083 + 0.282 + 0.133}{4} = 0.131$$

Using the stress-strain curves from Appendix C, the flow stress is approximately $\sigma_o = 318$ N/mm². The values are substituted into Equation 4.41 giving a steady-state cutting force of $F = 24,142$ N.

Wedge Semi-angle, $\theta=30^\circ$ - The average strain is calculated as

$$\epsilon_{ave} = \frac{0.025 + 0.083 + 0.112 + 0.090}{4} = 0.078$$

This strain corresponds to a flow stress of $\sigma_o = 298$ N/mm². Equation 4.41 yields a steady-state cutting force of $F = 19,136$ N.

The comparison of the above results to the experiments are shown in Figures 4.10 through 4.14 (in the same order as presented in Chapter 3). For each test, a force-displacement curve and a work-displacement curve is plotted. The mean force is plotted on the force-displacement curve in the region estimated to be steady-state cutting. The transition from initiation to steady-state cutting is denoted l^* and is estimated by inspection of the experimental force-displacement curves. The experimental mean steady-

state cutting force F_m is calculated by integrating the area under the steady-state portion of the force curve and then dividing by the length of steady-state cutting interval (l^* to l_f):

$$F_m = \frac{\int_{l^*}^{l_f} F_{exp} dl}{(l_f - l^*)}, \quad (4.50)$$

where F_{exp} is from the experimental force data. Table 4.1 summarizes the comparison of experiments and theory. The error is calculated by $error(\%) = 100(F - F_m)/F_m$.

Table 4.1 Comparison of USDH Experiments and Theory.

Test No.	Wedge Semi-angle θ	Steady-state Transition l^* (m)	Experimental Mean Force F_m (N)	USDH Theory F (N)	Error (%)	Figure No.
1	45°	0.15	22,792	24,142	+5.9	4.10
2	45°	0.05	23,299	24,142	+3.6	4.11
3	30°	0.10	19,128	19,136	+0.04	4.12
4	30°	0.075	18,814	19,136	+1.7	4.13
5	45°	0.10	27,434	24,142	-12.0	4.14

For Test 5, the semi-angle of 45° was assumed based on the geometry of a circle. Taking one quadrant of a circle and drawing a line from the two perpendicular radii gives a 45° right triangle. The higher mean force of Test 5 is most likely due to some other cutting mechanism that takes more work than observed in the previous tests.

(Note that the calculated concertina force (shown in Appendix B) is between 7,704 and 8,046 N. The calculated mean force of Test 6 (Figure 3.6) is 8,647 N. The correlation is within -7.0 to -10.9%.)

4.3.2 Single Hull Comparison

This section compares the solutions of initiation and steady-state cutting, Equations 4.43 and 4.44, respectively, for Tests 7, 8, 9b, and 10 of Chapter 3. Both the force-displacement and work-displacement curves are shown for each experiment.

The point where Equations 4.43 and 4.44 intersect, denoted l^* , is the transition from initiation to steady-state cutting. That is, the cutting process follows (4.43) until l^* , at which steady-state cutting ensues, and then (4.44) is followed. This is shown in Figure 4.15.

In the single hull specimens, three material thicknesses were used each having different yield and ultimate stresses as shown in the stress-strain curves in Appendix C. An average flow stress can be determined from Hughes (1988) as

$$\sigma_o = \frac{\sigma_{ow}A_w + \sigma_{of}A_f + \sigma_{op}bt_p}{A_w + A_f + bt_p}, \quad (4.51)$$

which is in terms of the cross sectional areas of the web, flange, and plate and the associated flow stress for each material used in these members.

The crack opening displacement parameter is assumed to be $\bar{\delta}_l = 1.0$ (this is consistent with the work of Wierzbicki and Thomas (1993) who showed that the solution has weak dependence on the COD parameter).

The average strain throughout the cutting process is assumed to be between 10 and 15%. With this strain range, and using the stress-strain curves of Appendix C, the average flow stress range using (4.51) is 309 to 318 N/mm². Since this range is small, the flow stress is assumed as the average of the range, $\sigma_o = 314$ N/mm². Using (4.42), the equivalent thickness is $t_{eq} = 2.01$ mm. The assumed coefficient of friction is $\mu = 0.3$.

For each test, a force- and work-displacement graph is shown with (1.8) and (4.43) plotted, respectively. An average mean force was not found since the experiments do not reach steady-state cutting. Rather, the accuracy of the theory to the experiments is based on comparing the work-displacement curves at a length of cut $l_f = 0.25m$ for each experiment. The transition point, l^* , calculated for each experiment was beyond the extent of cutting showing that none of the experiments reached steady state cutting. This was also observed in the force-displacement curves. Table 4.2 summarizes the comparison of experiments and theory.

Table 4.2 Comparison of Single Hull Experiments and Theory.

Test No.	Wedge Semi-angle θ	Steady-state Transition l^* (m)	Final Cut Length l_f (m)	Experimental Work $W(l_f)$ (Nm)	SH Theory $W_f(l_f)$ (Nm)	Error (%)	Figure No.
7	45°	0.641	0.25	3,968	4,455	+12.3	4.16
8	45°	0.641	0.25	4,661	4,455	-4.4	4.17
9b	30°	0.29	0.25	2,291	3,554	+55.1	4.18
10	45°	0.641	0.25	4,433	4,455	+0.5	4.19

The worst case is Test 9b with an error of +55.1%. This is due to a poor experiment as discussed in Chapter 3. As such, this test result and comparison is discarded with a recommendation that the test be repeated.

For completeness, the concertina tearing force for the single hull specimen of Test 11 (Figure 3.11) was calculated as $F_{concertina} = 7,755N$ using as inputs

$$\sigma_o = 314 N / mm^2$$

$$R = 650 N / mm$$

$$b = 53.34 mm$$

$$t = 1.130 mm.$$

The mean force in the experiment was calculated as 8,895 N. The accuracy is -12.8%.

4.4 Parametric Study of the USDH Steady-state Cutting Force Solution

There are four primary parameters that are imbedded in Equation 4.41 and warrant a graphical parametric study to determine the cutting force solution behavior. They are the wedge width, B , wedge semi-angle, θ , and the coefficient of sliding friction, μ , and the plate thickness, t . The non-varying values used were those of section 4.3.1, namely

$$\sigma_o = 318 N / mm^2$$

$$R = 650 N / mm$$

$$b = 41.7 mm.$$

Wedge Width, B - This parameter was varied from b to $3b$, which is the range of validity of the solution. When $B=b$, then the wedge cuts between two longitudinals in the concertina mode only. As B increases, the force increases as would be expected by the wedge having to deform more plating as it progresses. See Figure 4.20.

Wedge Semi-angle, θ - This parameter was varied from 20 to 80 degrees. As the wedge becomes blunter with increasing semi-angle, the force increases rapidly as would

be expected. This is demonstrated by the increased force using the cylindrical wedge. See Figure 4.21. Physically this means that for larger θ some other failure mechanism must take over, for example, concertina tearing.

Coefficient of Sliding Friction, μ - The solution has a weak dependence on μ . The force is increased $\sim 10\%$ going from $\mu = 0.15$ to 0.30 . See Figure 4.22.

Plate Thickness, t - The force increases linearly due to the deformation term of (4.41) and proportional to $t^{3/3}$ due to the concertina tearing term. See Figure 4.23.

4.5 Alternative Failure Modes Assuming USDH Weld Failure

The welds did not fail in any of the USDH cutting experiments. The steady-state cutting force solution of Equation 4.41 assumes that the longitudinal girders do not separate from the plating. The longitudinals enter into the solution in the assumed kinematic model, but not explicitly as a parameter.

Consider that the welds fail and the inner two longitudinal girders separate from the plating. The next outer set of longitudinals now provide the boundary condition and the inner two are free to deform independent of the hull plating. If that is the case, other failure modes must occur. Two possible failure modes are the concertina tearing of the plating, or the steady-state cutting of the plating.

Concertina Mode - The spacing between the longitudinal girders is now $3b$. Using the following parameters

$$\sigma_o = 310 \text{ N} / \text{mm}^2$$

$$t = 0.749 \text{ mm}$$

$$b = 3 \times 41.7 \text{ mm} = 125.1 \text{ mm}$$

$$R = 650 \text{ N} / \text{mm}$$

Equation 4.32 is evaluated for the cutting of both plates as $F_{concertina} = 10,259 \text{ N}$.

Steady-State Cutting - Equation 1.14 is used to evaluate the steady-state cutting force F_{ss} where the wedge width is $B = 76.2 \text{ mm}$. The flow stress and plate thickness are the same as above. The steady-state cutting force of both plates for two wedge semi-angles is evaluated as

- $\theta=45^\circ$: $F_{ss} = 20,009 \text{ N}$

- $\theta=30^\circ$: $F_{ss} = 10,405 \text{ N}$.

The force levels for concertina tearing and steady-state plate cutting are less than the USDH steady-state cutting solution and the experimental mean force level. Therefore, when considering the failure of welds and other plate cutting modes, the force levels provide a lower bound to the USDH solution presented in this thesis. Table 4.3 provides a comparison of results.

Table 4.3 Force Level Comparison for Alternative USDH Failure Modes.

Test No.	Wedge Semi-angle θ	Concertina Force $F_{concertina} \text{ (N)}$	Steady-State Cutting Force $F_{ss} \text{ (N)}$	Experimental Mean Force $F_m \text{ (N)}$	USDH Theory $F \text{ (N)}$
1	45°	10,259	20,009	22,792	24,142
2	45°	10,259	20,009	23,299	24,142
3	30°	10,259	10,405	19,128	19,136
4	30°	10,259	10,405	18,814	19,136
5	45°	10,259	20,009	27,434	24,142

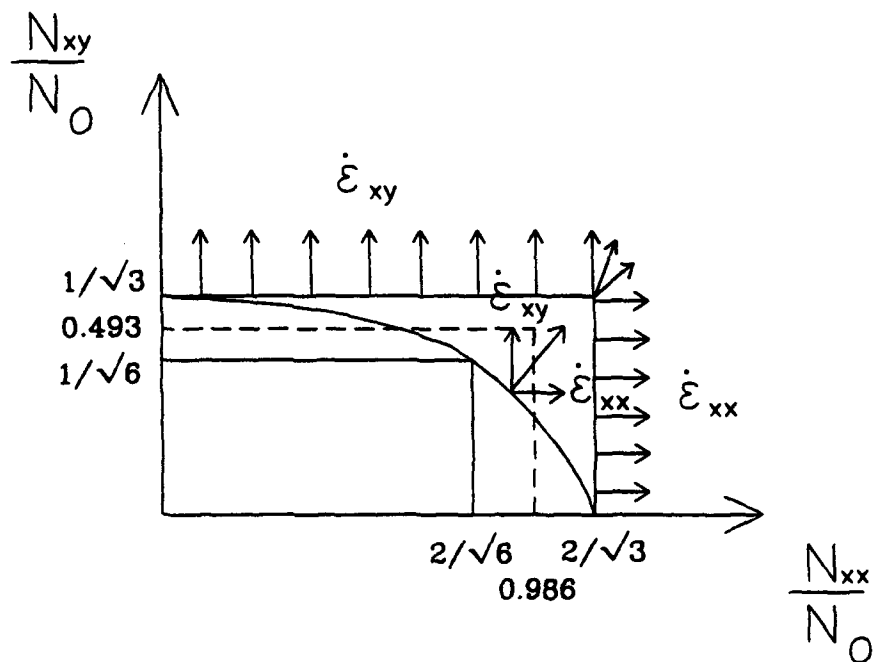
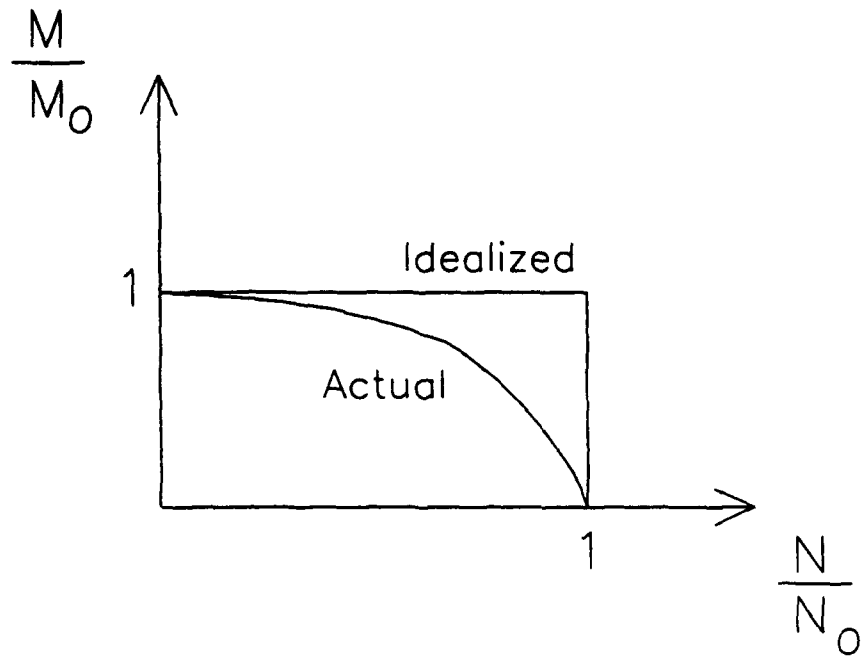


Figure 4.1 Decoupling the Yield Locus - Actual and Idealized (only one quadrant shown). Decoupling of bending and membrane force (upper), and shear force and axial force (lower).

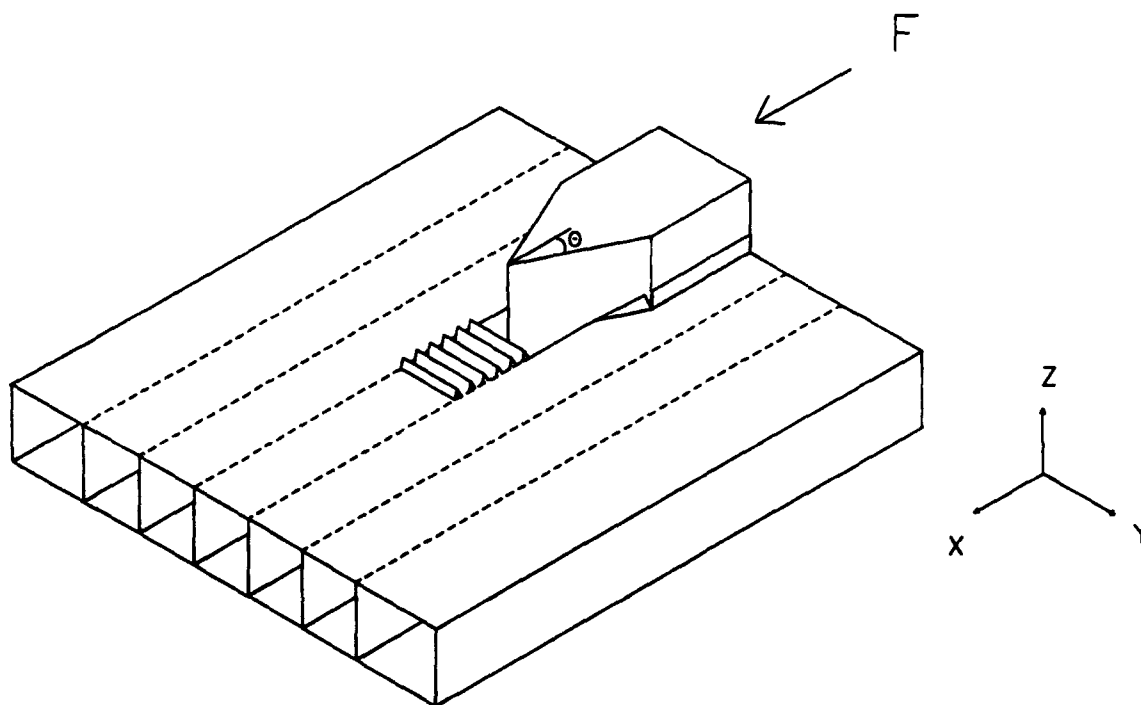


Figure 4.2 USDH Deformation Model.

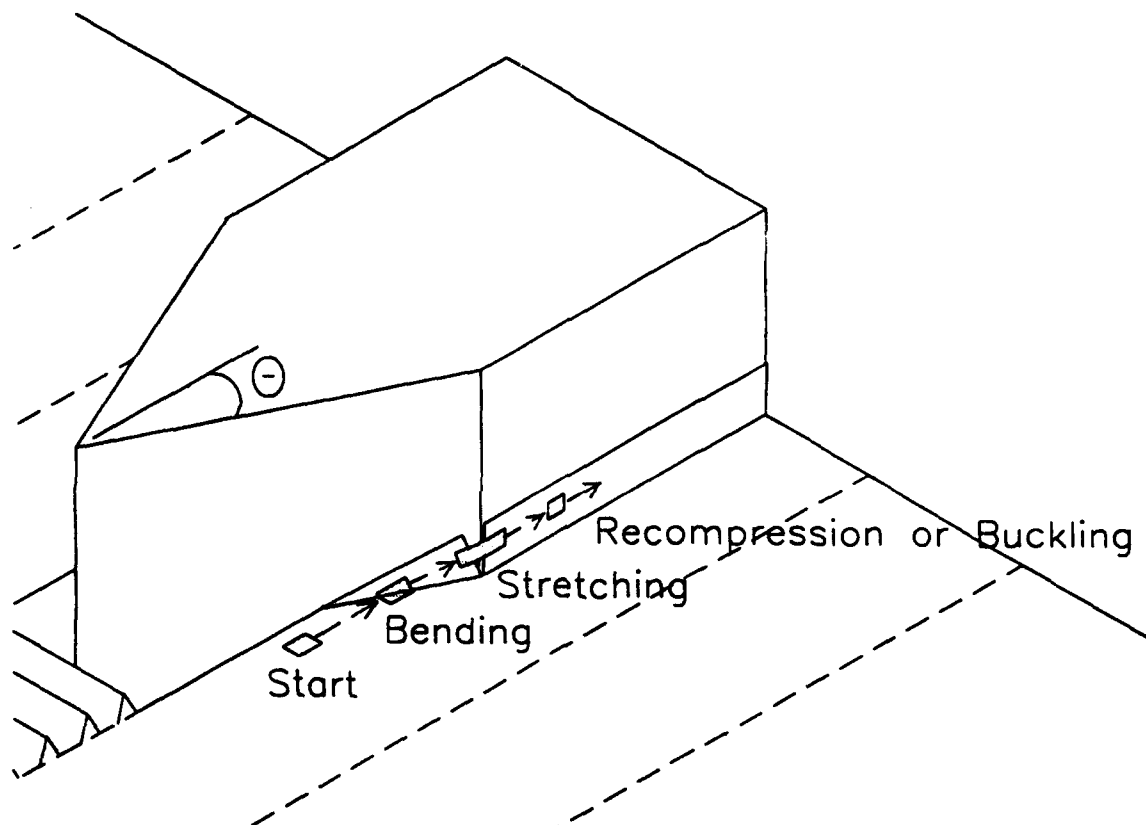


Figure 4.3 Material Element Undergoing Deformation Around Wedge.

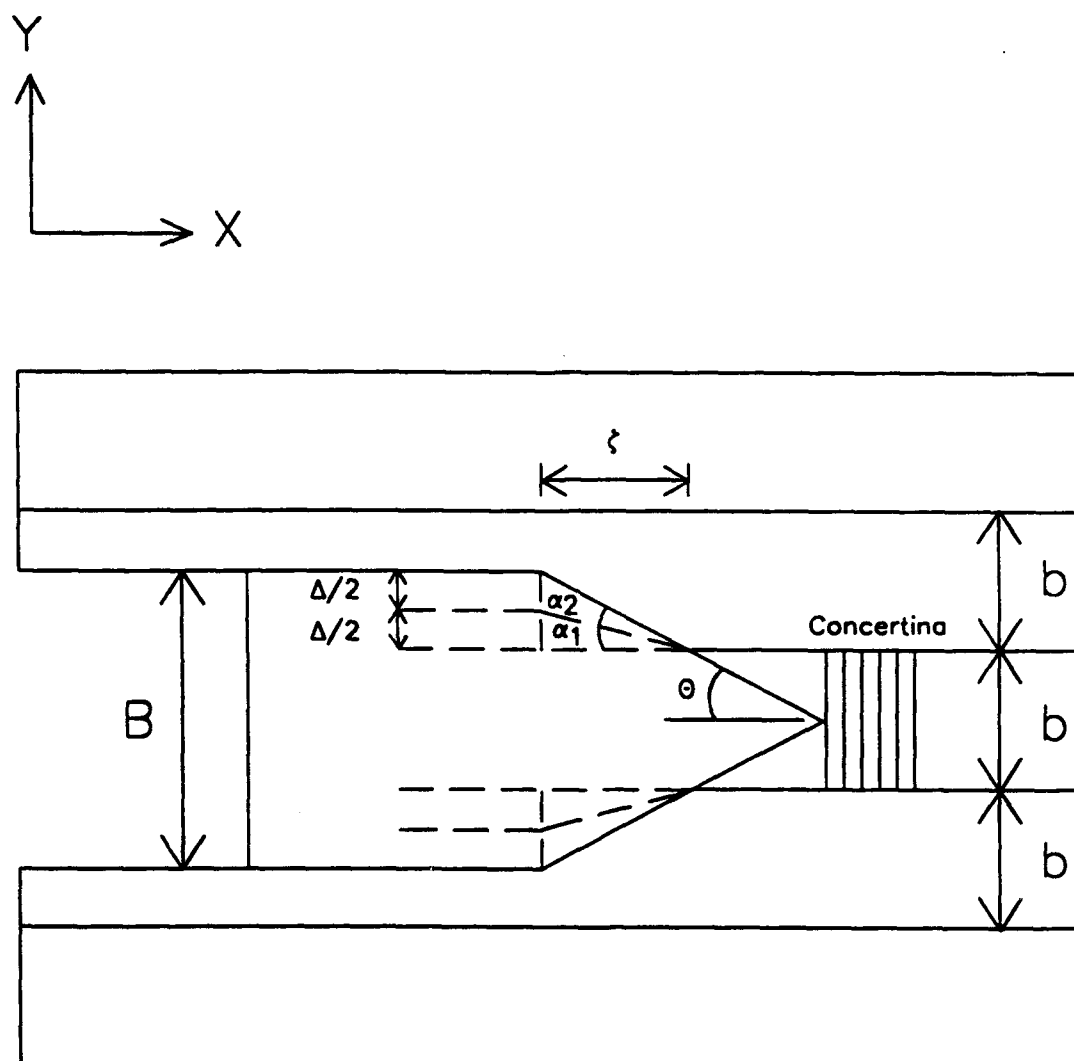


Figure 4.4 Plan View of USDH Wedge Cutting Process.

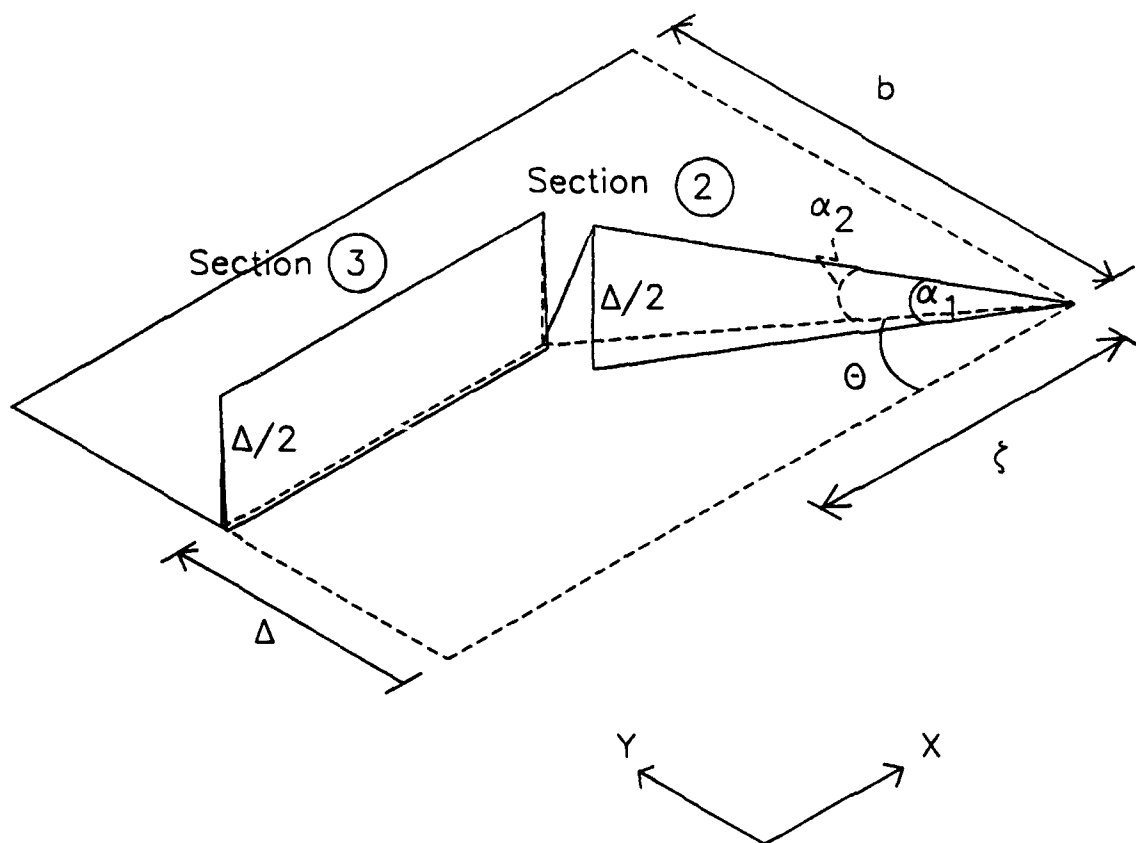


Figure 4.5 Deformation Mechanisms. The photo shows an end view of an actual USDH specimen. One section of the simplified kinematic model is shown (by symmetry).

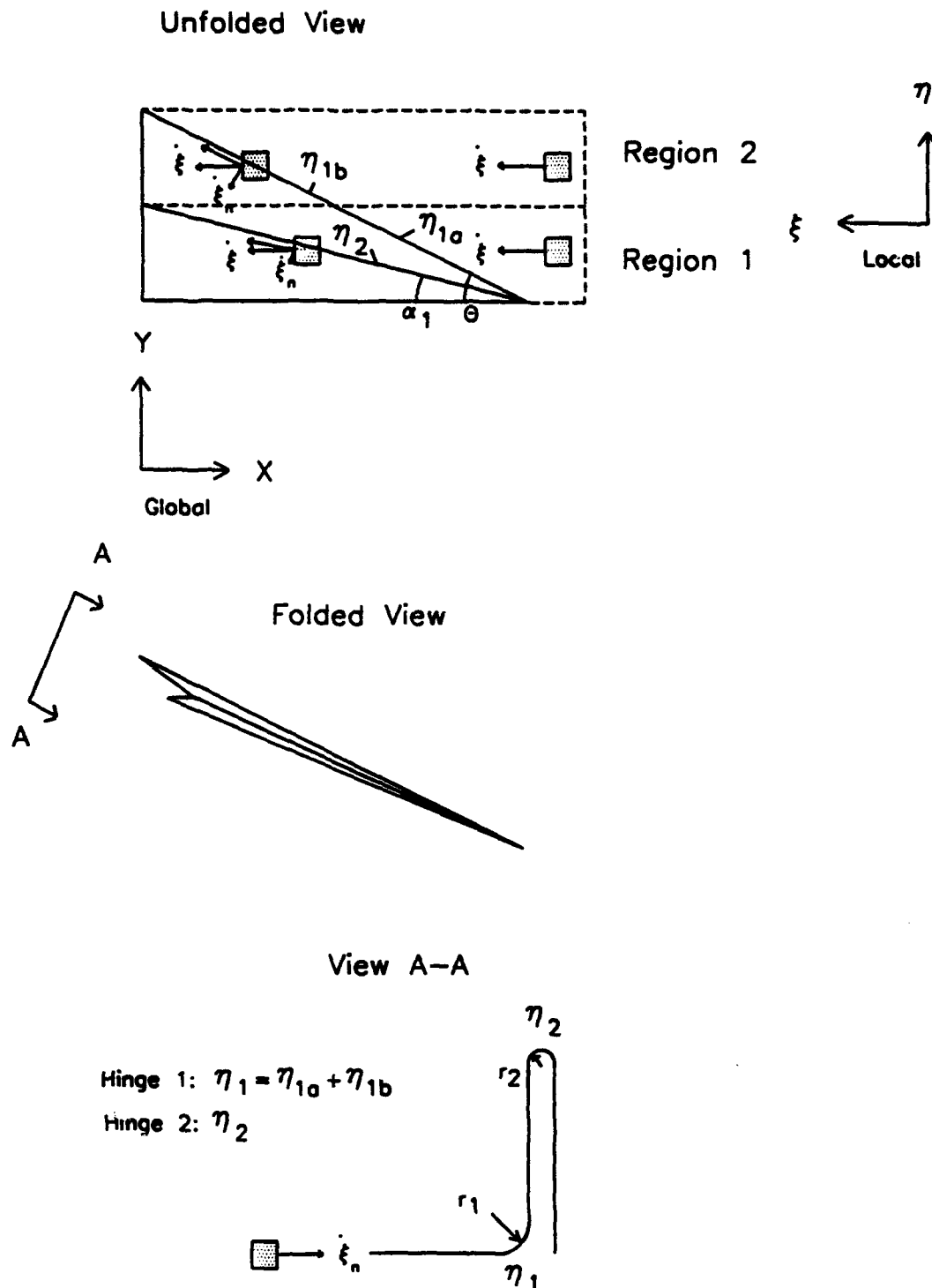


Figure 4.6 Material Element Undergoing Bending.

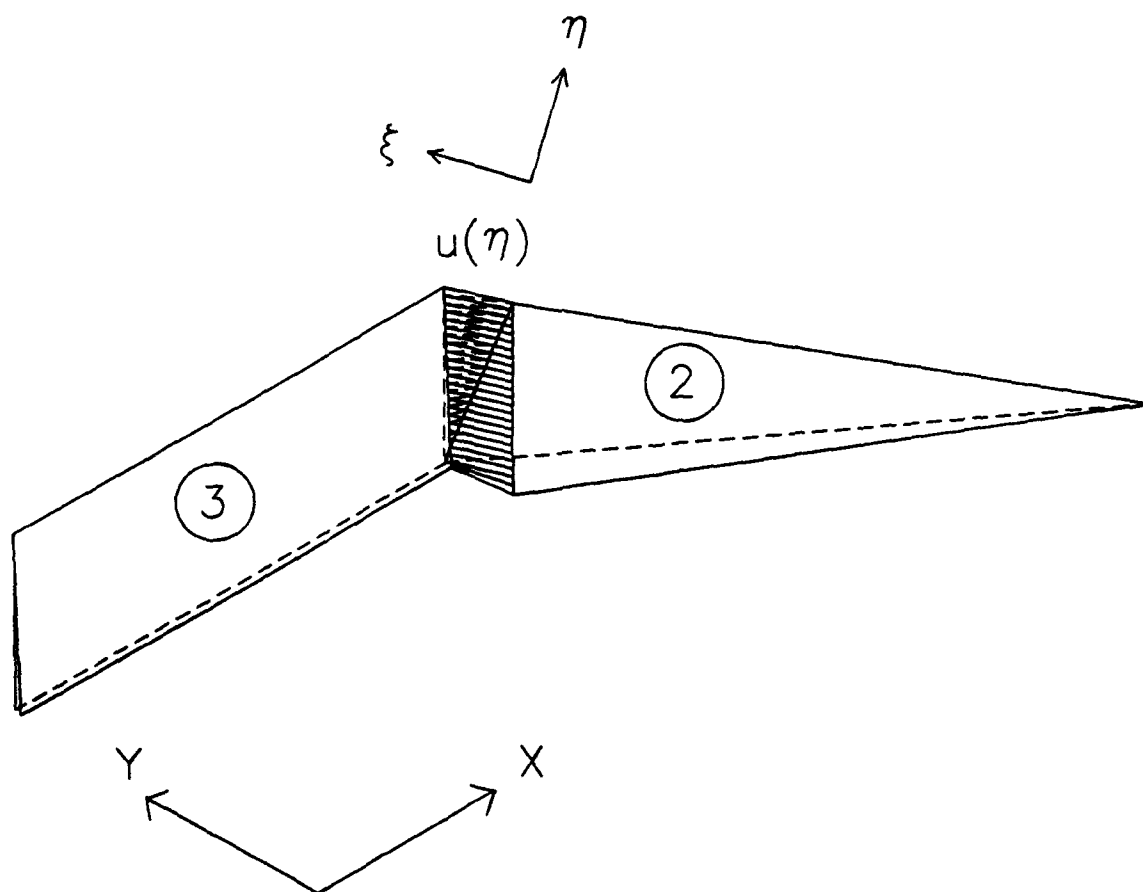


Figure 4.7 Detailed Region of Membrane Stretching.

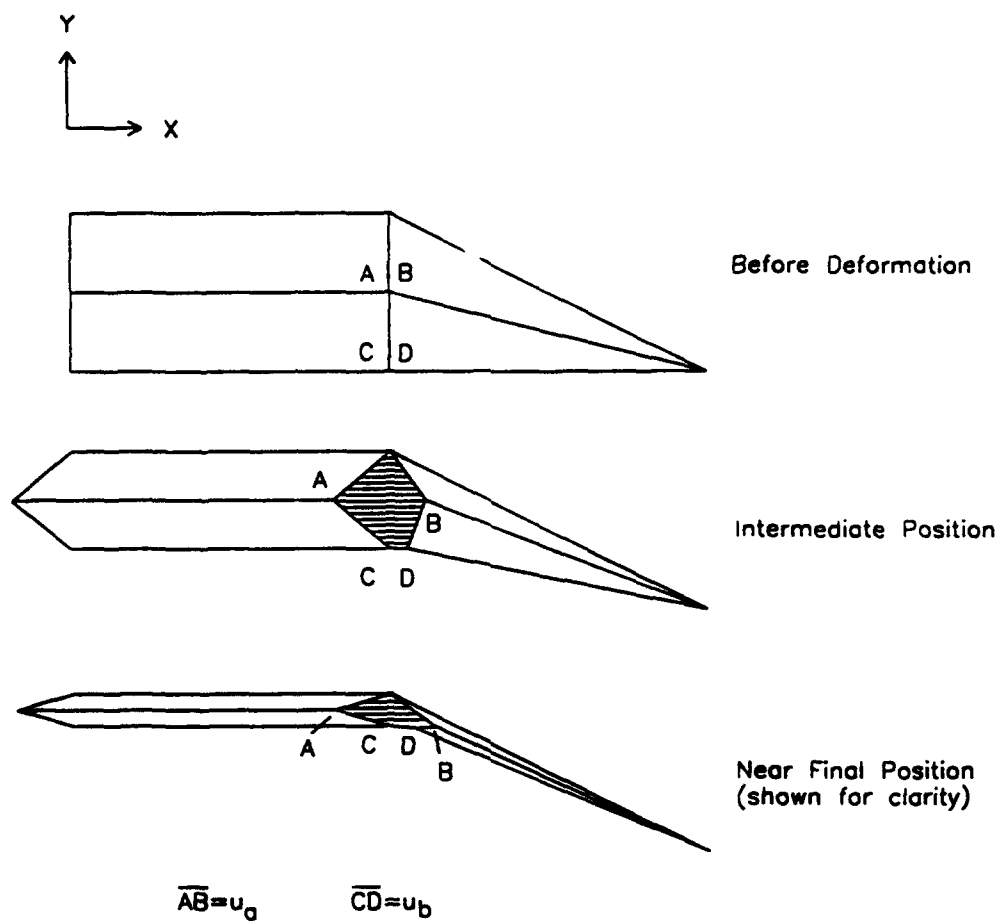


Figure 4.8 Deformation Process for Membrane Stretching.

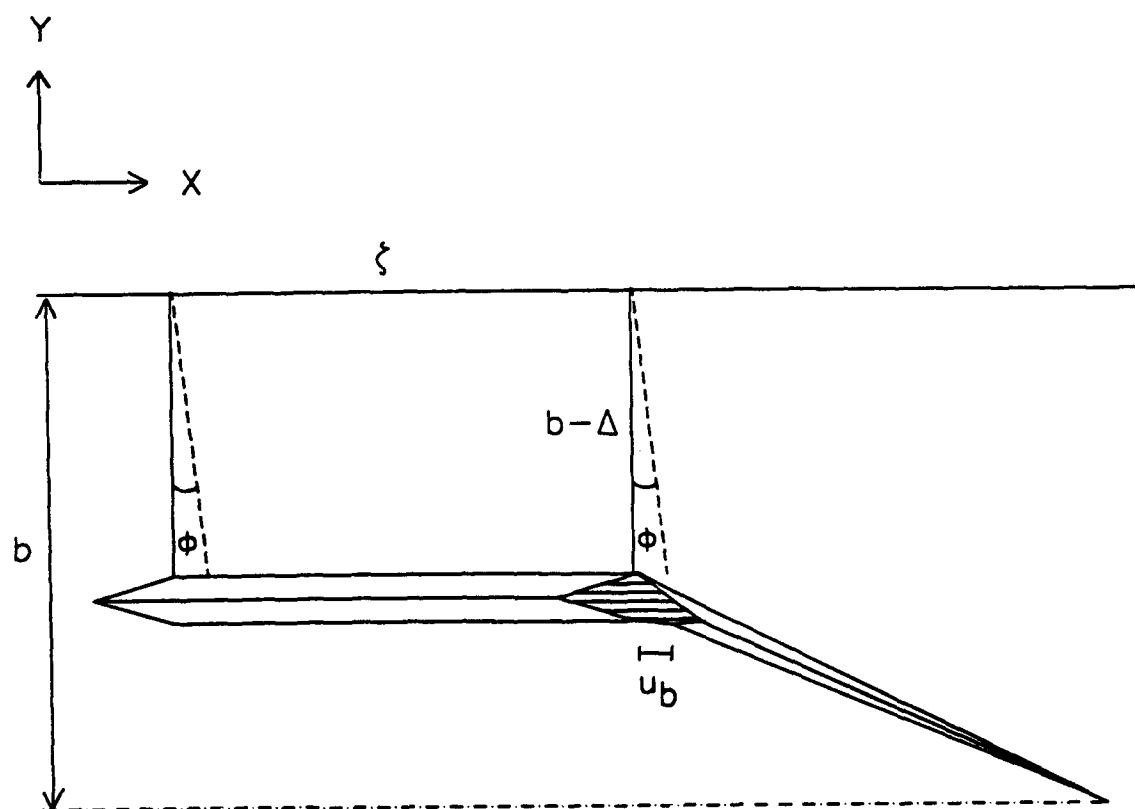


Figure 4.9 Shearing of Plate for Kinematic Admissibility.

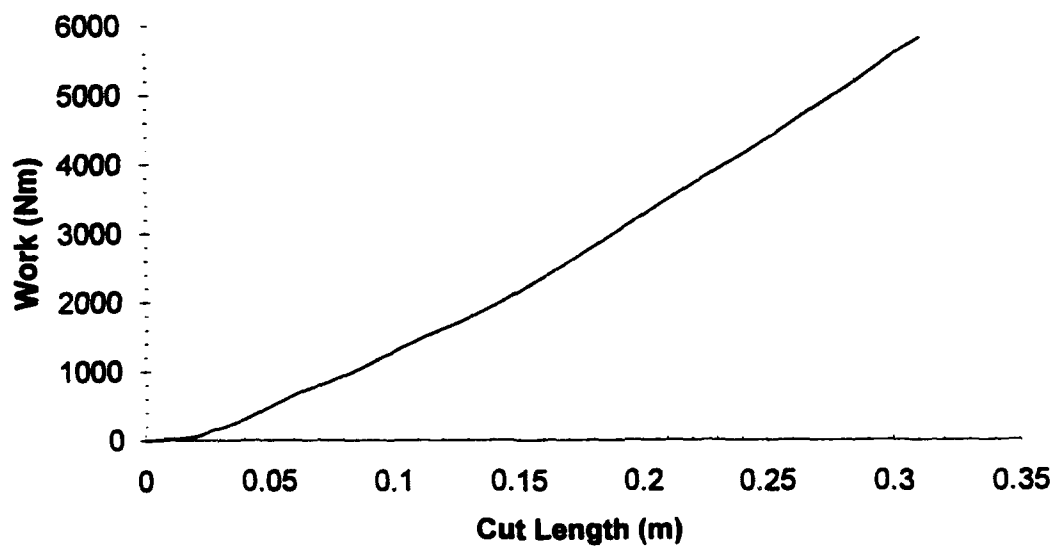
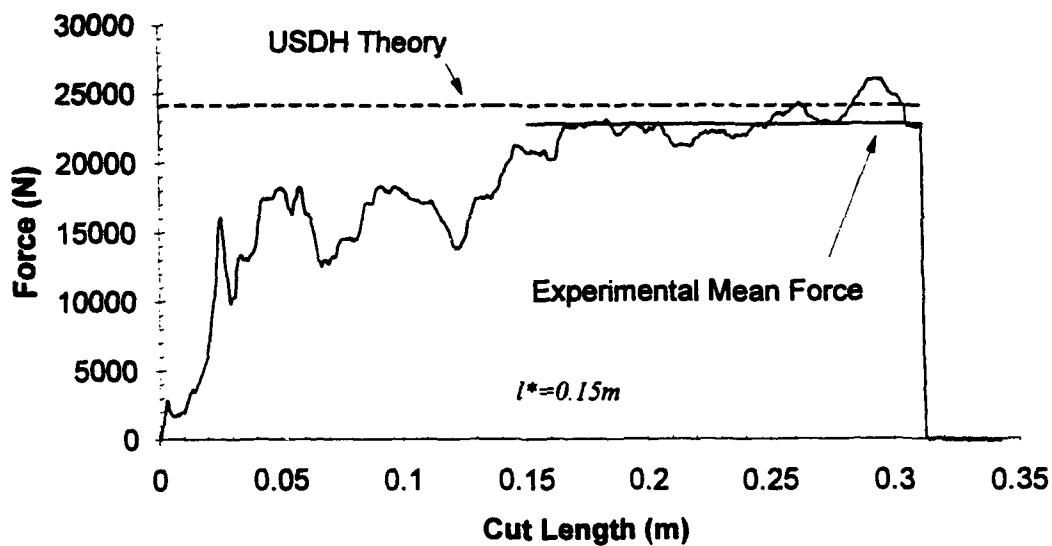


Figure 4.10 Test No. 1 (USDH, Wedge #1, $\theta=45^\circ$, Sharp Tip) - Comparison of Experiment and Theory (Force- and Work-Displacement Graphs).

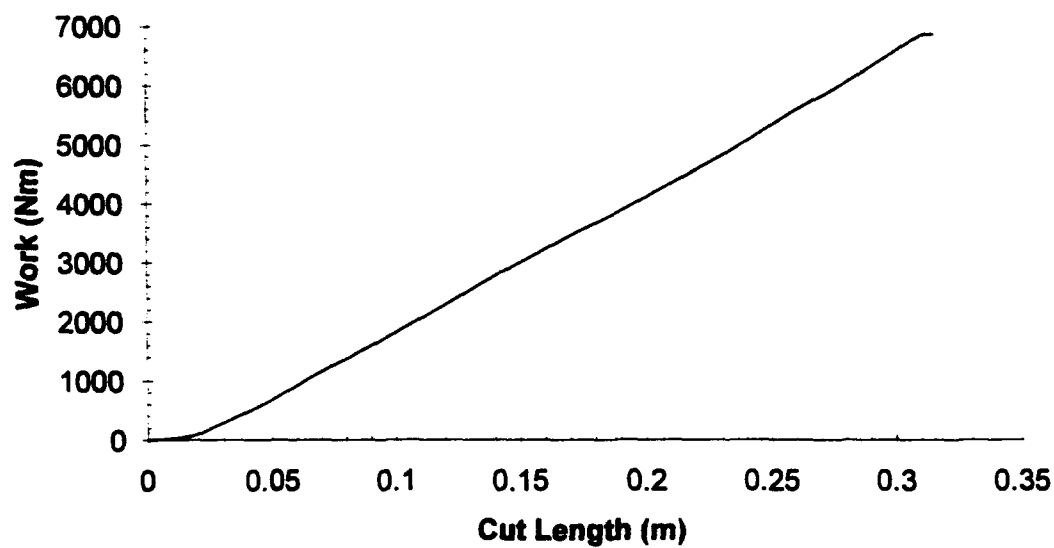
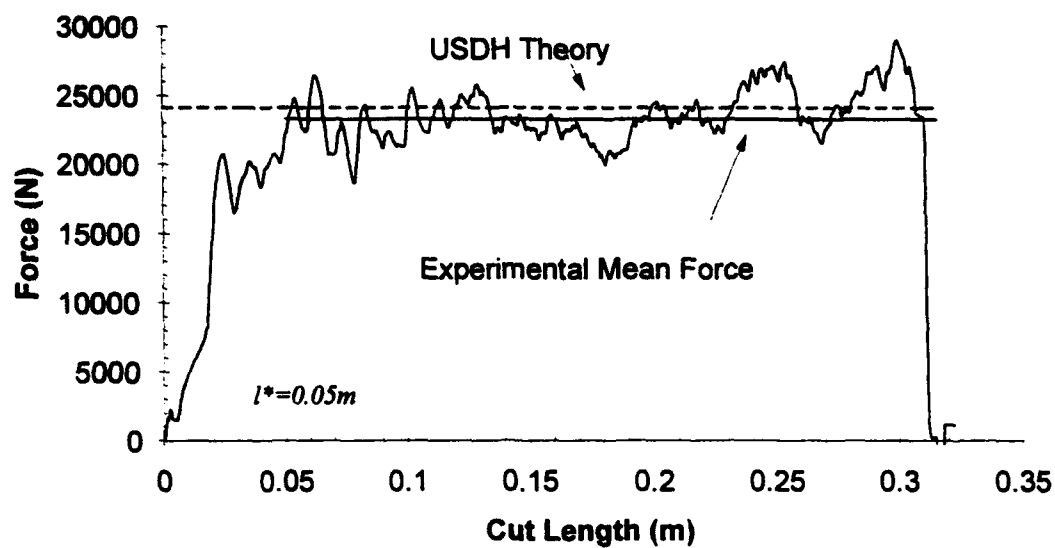


Figure 4.11 Test No. 2 (USDH, Wedge #2, $\theta=45^\circ$, 3/8 in. Radius Tip) - Comparison of Experiment and Theory (Force- and Work-Displacement Graphs).

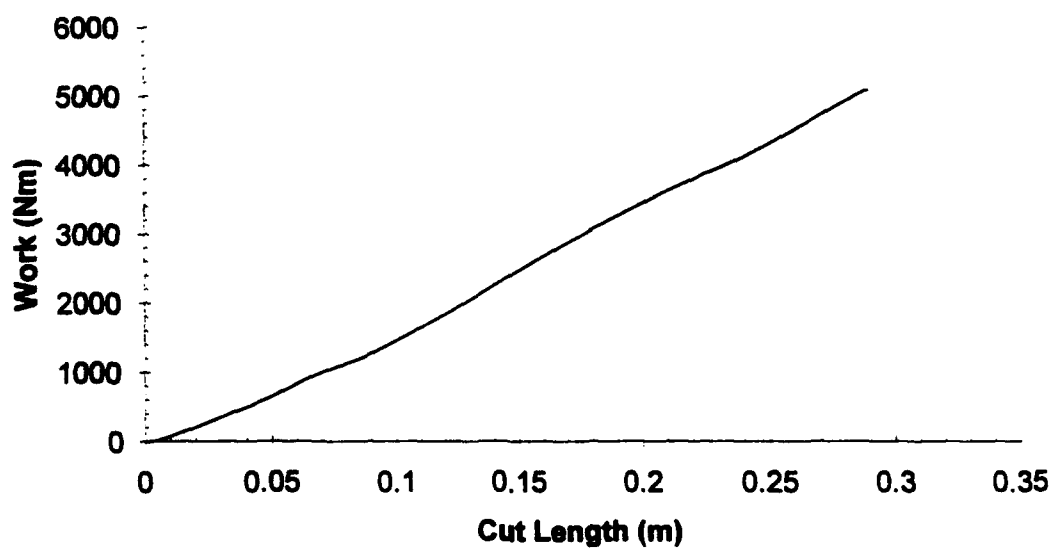
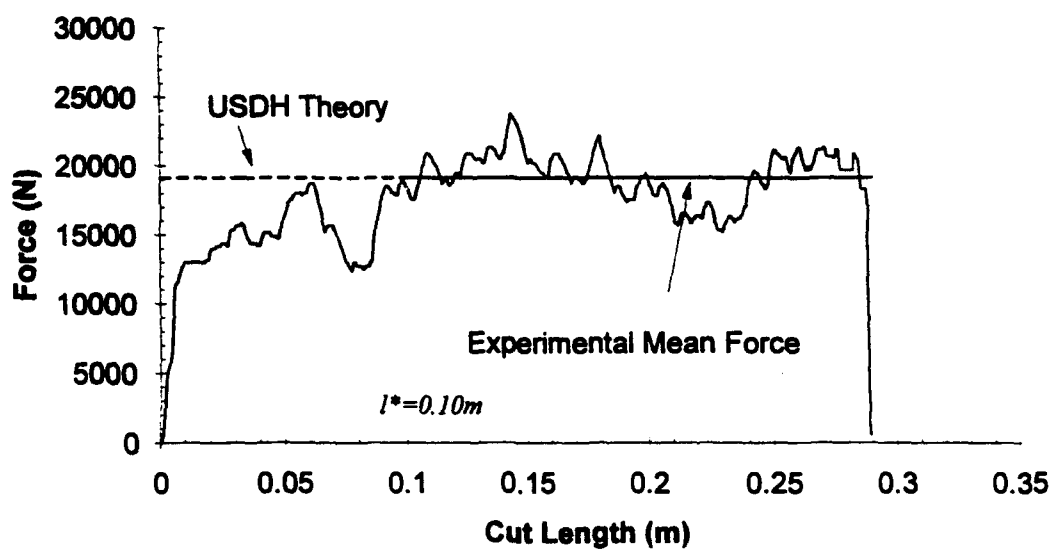


Figure 4.12 Test No. 3 (USDH, Wedge #3, $\theta=30^\circ$, Sharp Tip) - Comparison of Experiment and Theory (Force- and Work-Displacement Graphs).

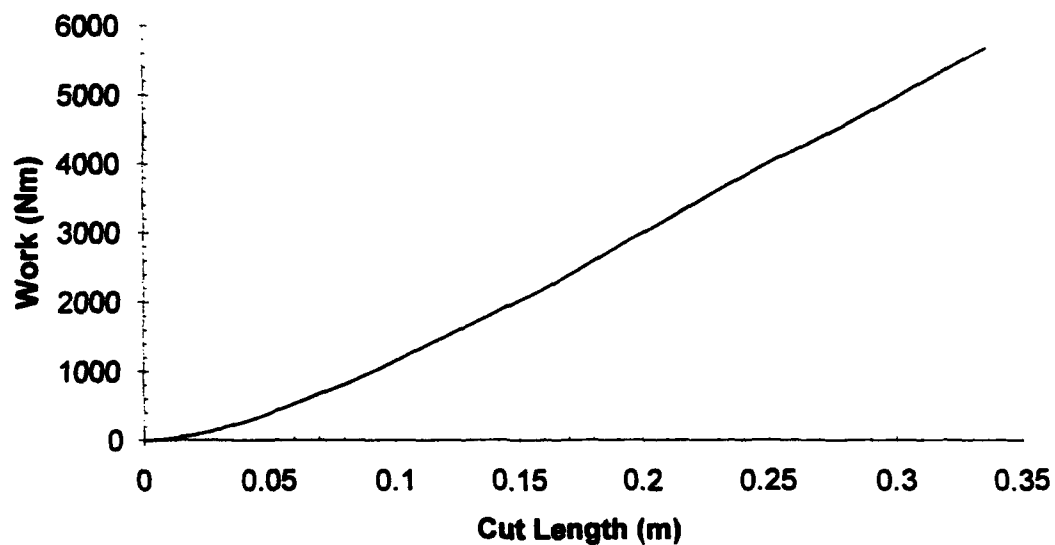
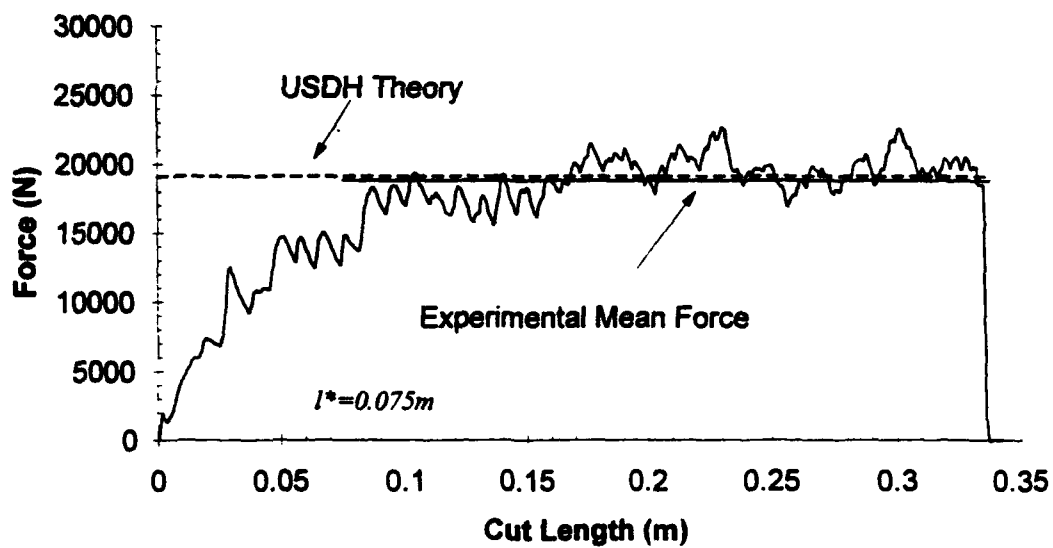


Figure 4.13 Test No. 4 (USDH, Wedge #4, $\theta=30^\circ$, 3/8 in. Radius Tip) - Comparison of Experiment and Theory (Force- and Work-Displacement Graphs).

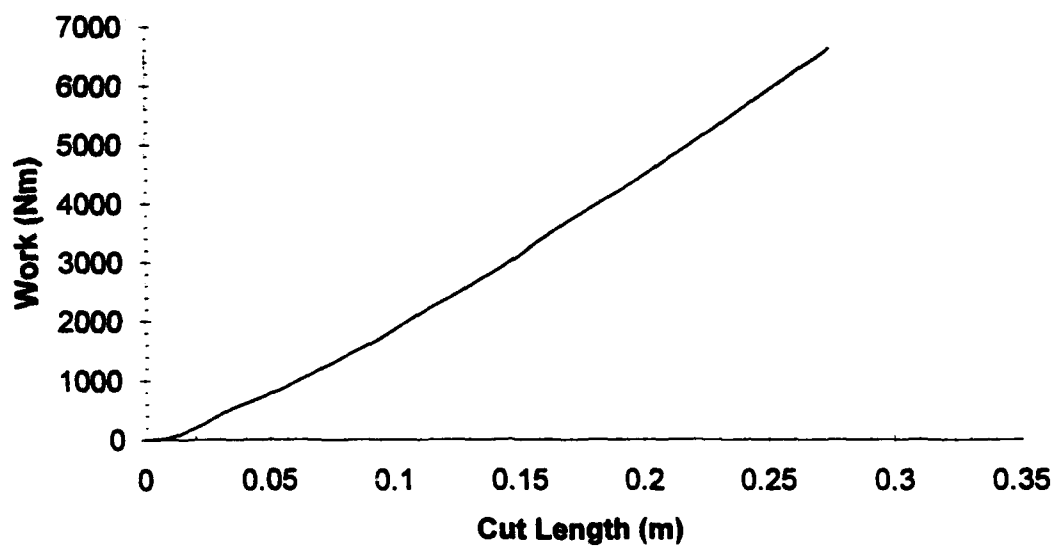
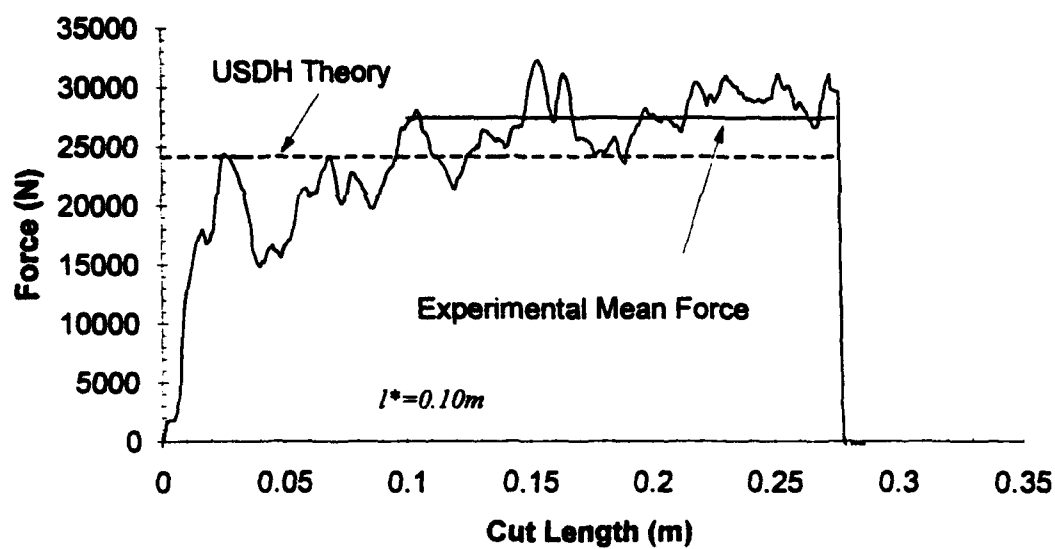


Figure 4.14 Test No. 5 (USDH, Wedge #5, Cylindrical) - Comparison of Experiment and Theory (Force- and Work-Displacement Graphs).

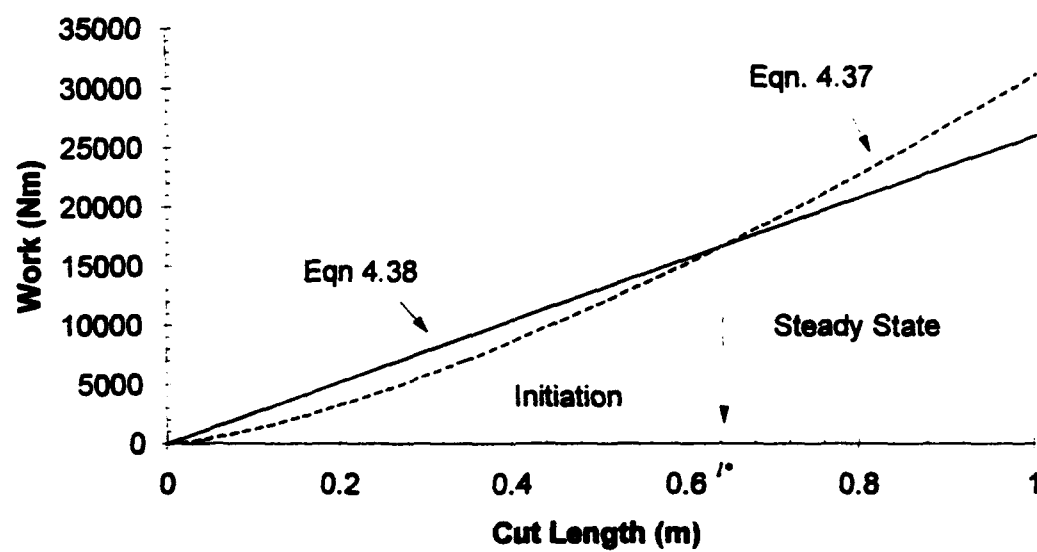


Figure 4.15 Work-Displacement Graph Showing Transition from Initiation to Steady State Cutting.

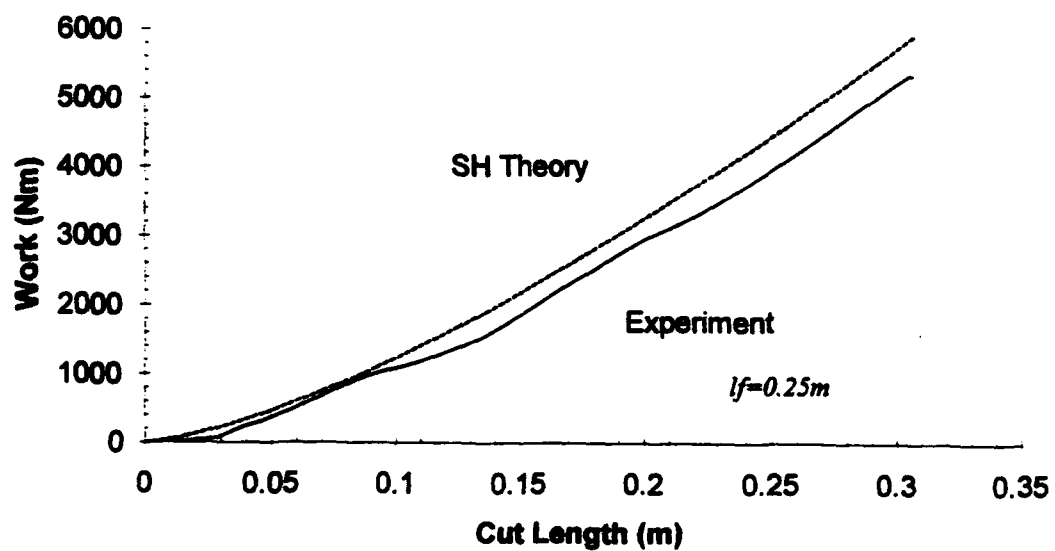
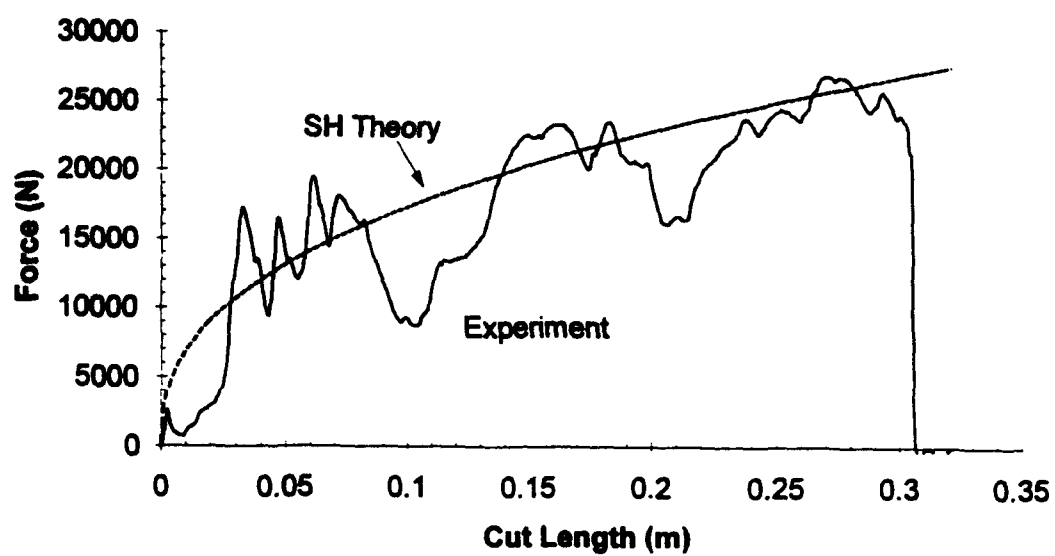


Figure 4.16 Test No. 7 (SH, Wedge #1, $\theta=45^\circ$, Sharp Tip) - Comparison of Experiment and Theory (Force- and Work-Displacement Graphs).

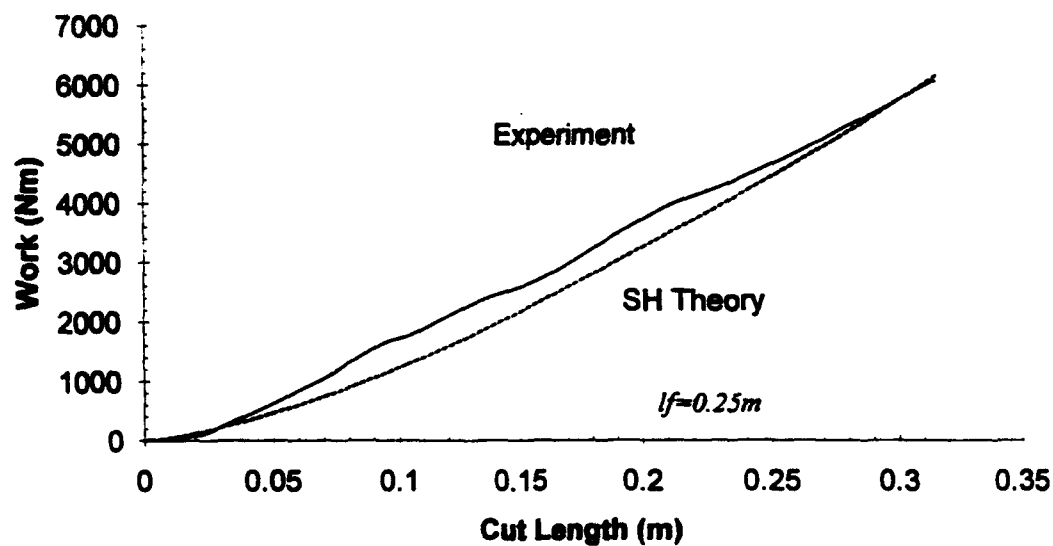
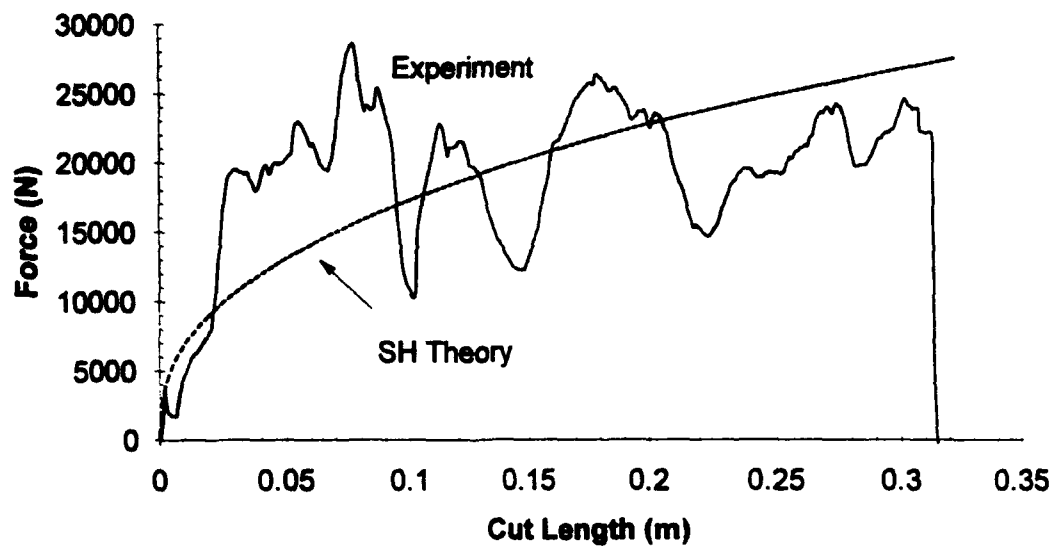


Figure 4.17 Test No. 8 (SH, Wedge #2, $\theta=45^\circ$, 3/8 in. Radius Tip) - Comparison of Experiment and Theory (Force- and Work-Displacement Graphs).

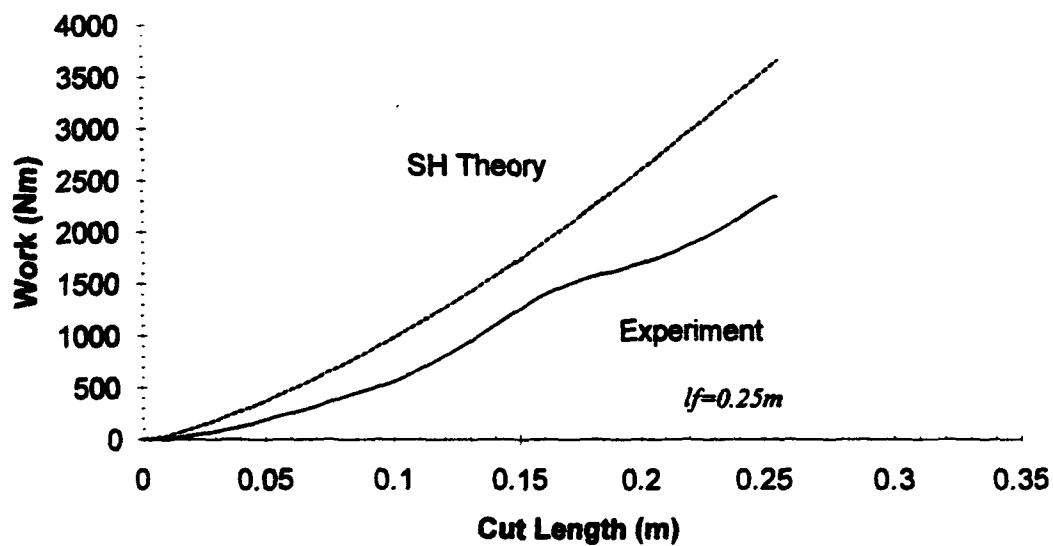
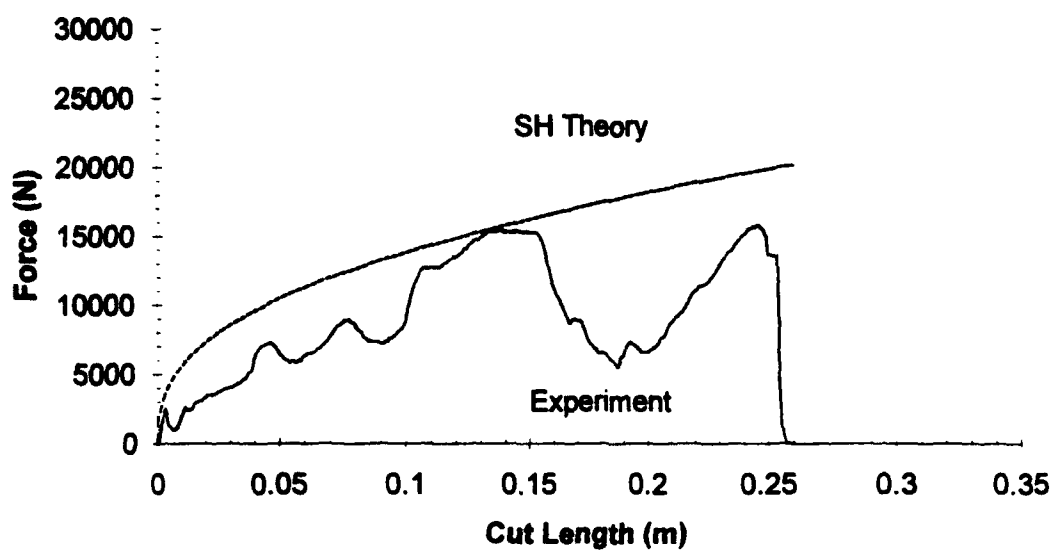


Figure 4.18 Test No. 9b (SH, Wedge #3, $\theta=30^\circ$, Sharp Tip) - Comparison of Experiment and Theory (Force- and Work-Displacement Graphs).

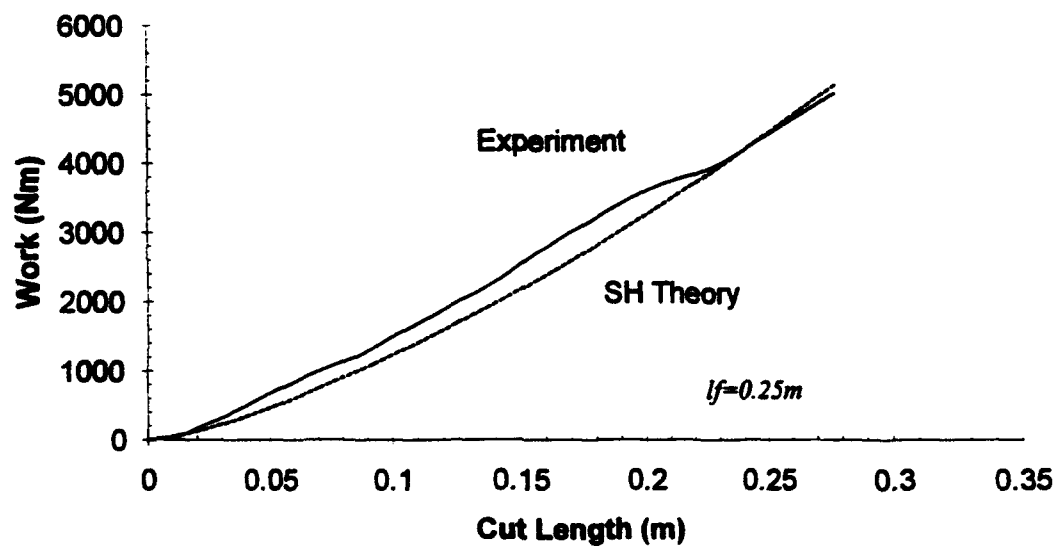
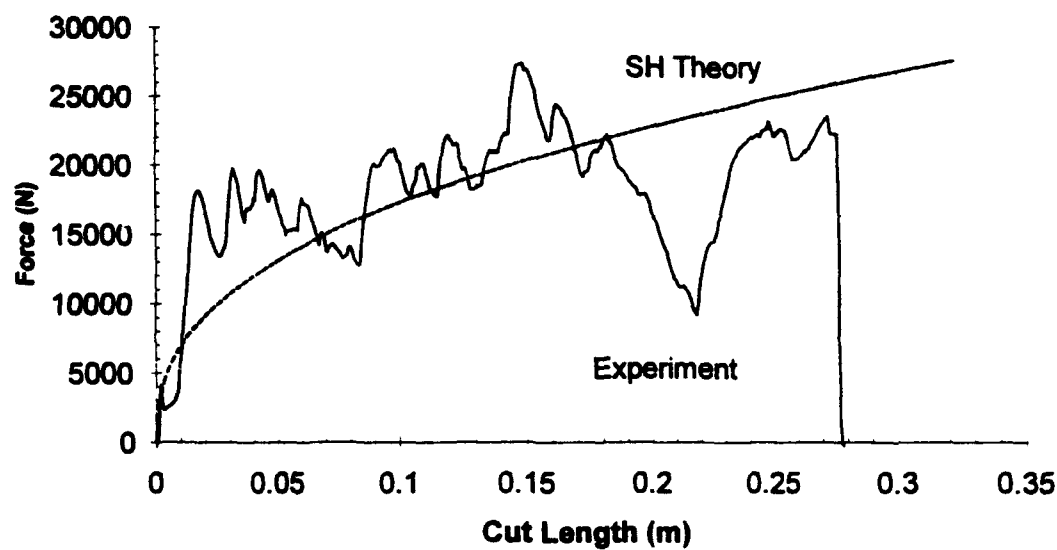


Figure 4.19 Test No. 10 (SH, Wedge #5, Cylindrical) - Comparison of Experiment and Theory (Force- and Work-Displacement Graphs).

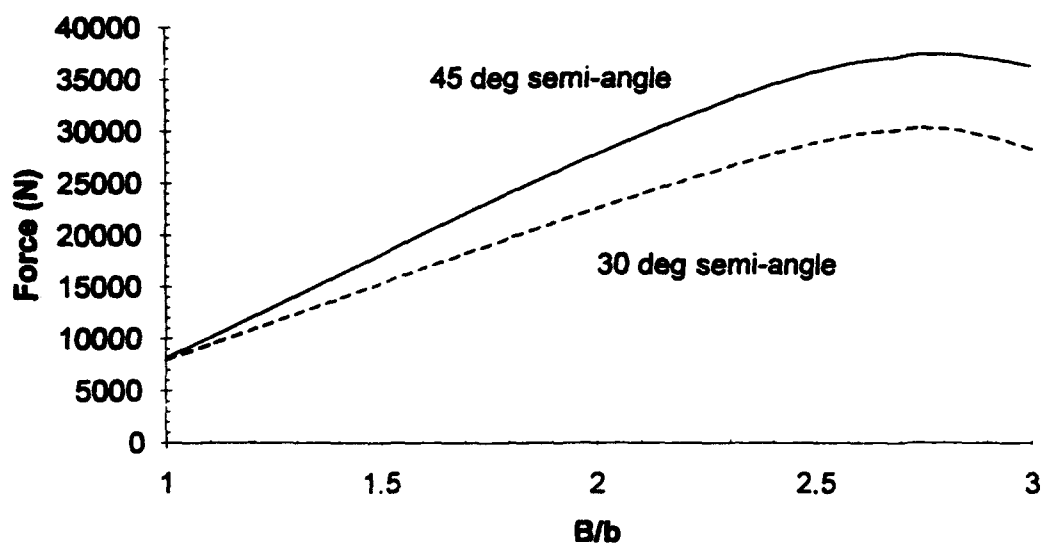


Figure 4.20 Effect of Wedge Width on USDH Cutting Force (Equation 4.41).

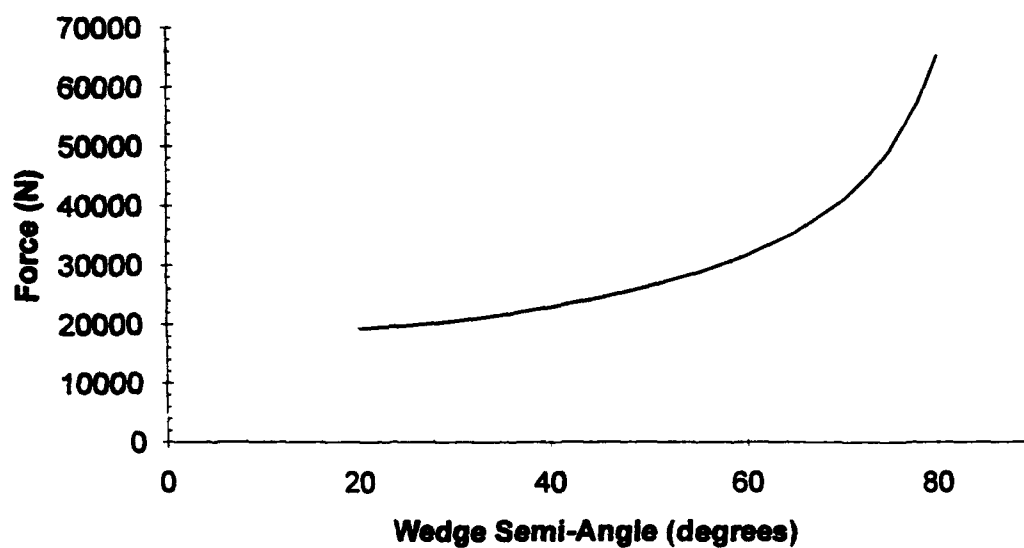


Figure 4.21 Effect of Wedge Semi-angle on USDH Cutting Force (Equation 4.41).

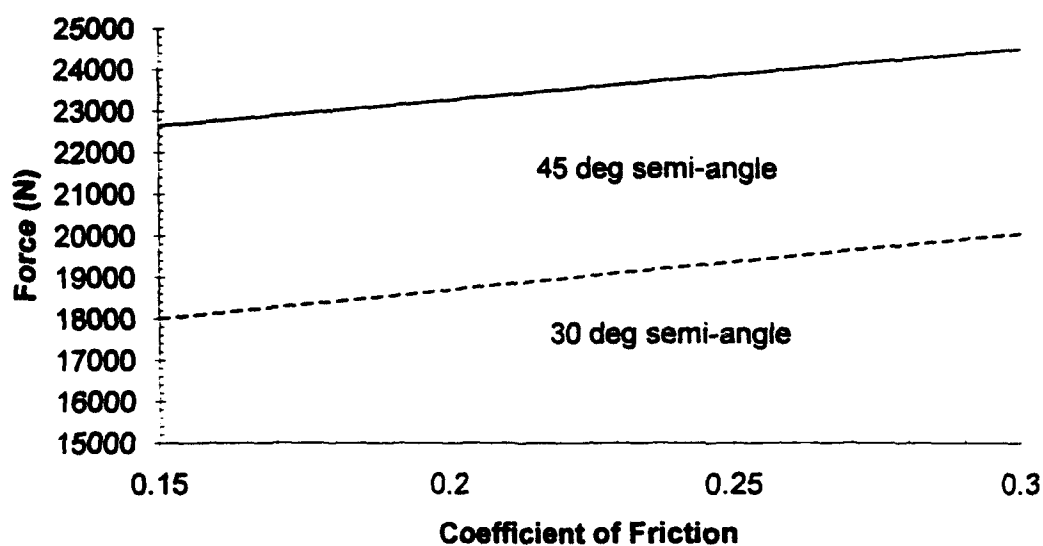


Figure 4.22 Effect of Coefficient of Friction on USDH Cutting Force (Equation 4.41).

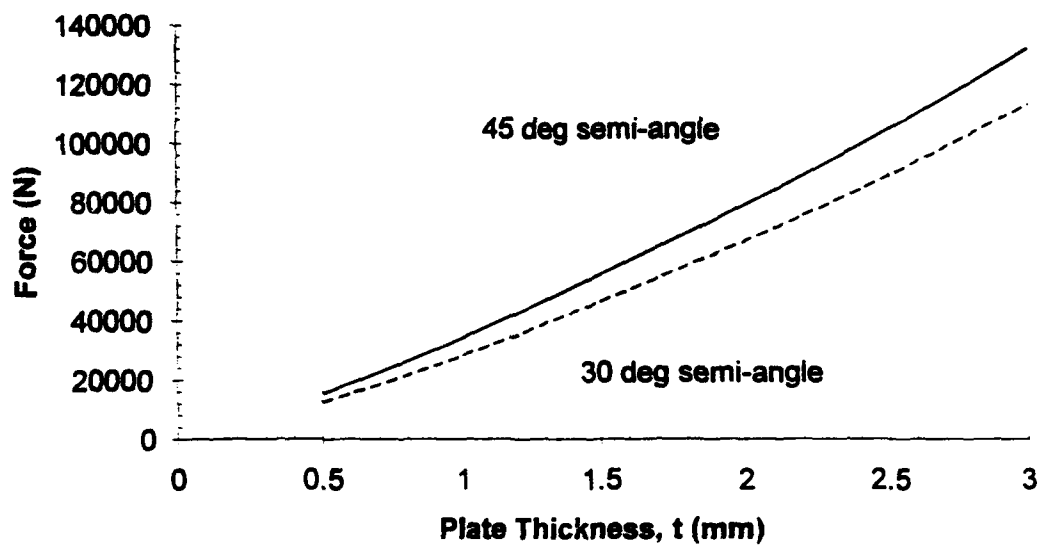


Figure 4.23 Effect of Plate Thickness on USDH Cutting Force (Equation 4.41).

Chapter 5

Conclusions and Recommendations for Future Work

5.1 Conclusions

The work in this thesis contributes to the Joint MIT-Industry Program on Tanker Safety by providing experimental force data for the cutting by a wedge of Unidirectionally Stiffened Double Hull (USDH) and longitudinally stiffened single hull models. *A theoretical steady-state cutting force solution proposed for the USDH model is quite accurate, with an error range of -12% to +6% compared to the experimental mean force. An existing solution for cutting initiation by Thomas and Wierzbicki was applied to the single hull model giving results within -4% to +12% of the experiments when comparing the final work required at the end of the cut length.*

USDH Summary - A theoretical expression for the steady-state cutting force (Equation 4.41) of a kinematic model of the USDH specimen was formulated using an upper bound approach. Steady-state cutting occurred at a transition cut length to wedge-width ratio of approximately $l^*/B = 1.3$. The model assumes a concertina tearing mode of the plate under the wedge tip in the central cell and deformation of the plating in the adjacent cells. Comparison of the theory to the experiments showed correlation in the range of -12% to +5.9%. The absolute average error is 4.6%. The worst case of -12.0% was for a specimen that was cut using a cylindrical wedge. An explanation lies in that an equivalent wedge semi-angle had to be chosen for use in (4.41). Picking a wedge angle of 53° improves the accuracy of the results to within 0.5%. Another factor may be that there

are other tearing modes that require more work when using a cylindrical (i.e. blunt) wedge. This requires further investigation.

A parametric study of the steady state cutting force solution of Equation 4.41 was conducted. The varied parameters were: wedge width, wedge semi-angle, coefficient of sliding friction, and hull plate thickness. The solution responds to these variables as expected (as shown in Figures 4.20 through 4.23). The solution has a weak dependence on the coefficient of friction.

The contributions of the internal work in membrane stretching and shearing, bending, and friction are shown in Table 5.1 (the concertina tearing contribution mode is not included).

Table 5.1 Contribution of Membrane, Bending, and Friction in the USDH Steady-State Cutting Force Solution (not including concertina tearing).

	$\theta=30^\circ$	$\theta=45^\circ$
Membrane	37.3%	55.3%
Bending	28.5%	21.6%
Friction	34.2%	23.1%

Single Hull Summary - The theory developed by Wierzbicki and Thomas (1993) for the cutting of a single plate was employed by smearing the longitudinal stiffeners and plate to obtain an equivalent thickness plate. The work in cutting of the experiments and theory were compared at the final length of cut (0.25m). The correlation between the theory and experiments was within -4.4% to +12.3%. The average absolute error is 5.7%. In one test, the theory overpredicted the work 55%, but this test used a specimen that was

cut in half and did not have the bottom edge fully clamped during the experiment. This experiment should be repeated.

Steady-state cutting was never reached even after a final cut length to wedge-width ratio of approximately $l_f/B = 3$.

Paik (1994) recently conducted stiffened plate cutting experiments and also applied the smearing technique to Wierzbicki and Thomas' equation. The wedge semi-angle was 30° . In Paik's experiments, the length of wedge penetration was shallow (~120 to 160 mm for specimens similar in size to the those used here) and the wedge shoulder barely made contact with the longitudinals. Thus, the longitudinals were barely deformed. Wierzbicki and Thomas' solution underestimated the work (measured at a cut length of 120 mm) of Paik's experiments by -32.1% for $t_{eq}=10.5$ mm ($t_p=7.0$ mm), and -19.5% for $t_{eq}=4.7$ mm ($t_p=3.4$ mm). The equivalent thickness for the specimens in this thesis was $t_{eq}=2.01$ mm. It appears that the error grows as the equivalent thickness increases.

5.2 Recommendations for Future Work

Future study is needed in the following areas:

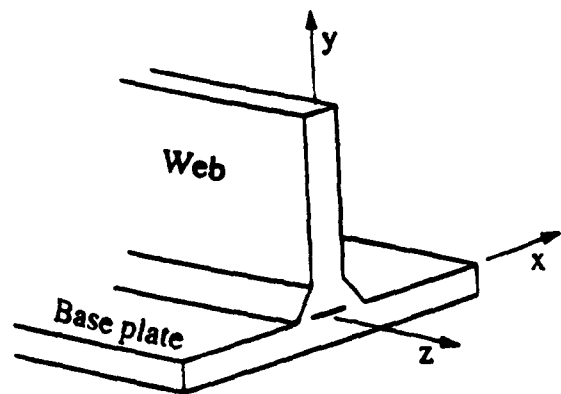
- **Experimental** - The experiments in this thesis were all conducted with the specimen at a zero degree angle of attack from the vertical. This was due to the limitations of the existing test fixture and universal test machine. To cut the specimens at an angle of attack, redesign of the fixture and wedge-to-load cell adapter is required to allow a long cutting stroke while ensuring no excessive bending moments are placed on the load cell. Also to be considered in the design is an increased length of cut so that steady state cutting would be observed in all future experiments.

For the single hull tests, hindsight shows that at least one more test needs to be run using a 30° wedge. The poor correlation of Test 9 with the theory is due to a poor experiment, not necessarily that the theory does not hold. This needs to be verified.

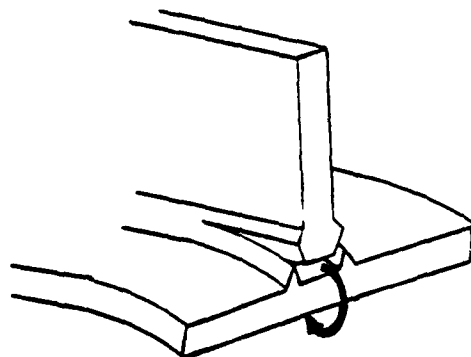
- Welding - All of the tests exhibited no failure of the electron beam welds (EBW). It is unrealistic to expect that some of the welds would not fail in actual ship. This has, in fact, been observed in grounding accidents. McClintock (1994) has identified the deformation and fracture modes of T-joints as shown in Figure 5.1. Kirkov (1994) has investigated the tearing mode of weld failure. More research needs to be conducted in the area of full scale weld failure. Appendix D shows the results of "Lazy-T" bending tests of small scale EBW T-specimens. This idea could be used as the starting point for full scale weld testing.
- Theory - The USDH steady state cutting force solution of Equation 4.41 needs further investigation both analytically and using experiments. The formulation needs to be expanded to include the case where the width of the wedge exceeds the current spacing limitation of $3b$, and the case of cutting at an angle of attack. Experiments could be run to verify the solution's behavior for cases such as: increased plate thickness, different plate thicknesses of the inner and outer hulls, larger wedge semi-angles (e.g. $\theta > 45^\circ$), cutting of only one plate in the USDH model, cutting the specimens at an angle of attack, etc. The pros to running more experiments would be to provide further validation of theory and model the grounding phenomenon more realistically. The cons lie in that the test specimens are relatively expensive to fabricate (around \$500 each), and that significant effort and expense would be

required to build new test fixtures and equipment. The cost-benefit would have to be analyzed to make this decision.

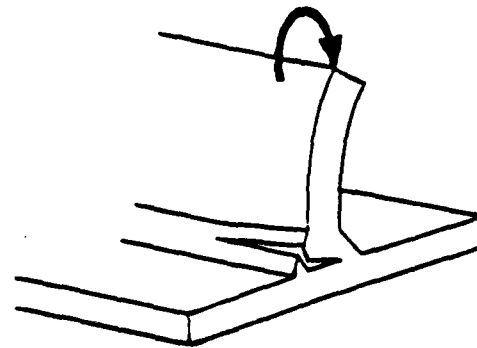
- **Scaling** - The proposed USDH steady-state force cutting solution and Wierzbicki and Thomas' plate cutting initiation solution produce scaling laws. Geometric parameters such as plate thickness t , and longitudinal spacing b , are in fact nonlinear in Equations 4.41 and 1.8. The result is consistent with Atkin's (1988) assertion that simple geometric scaling (i.e. λ^3 -scaling) of work does not hold. Future work in comparison of small scale tests and laws must be made to large scale tests. The issue of scaling must be thoroughly explored not only for the results of this thesis, but for all the theoretical formulations supporting the MIT-Industry Program on Tanker Safety. Efforts should be made to obtain experimental results on the cutting of large scale USDH models when they are conducted (in the future) by NSWG for comparison to small scale experimental results and theory proposed here.



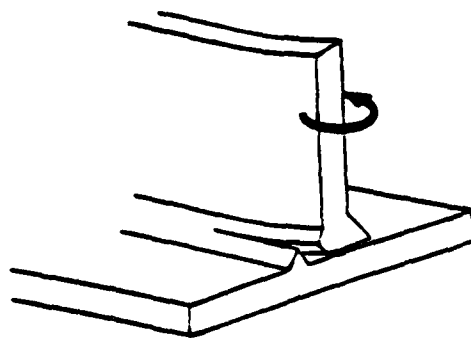
Coordinate axes for a T-joint



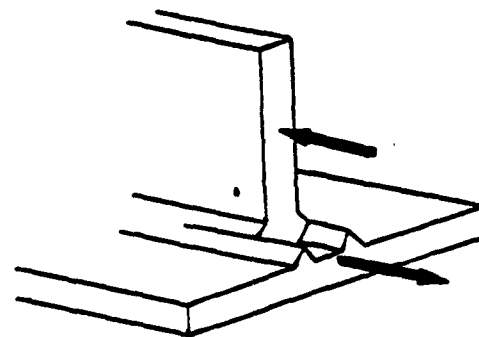
(a) Tearing



(b) Web folding



(c) Web bending



(d) Longitudinal shearing

Figure 5.1 Deformation and Fracture Modes of T-Joints.
(McClintock (1994).)

References

- Atkins, A. G., 1988, "Scaling in Combined Plastic Flow and Fracture", *International Journal of Mechanical Sciences*, Vol. 30, No. 3/4, pp. 173-191.
- Beach J., 1991, "Advanced Surface Ship Hull Technology - Cluster B", *ASNE Naval Engineers Journal*, Vol. 103, No. 6, November, pp. 27-37.
- Becket, F. J., 1991, "Electron Beam Welding Transmission Components", *Welding & Metal Fabrication*, December, pp. 551-554.
- Fernandez-Gonzalez, F., 1993, Private Communications, September.
- Hughes, C. F., 1988, *Ship Structural Design: A Rationally Based, Computer-Aided, Optimization Approach*, SNAME.
- Johnson, W., and Mellor, P. B., 1983, *Engineering Plasticity*, Ellis Horwood Limited, pp. 183-198.
- Jones, N., 1983, "Structural Aspects of Ship Collisions", *Structural Crashworthiness*, N. Jones and T. Wierzbicki, Editors, Butterworths, London, pp. 316-317.
- Jones, N., and Jouri, W. S., 1987, "A Study of Plate Tearing for Ship Collision and Grounding Damage", *Journal of Ship Research*, Vol. 31, No. 4, pp. 253-268.
- Kirkov, K. D., 1994, "Tests for Tensile Tearing Resistance of Welded T-Joints", *M.S. Thesis, Dept. of Ocean Eng., MIT*, to be submitted May.
- Lu, G., and Calladine, C. R., 1990, "On the Cutting of a Plate by a Wedge", *International Journal of Mechanical Science*, Vol. 32, No. 4, pp. 293-313.
- Maxwell, L.M., 1993, "Effect of Rock Geometry on the Failure Mode of Plates and the Forces in Grounding Experiments", *M.S. Thesis, Dept. of Ocean Eng., MIT*, June.
- McClintock, F. A., and Argon, A. A., 1966, *Mechanical Behavior of Materials*, Addison-Wesley Publishing Company, Inc., Reprinted 1993 by Tech Books, Fairfield, VA.
- McClintock, F. A., 1994, "Fully Plastic Mechanics for Welded T-Joints", *Joint MIT-Industry Program on Tanker Safety*, Report No. 26, January.

Minorsky, V. U., 1959, "An Analysis of Ship Collisions with Reference to Protection of Nuclear Power Plants", *Journal of Ship Research*, Vol. 3, No. 1.

Nurick, G., 1993, Private Communications, September.

Oil Pollution Act of 1990, Public Law 101-380, August 18, 1990.

Okamoto T., *et al.*, 1985, "Strength Evaluation of Novel Unidirectional-Girder-System Product Oil Carrier by Reliability Analysis", *SNAME Transactions*, Vol. 93, pp. 55-77.

Paik, J. K., 1994, "Cutting of a Longitudinally Stiffened Plate by a Wedge", *Journal of Ship Research*, Submitted March.

Thomas, P.F., 1992, "The Mechanics of Plate Cutting with Application to Ship Grounding", *M.S. Thesis, Dept. of Ocean Eng., MIT*, May.

Thunes, R., 1993, "Development of Analytical Models of Wedge Indentation into Unidirectionally and Orthogonally Stiffened Double Hull Models", *Siv. Ing. Thesis, Department of Marine Structures, Norwegian Institute of Technology*, December.

United States Coast Guard, Department of Transportation, 1992, "Alternatives to Double Hull Tank Vessel Design", *Report to Congress Oil Pollution Act of 1990*.

Vaughan, H., 1978, "Bending and Tearing of Plate with Application to Ship-bottom Damage", *The Naval Architect*, Vol. 97, May, pp. 97-99.

Vaughan, H., 1980, "The Tearing Strength of Mild Steel Plate", *Journal of Ship Research*, Vol. 24, No. 2, pp. 96-100.

Wierzbicki, T., Peer, D. B., and Rady, E., 1993, "The Anatomy of Tanker Grounding", *Marine Technology*, Vol. 30, No. 2, pp. 71-78.

Wierzbicki, T., and Thomas, P., 1993, "Closed-Form Solution for Wedge Cutting Force Through Thin Metal Sheets", *International Journal of Mechanical Science*, Vol. 35, No. 3/4, pp. 209-229.

Wierzbicki, T., 1994, "Concertina Tearing of Metal Plates Improved Solution and Comparison with Experiments", *Joint MIT-Industry Program on Tanker Safety*, Report No. 22, January.

Zheng, Z., and Wierzbicki, T., 1993 "Study on the Steady-State Wedge Cutting Force Through Thin Metal Plates", Massachusetts Institute of Technology, Department of Ocean Engineering, Draft Report, October.

Wierzbicki, T., and Zheng, Z., 1994, "A Theoretical Analysis of a Steady-State Wedge Cutting Through Thin Metal Plates", *Joint MIT-Industry Program on Tanker Safety*, Report No. 19, January.

Appendix A

Operation of the Test Equipment

This appendix discusses the steps required to conduct a plate cutting experiment. It includes the switch lineup of the testing machine and data acquisition program, initialization of the equipment, and processing of the raw data. The procedure assumes that the test specimen and frame assembly has been secured in the test machine, and that the appropriate wedge has been attached to the load cell.

A.1 Instron Universal Test Machine Switch Lineup

The test machine has a number of switches, located on the front, that must be aligned prior to running a cutting experiment. Power on the Instron by flipping two switches located at the lower left front panel. The switches are labeled AMPLIDYNE and MAIN POWER. This should be done first as the machine requires a 30 minute warm up time. The remaining switch settings are shown in Table A1. Start the switch line up at the top left side of the machine and move across and down, then move to the right side of the machine and move across and down.

Table A.1 Instron Universal Test Machine Switch Settings.

Switch Marker	Setting
FULL SCALE LOAD	select desired load value just above expected full load
MARKER CONTROL	manual
PRESET CYCLE COUNTER	off
LOAD CELL	CT-G
PACING CONTROL	normal

ZERO SUPPRESSION CONTROL	out
CHART DRIVE AMPLIFIER	off
STRAIN GAGE PRE-AMPLIFIER	10
RANGE	
LIMIT CYCLE	off
AUTOMATIC	off
CYCLE CONTROL	manual
CYCLE - LO	stop
CYCLE - HI	stop
SPEED CONTROL	-1-.01
TRAVERSE	1

A.2 Data Acquisition Program Lineup

The data acquisition system consists of a 386 IBM compatible personal computer (PC), running a National Instruments Data Acquisition (NI-DAQ version 4.2) software package. The voltage output from the load cell is connected to a volt meter in series with the computer. The program displays a control panel on the screen that consists of switches, toggles and graphical output. The settings can be changed by using the mouse to reposition switches, much like a Windows™ application.

After turning on the computer, the program is accessed by selecting the dos_data_aq icon from the NI-DAQ window. The first screen that appears should have BOARD: NUMBER 1 and BOARD USED: LAB-PC selected. From the toolbar select INSTRUMENTS, and from the menu select STRIP CHART AND DATA LOGGER. This will bring up the control panel screen.

It is from the control panel screen that most of the settings are selected. The output voltages from the load cell can be seen real time on the screen. Set the limits of the y-axis by changing the values of YMAX and YMIN and clicking OK. Suggested values are 0.1 and -0.5 for expected forces of 5k-10k N. The limits settings in no way affect the

actual data being recorded in the computer. On the right side of the screen, set the toggle switch to CONSECUTIVE. Click on SAVE TO FILE. Ensure that the circle changes to green (if it does not show green, then no data will be saved). Click on CHAN SETUP. Another window will be displayed. Select the block showing CHANNEL 0, and type LOAD CELL. Click OK. The previous control panel will then be displayed. Change the value of SAMPLE RATE to 40, and the value of AVERAGE to 40. Click the box next to the word AVERAGE.

A.3 Equipment Initialization

The system must be initialized each time after powering up the machine or if a different wedge is installed. The initialization consists of calibrating the Instron chart recorder to the expected force range. The voltage outputs at the zero and full scale of the load must be noted. These endpoint values are very important in order to convert the voltages to force. The chart recorder gives a hard copy output of load versus deflection which is used to verify the results of the data acquisition program. The chart calibration is somewhat of an art and can only be mastered by experience. The two toggle switches labeled CHART and PEN must be positioned on. To calibrate, set the FULL SCALE LOAD to 500 lb. Then using the knob labeled ZERO, position the chart pen to the x-axis on the far left side of the graph paper (the x-axis is vertical, and the y-axis is horizontal while the paper is in the recorder). Push the button next to the knob. The pen should stay at zero. If not adjust the knob again to put the pen on zero. Continue this until the pen does not move off zero when the button is pushed. Next, push and hold the button under the CALIBRATION label. The pen will move to the right and should stop on the rightmost edge of the graph. (Full scale on the y-axis is ten inches, with a grid spacing of one-inch.) Most likely the pen will over or under shoot the edge. If this happens, turn the

knob (next to the button) while continuing to hold the button to bring the pen to the graph edge. Now, release the button, the pen should move back to the right and stop on zero. If it does not land on zero, repeat the entire process until the pen is calibrated to the zero and full scale. This is an iterative process. Now select 1000 lb on the FULL SCALE LOAD, and push the button under CALIBRATION. The pen should go half way across the graph paper. Continue selecting the loads and checking the calibration up to the desired load.

The preceding procedure was to calibrate for compression on the load cell. If tension is applied to the load cell (as in a tensile test), follow the same procedure. except the zero should be on the right side of the graph and full scale on the left side of the graph. Switch CHART off until ready to begin the experiment.

A.3.1 Setting the Chart Speed

The rate of paper advance can be set to a desired speed by repositioning the gears located inside the chart recorder. The chart recorder is on hinges and can be opened by releasing the locking lever labeled A behind the glass door. Swing open the chart recorder to reveal a matrix showing the combinations of gear positions and the associated speeds. Position the gears to the desired chart speed. A satisfactory chart speed is 10 inches per minute.

A.4 Starting the Experiment

The equipment is ready to start the experiment. To begin, first click the START/STOP button on the NI-DAQ control panel. The program is now ready to receive input data. On the Instron, switch CHART on to begin the chart recorder. Shut the small

door next to the SPEED CONTROL buttons. This is a safety interlock that allows the test machine head to travel. Press the UP button to cause the head to move up. As loads are applied to the test specimen, the chart and NI-DAQ screen should both plotting data.

Once the experiment is complete, press the STOP button on the Instron to stop the machine head travel. Switch CHART to off, and press ENTER on the keyboard to stop the data acquisition program. A new menu will appear on the screen. Position the cursor on the file name block and rename the file (with a unique name that describes the test) ensuring the extension is ".txt". The data is now saved and ready for processing. Press the ENTER key and click on QUIT to exit NI-DAQ.

A.5 Data Reduction

The file generated from the NI-DAQ program is a standard ASCII text file which can be read into a spreadsheet package. For completeness, this section describes how to read the text file into Microsoft Excel. which is used to process the raw data.

From the main window, open the Microsoft Word program. Click on FILE and select OPEN. Change the directory to C:\NIDAQDOS\DAQWARE. Click on LIST OF FILE TYPES and select *.txt. This should display the data file name previously saved. An icon will ask to convert the file, click OK. The data file should appear on the screen. Delete the first few lines of zero voltage readings keeping only one zero voltage reading (recall that the zero voltage should have been noted during calibration). From the EDIT menu click on SELECT ALL. The data should now be highlighted. From TABLE, select CONVERT TEXT TO TABLE. Two columns will appear. The first contains the test data, and the second is blank. To clear the second column, choose TABLE. then SELECT COLUMN, and press the delete key. Finally, from the EDIT menu, choose SELECT

ALL, then COPY. At this point, the file is saved in the buffer and ready for import to Excel.

After exiting Word and bringing up the Excel spreadsheet, select the EDIT menu and choose PASTE. The data should be displayed in the spreadsheet. The data is ready for processing.

Appendix B

Supporting Calculations

This appendix provides supporting calculations for Chapter 4. Specifically shown are the details of Equation 4.23, the numerical evaluation of the USDH steady state cutting force expression (Equation 4.41), and a comparison of the fully plastic torsion of a stiffener to the fully plastic bending moments of a stiffener, plate, and stiffener/plate combination.

B.1 Calculation of Displacements u_a and u_b

The calculations of the displacements given by Equation 4.23 are shown in this section. The geometry used in these calculations is shown in Figure B.1

Displacement u_a - The displacement u_a is given by

$$u_a = OA - OB. \quad (B.1)$$

The distance OA is known from the geometry and is given by

$$OC = \frac{\zeta}{\cos \theta}.$$

The distance OB is determined from geometry, and OC is the projection of OA through the angle α_2 , as

$$OB = \frac{\zeta}{\cos \alpha_1} \quad (B.2)$$

$$OA = \frac{\zeta}{\cos \theta \cos \alpha_2}$$

Substitution of (B.2) in (B.1) gives the displacement

$$u_a = \zeta \left(\frac{1}{\cos \theta \cos \alpha_2} - \frac{1}{\cos \alpha_1} \right) \quad (4.23a)$$

Displacement u_b - Referring to Figure B.2, let

$$x_1 = OE$$

$$x_2 = EC$$

$$y_1 = BE$$

$$y_2 = ED$$

$$\frac{\Delta}{2} = BD$$

From the geometry, u_b can be found by the expression

$$u_b = CD = \sqrt{y_2^2 + x_2^2}. \quad (B.3)$$

The lengths y_1 and y_2 are related by

$$\frac{\Delta}{2} = y_1 + y_2, \quad (\text{B.4})$$

where

$$y_1 = \frac{\zeta}{\cos \alpha_1} \sin \alpha_2 \quad (\text{B.5})$$

which upon rearrangement of (B.4) gives

$$y_2 = \frac{\Delta}{2} - \frac{\zeta}{\cos \alpha_1} \sin \alpha_2. \quad (\text{B.6})$$

The relation between x_1 and x_2 is

$$x_1 + x_2 = \frac{\zeta}{\cos \theta}. \quad (\text{B.7})$$

The length x_1 is found to be related to y_1 by

$$\frac{y_1}{x_1} = \tan \alpha_2. \quad (\text{B.8})$$

Substitution of (B.5) into (B.8), and then that result into (B.7) gives an expression for x_2 as

$$x_2 = \zeta \left(\frac{1}{\cos \theta} - \frac{\cos \alpha_2}{\cos \alpha_1} \right). \quad (\text{B.9})$$

Finally, substitution of (B.6) and (B.9) into (B.3) gives the displacement

$$u_b = \sqrt{\left(\frac{\Delta}{2} - \zeta \frac{\sin \alpha_2}{\cos \alpha_1}\right)^2 + \left(\zeta \left(\frac{1}{\cos \theta} - \frac{\cos \alpha_2}{\cos \alpha_1}\right)\right)^2} \quad (4.23b)$$

B.2 Evaluation of the USDH Steady-State Cutting Force Equation

The values of the various terms to get to the final result of Equation 4.41 are given in Table B.1. The final result is for the cutting of both plates of the USDH specimen. The intermediate values in the table are for only one deformed segment. The forces in bending and membrane are obtained by dividing through by the velocity, V . The input parameters are given as follows

Cell spacing:	$b = 41.7 \text{ mm}$
Wedge Width:	$B = 76.2 \text{ mm}$
Plate Thickness:	$t = 0.749 \text{ mm}$
Coefficient of Friction:	$\mu = 0.3$
Specific Work of Fracture:	$R = 650 \text{ N/mm}$

Table B.1 USDH Steady-State Cutting Force Equation Values.

Variable	$\theta=30^\circ$	$\theta=45^\circ$	Equation No.
Δ	17.25 mm	17.25 mm	4.16
ζ	29.88 mm	17.25 mm	4.17
α_1	16.1°	26.6°	4.17
α_2	13.9°	18.4°	4.17
u_a	4.44 mm	6.43 mm	4.23
u_b	4.47 mm	6.60 mm	4.23
u_η	3.34 mm	4.87 mm	4.26
r_1	7.49 mm	7.49 mm	4.48
r_2	2.25 mm	2.25 mm	4.48
ϵ_{ave}	0.073	0.131	4.47
σ_0	298 N/mm ²	318 N/mm ²	App C
F_b	815 N	870 N	4.20
F_{str}	497 N	1338 N	4.27
F_{sh}	569 N	887 N	4.31
F_p	1881 N	3095 N	4.34
F_f	977 N	929 N	4.33
$F_{concertina}$	3852 N	4023 N	4.32
F	19136 N	24142 N	4.41

B.3 Fully Plastic Torsion of the Stiffener and Bending of the Stiffener and Plate

This section estimates and compares the fully plastic twisting moment of a stiffener, and the fully plastic bending moment of the plate, stiffener, and plate/stiffener combination.

B.3.1 Fully Plastic Torsion of the Stiffener

The fully plastic torsion of a stiffener can be estimated using the sand heap analogy, Johnson and Mellor (1983). Figure B.2 shows the geometry of the stiffener and the shear stress, k , from the sand heap analogy. The actual shear flow around the corner near the flange/web joint is parabolic, but the twisting moment contribution in the shaded area is ignored since the moment arm and area are both small compared to the other sections.

The moment about the point O is expressed as

$$T_o = kA_I l_1 + 2kA_{II} l_2 + 2kA_{III} l_3 + kA_{IV} l_4 + 2kA_V l_5. \quad (B.10)$$

The moment arm from the origin, O , to the centroidal axis, \bar{y} , of each area section is found using the following relationship

$$\bar{y} = \frac{\sum \bar{y}_i A_i}{\sum A_i}. \quad (B.11)$$

The section areas are found from geometry to be

$$\begin{aligned} A_I &= \frac{t_f}{4} (2b_f - t_f) \\ A_{II} &= \frac{t_f^2}{4} \\ A_{III} &= \frac{t_f}{4} \left(b_f - t_w - \frac{t_f}{2} \right) \\ A_{IV} &= \frac{t_w^2}{4} \\ A_V &= \frac{t_w}{2} \left(b_w - \frac{t_w}{4} \right) \end{aligned} \quad (B.12)$$

and the moment arms are found using (B.11) as

$$\begin{aligned}
 l_1 &= \frac{\frac{t_f}{2} \left(b_f - \frac{t_f}{3} \right)}{(2b_f - t_f)} & l_4 &= \left(\frac{1}{2} t_f + b_w - \frac{t_w}{6} \right) \\
 l_2 &= \frac{1}{2} \left(b_f - \frac{t_f}{3} \right) & l_5 &= \frac{\frac{t_w}{4} \left(b_w - \frac{t_w}{3} \right)}{\left(b_w - \frac{t_w}{4} \right)} \\
 l_3 &= \frac{\frac{t_f}{4} \left(b_f - t_w - \frac{2t_f}{3} \right)}{\left(b_f - t_w - \frac{t_f}{2} \right)} & &
 \end{aligned} \tag{B.13}$$

Substitution of (B.12) and (B.13) into (B.10) results in an approximation for the fully plastic torsion of the stiffener as

$$T_o = k \left[\frac{3t_f^2}{8} \left(b_f - \frac{t_f}{3} \right) + \frac{t_f^2}{8} \left(b_f - t_w - \frac{2t_f}{3} \right) + \frac{t_w^2}{4} \left(\frac{1}{2} t_f + b_w - \frac{t_w}{6} \right) + \frac{t_w^2}{4} \left(b_w - \frac{t_w}{3} \right) \right]. \tag{B.14}$$

Now, taking the values for the stiffener from Table 2.4 and letting $k = \frac{\sigma_o}{\sqrt{3}} = \frac{314 \text{ N/mm}^2}{\sqrt{3}}$, Equation B.3 is evaluated to be $T_o = 4.9 \text{ Nm}$.

B.3.2 Fully Plastic Bending Moment of the Stiffener, Plate, and Stiffener/Plate Combination

The fully plastic bending moments of the stiffener and the stiffener/plate combination are calculated using the method described by Hughes (1988) in *Ship Structural Design*³.

Stiffener Only - The following describes the method to find the fully plastic bending moment:

First, the following quantities are calculated from the geometry of the stiffener:

$$\begin{aligned}C_1 &= \frac{A_w + A_f}{2A_w} \\C_2 &= C_1^2 - C_1 + 0.5 \\g &= C_1 b_w \\Z_f &= A_f (b_w - g + 0.5t_f) \\Z_w &= A_w b_w C_2\end{aligned}$$

The plastic section modulus for the stiffener is given as

$$Z_p = Z_f + Z_w.$$

Using this result, the fully plastic bending moment for the stiffener is

$$M_s = \sigma_y Z_p.$$

³ Section 16.1, page 510.

Letting the yield stress be $\sigma_y = 175 \text{ N/mm}^2$, estimated from the stress-strain curves in Appendix C, the fully plastic bending moment for the stiffener is $M_s = 84.3 \text{ Nm}$.

Plate Only - The fully plastic bending moment for the plate alone, with width b , is given as

$$M_p = \frac{2}{\sqrt{3}} \frac{\sigma_y t_p^2}{4} b,$$

which on substitution of the values gives $M_p = 6.2 \text{ Nm}$.

Stiffener/Plate Combination - The equations for the stiffener/plate section are given as

$$C_1 = \frac{A_p - A_w + A_f}{2A_p}$$

$$C_2 = C_1^2 - C_1 + 0.5$$

$$g = C_1 t_p$$

$$Z_f = A_f (b_w + g + 0.5 t_f)$$

$$Z_w = A_w (0.5 b_w + g)$$

$$Z_p = A_p t_p C_2$$

The fully plastic section modulus now has the plate section modulus added to give

$$Z_p = Z_f + Z_w + Z_p,$$

and the fully plastic bending moment for the plate/stiffener combination is $M_{s/p} = \sigma_y Z_p = 214.9 Nm$.

The results of the above calculations are summarized in Table B.2. Comparison of the four results shows that the plastic bending of the plate alone, and the plastic twisting of the stiffener alone are of the same order of magnitude. The plastic bending of the stiffener/plate combination is nearly two orders of magnitude higher than the torsion of the stiffener and bending of the plate, and nearly one order of magnitude higher than the bending of the stiffener.

This order of magnitude analysis shows that the stiffener and plate cannot be modeled independently, but must be modeled as a unit. The complex bending and twisting of the single hull specimens after cutting by a wedge proved to be beyond the scope of this thesis.

B.2 Fully Plastic Moments of Stiffener and Plate Structural Members.

Structural Unit	Plastic Moment (Nm)
Stiffener (Torsion)	4.9
Stiffener (Bending)	84.3
Plate (Bending)	6.2
Stiffener/Plate (Bending)	214.9

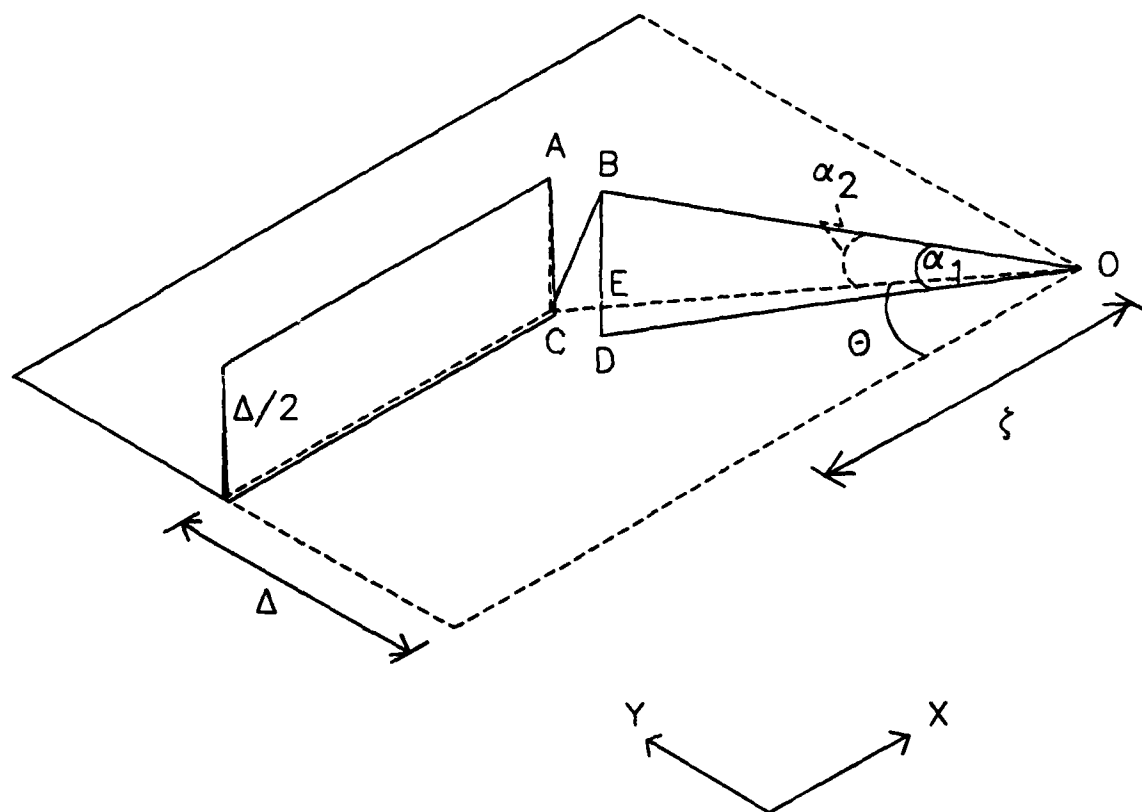


Figure B.1 Geometry for Calculation of Displacements u_a and u_b .

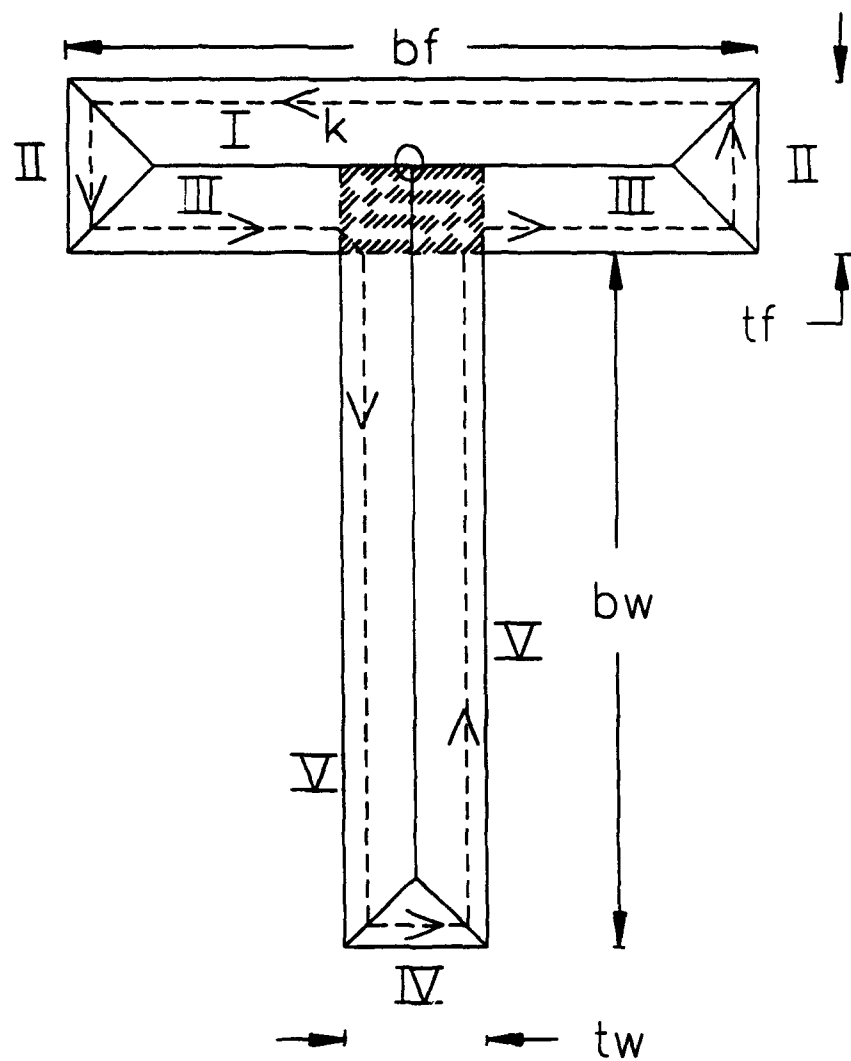


Figure B.2 Sand Heap Analogy for Stiffener.

Appendix C

Tensile Test Results

Tensile tests results are reported here for the three material thickness used in fabrication of the single and double hull models⁴. A total of twelve specimens were tested: four for each thickness with two each in the transverse and longitudinal direction to the roll axis. The tests were conducted in accordance with ASTM specification A370. The test specimen dimensions are shown in Figure C.1. The reported results include yield strength (YS), tensile strength (TS), percent elongation, and the accompanying engineering stress-strain curves, as shown in Table C.1 and Figures C.2 - C.13.

Table C.1 Tensile Test Specimen Properties.

Specimen No.	Thickness (mm)	Orientation (from roll axis)	0.2% YS (N/mm ²)	TS (N/mm ²)	% Elongation
1	0.749	0°	244.8	328.9	41.3
2	0.749	0°	180.0	329.6	41.0
3	0.749	90°	175.8	319.9	41.3
4	0.749	90°	176.5	319.2	39.4
5	1.130	90°	211.7	332.3	38.5
6	1.130	90°	213.1	334.4	37.3
7	1.130	0°	229.6	338.5	38.0
8	1.130	0°	207.5	333.7	38.5
9	1.829	0°	153.1	299.9	45.9
10	1.829	0°	137.2	280.6	45.8
11	1.829	90°	145.5	282.7	44.7
12	1.829	90°	146.2	282.7	45.0

Conversion Factor: 0.006895 (N/mm²) = 1 psi.

⁴ The work in this appendix was done in collaboration with P. Little.

The results of Table C.1 can be averaged for each thickness as shown in Table C.2.

Table C.2 Tensile Test Specimen Averaged Properties.

Thickness (mm)	Average 0.2% YS (N/mm ²)	Average TS (N/mm ²)	Average % Elongation
0.749	194.3	324.4	40.8
1.130	215.5	334.8	58.1
1.829	145.5	286.5	45.4

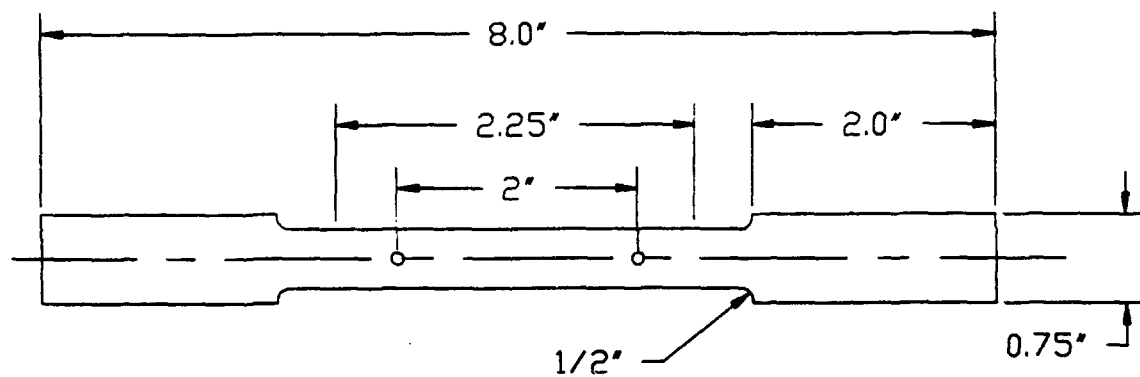


Figure C.1 ASTM A370 Flat Tensile Specimen.

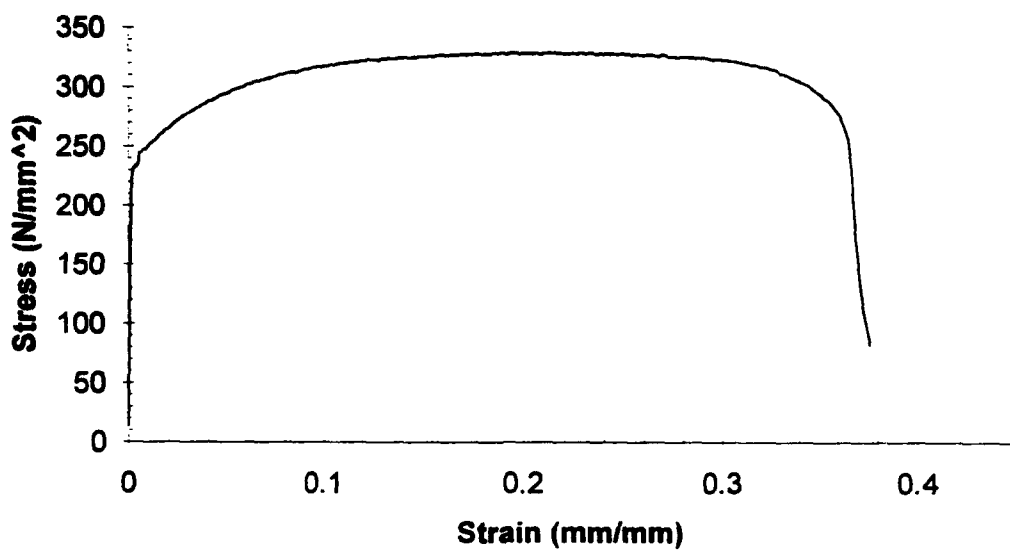


Figure C.2 Specimen 1 - Engineering Stress-Strain Curve
($t = 0.749$ mm, 0° from roll axis).

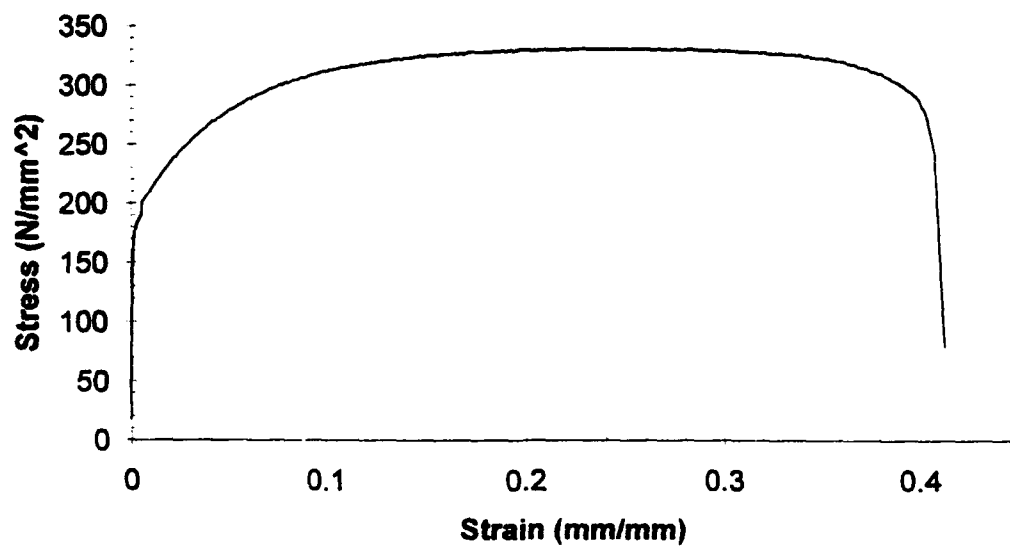


Figure C.3 Specimen 2 - Engineering Stress-Strain Curve
($t = 0.749$ mm, 0° from roll axis).

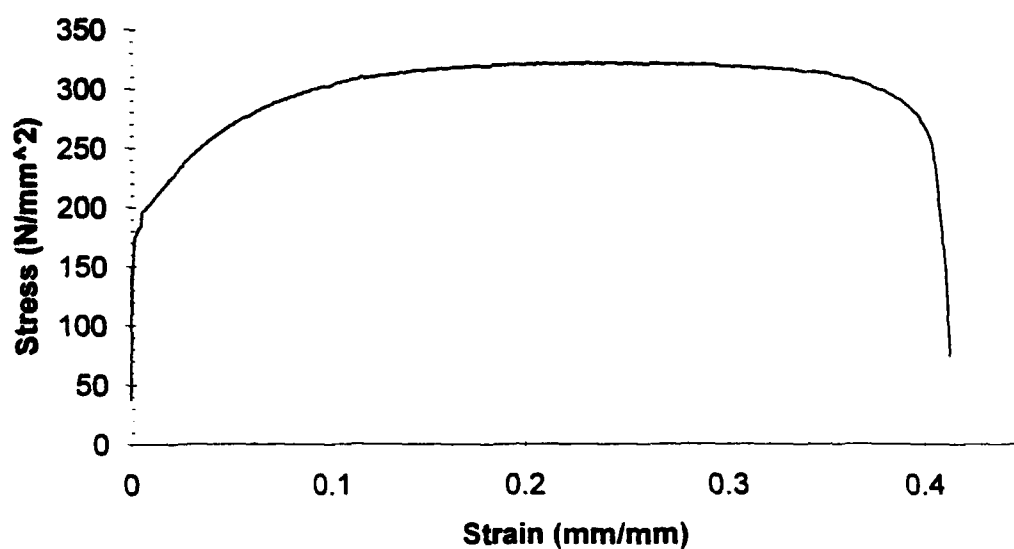


Figure C.4 Specimen 3 - Engineering Stress-Strain Curve
($t = 0.749$ mm, 90° from roll axis).

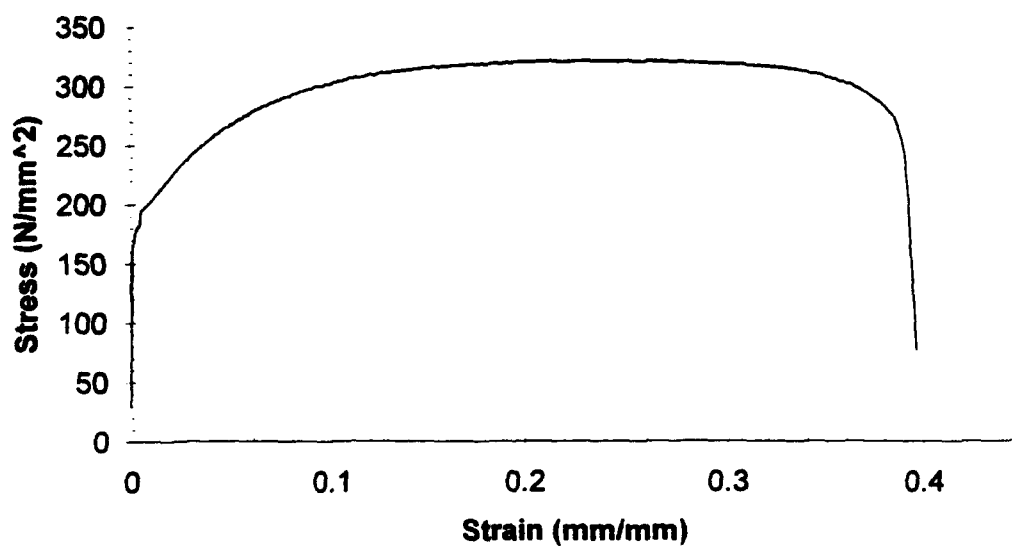


Figure C.5 Specimen 4 - Engineering Stress-Strain Curve
($t = 0.749$ mm, 90° from roll axis).

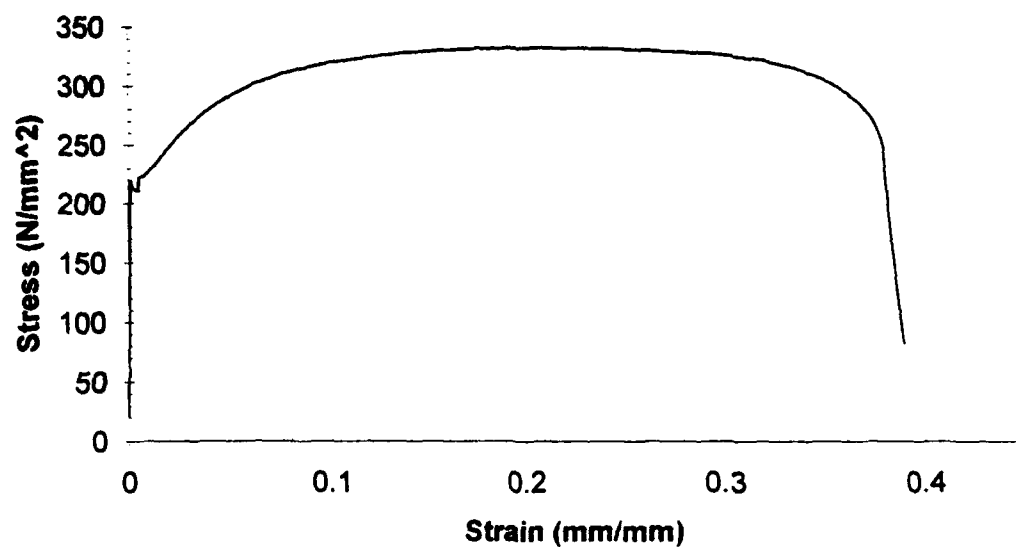


Figure C.6 Specimen 5 - Engineering Stress-Strain Curve
($t = 1.130$ mm, 90° from roll axis).

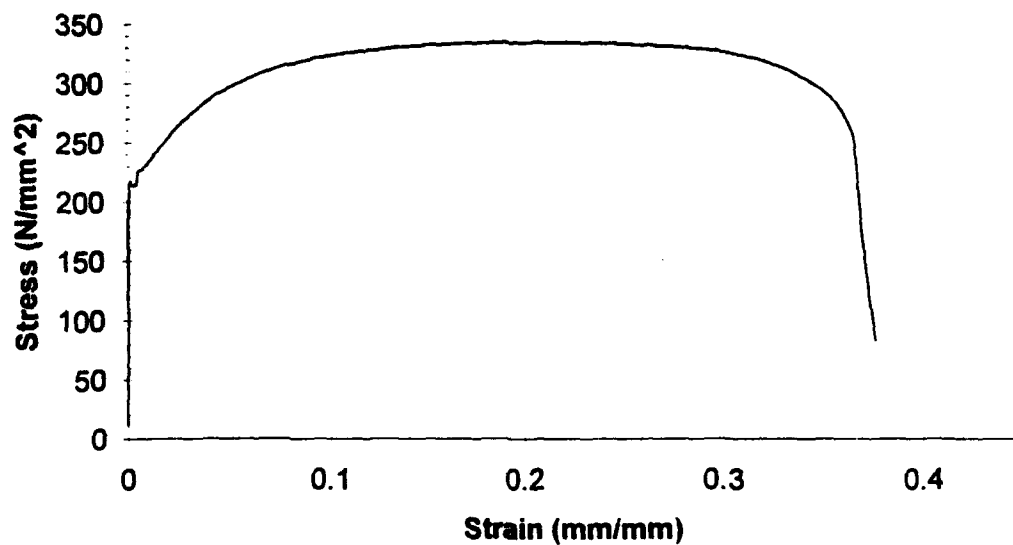


Figure C.7 Specimen 6 - Engineering Stress-Strain Curve
($t = 1.130$ mm, 90° from roll axis).

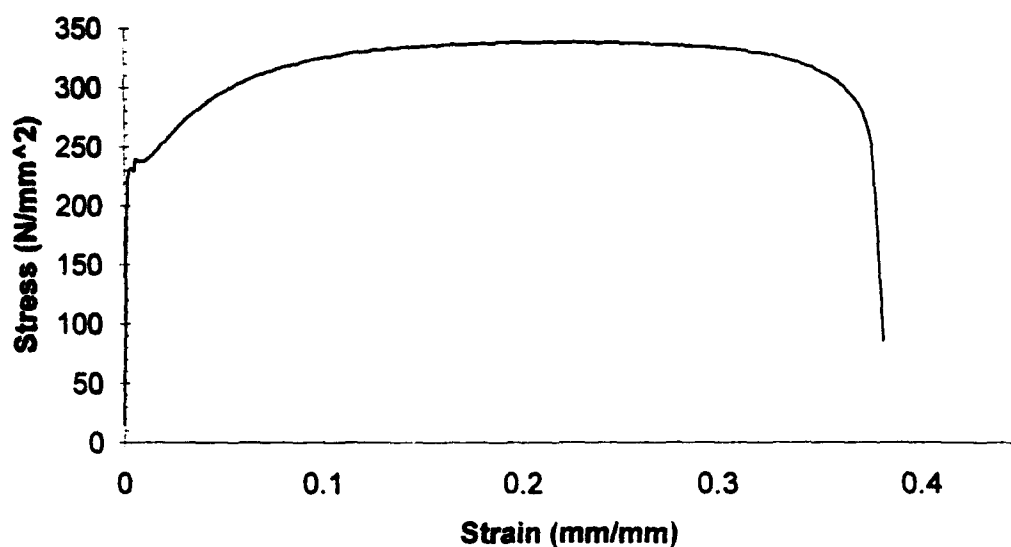


Figure C.8 Specimen 7 - Engineering Stress-Strain Curve
($t = 1.130$ mm, 0° from roll axis).

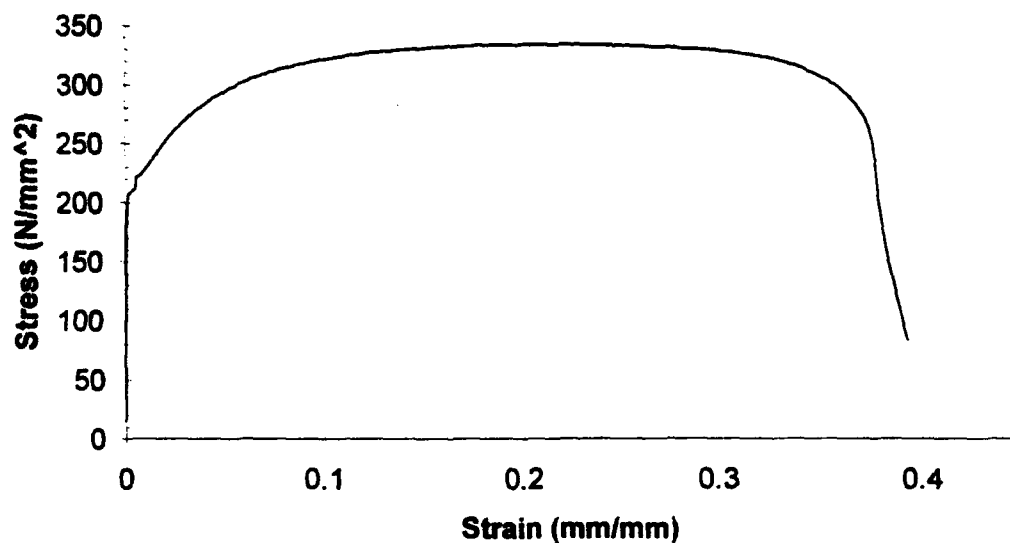


Figure C.9 Specimen 8 - Engineering Stress-Strain Curve
($t = 1.130$ mm, 0° from roll axis).

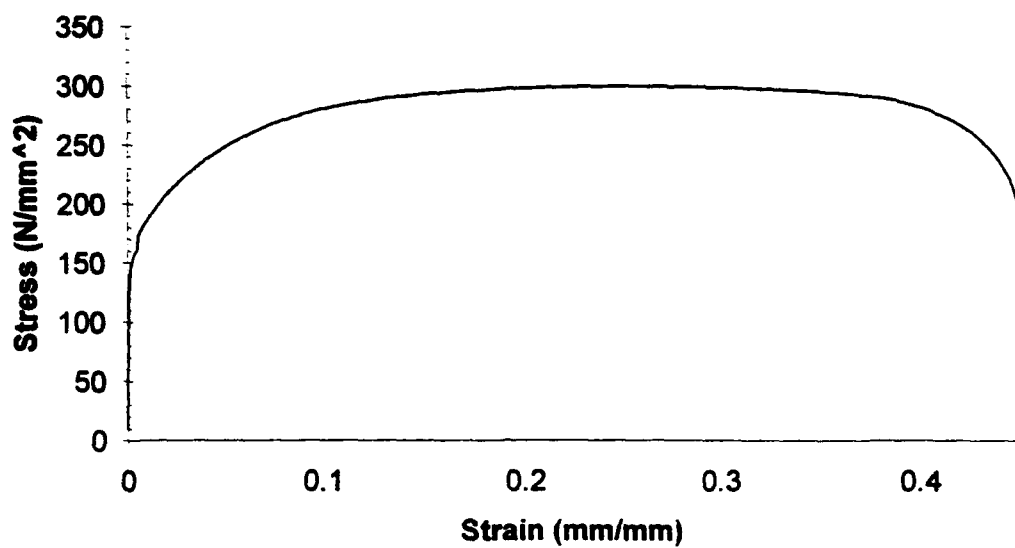


Figure C.10 Specimen 9 - Engineering Stress-Strain Curve
($t = 1.829$ mm, 0° from roll axis).

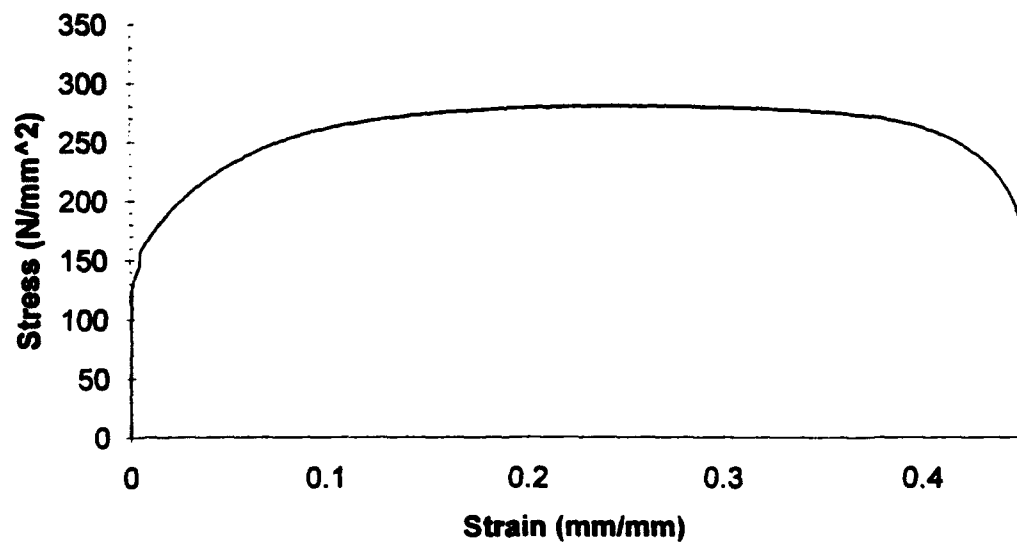


Figure C.11 Specimen 10 - Engineering Stress-Strain Curve
($t = 1.829$ mm, 0° from roll axis).

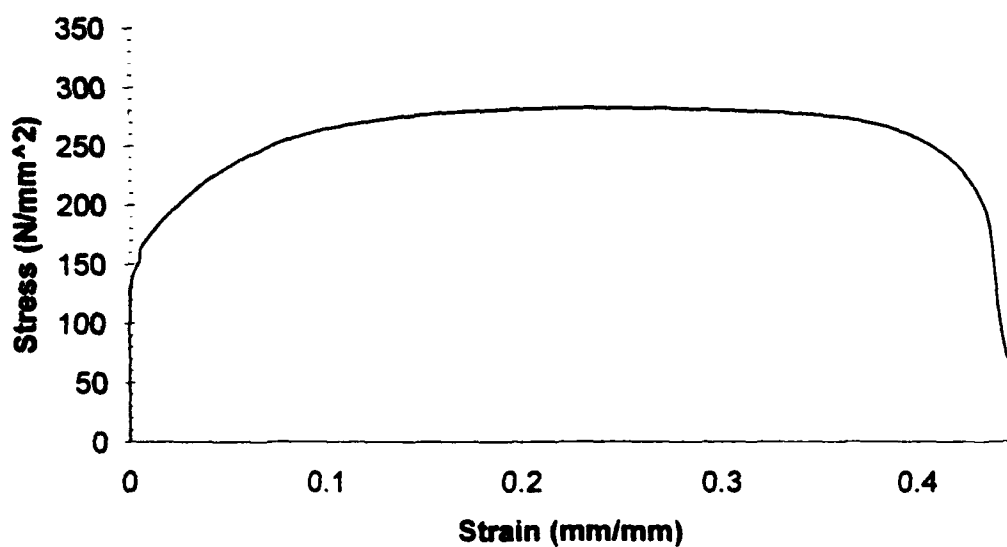


Figure C.12 Specimen 11 - Engineering Stress-Strain Curve
($t = 1.829$ mm, 90° from roll axis).

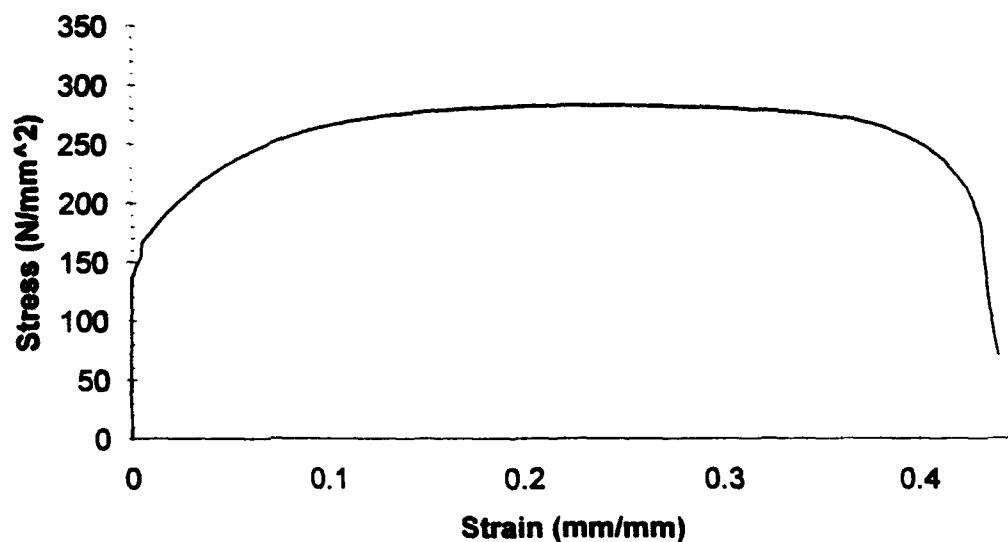


Figure C.13 Specimen 12 - Engineering Stress-Strain Curve
($t = 1.829$ mm, 90° from roll axis).

Appendix D

Lazy-T Weld Bend Tests

D.1 Purpose

This appendix provides information on Lazy-T weld bend tests conducted to investigate the strength of welds made using the electron beam welding (EBW) process. A secondary purpose of the tests was to provide information to assist in the development of full scale Lazy-T tests using material thicknesses commonly found in oil tanker design. The work in this appendix was done in collaboration with P. Little.

The Lazy-T test was suggested by McClintock (1994) as a means for testing T-joints in the web folding mode of deformation and fracture. Figure 5.1 illustrates the weld failure modes proposed by McClintock (1994). The strength of EBW T-joints was questioned when the EBW joints did not fail even when subject large deformations during the scale model testing.

D.2 Limit Load Calculation

Figure D.1 shows a free body diagram for the T-joints tested. The load, P , is applied by the crosshead of a universal testing machine. Teflon tape was positioned under points A and B to minimize sliding friction.

Prior to conducting tests, a calculation of the limit load was made to determine the test equipment size needed. From the geometry of the problem, the following is determined as

$$\theta = \tan^{-1}\left(\frac{b_f}{2h_w}\right). \quad (D.1)$$

Summing moments about point *A* gives;

$$P_B \frac{h_w}{\cos \theta} - P b_f \sin \theta = 0. \quad (D.2)$$

Defining *b* as the depth of the specimen (into the page), σ_{TS} as the tensile strength of the material and t_w as the thickness of the web gives the fully plastic bending moment

$$M_p = \frac{b \sigma_{TS} t_w^2}{4}. \quad (D.3)$$

Referring to the geometry in Figure D.2 where μ is the coefficient of sliding friction, the bending moment due to web folding at the weld joint is

$$M = P_B h_w \cos \theta - \mu P_B h_w \sin \theta. \quad (D.4)$$

Setting the fully plastic bending moment, Equation D.3, equal to the bending moment at the weld joint, Equation D.4, results in

$$P_B h_w (\cos \theta - \mu \sin \theta) = \frac{b \sigma_{TS} t_w^2}{4}. \quad (D.5)$$

Substituting (D.2) into (D.5) and solving yields the limit load

$$P_{\text{limit}} = \frac{\sigma b t_w^2}{4 b_f \sin \theta \cos \theta (\cos \theta - \mu \sin \theta)}. \quad (D.6)$$

D.3 Test Results

A total of three t-stiffeners were tested. Table D.1 lists the dimensions of the specimens tested. For the calculations, values of $\sigma_{TS} = 324 \text{ N/mm}^2$ and $\mu = 0.3$ were used.

Table D.1 T-Stiffener Dimensions.

Specimen	h_w (Inches)	b_f (Inches)	Depth, b (Inches)	Thickness (Inches)	Calculated Limit Load, N
1	1.644	1.5	0.482	0.029	47.7
2	1.644	1.5	0.465	0.029	46.0
3	1.647	1.5	0.499	0.029	49.4

Testing was performed on a Instron 4201 universal testing machine in the Remergence Laboratory at MIT. Based upon the calculated limit load, the 500 N load cell was selected for use. Unfortunately, it was inoperative and the tests were conducted with the 5 kN load cell instead. A total three Lazy-T tests were performed. The force displacement graphs are included as Figure D.3 through D.5.

During the Lazy-T tests, the crosshead direction was reversed several times in order to observe the effect of friction. The results of the reversal are depicted in Figures D.3 through D.5. As shown, there is evidence of 'sticking' during the crosshead motion. In spite of the sticking evident in the hysteresis loops, the contribution of sliding friction was determined to be not significant.

As shown in the figures the force starts to rise sharply when the crosshead displacement exceeds 25 mm. This coincides with the flattening of the T-joint. The same

feature was observed on all tests, namely, the weld did not fail. A close examination of the crushed samples indicated the bending took place in the web.

D.4 Lazy-T Test Conclusions

Several conclusions were drawn from the Lazy-T testing. First, Equation D.6 provided an estimate of the limit load which was within 20% of that observed experimentally. Second, any welded joint should be strong enough so that the deformation occurs in the base metal, not the weld itself. In this case, EBW exhibited sufficient strength since the deformation occurred in the web on all tests. For future planning of full-scale Lazy-T tests, it appears as if friction is not a significant factor provided steps are taken to minimize its effect. The sticking observed during the compliance tests and in the hysteresis loops may be due to off center loading. An alternative may be the Lazy-L test, where the flange is trimmed at the weld joint and the legs are of equal length. The loading on this type of specimen would be symmetric throughout the test. Finally, the analysis can be extended so that the theoretical load is calculated as a function of cross-head displacement.

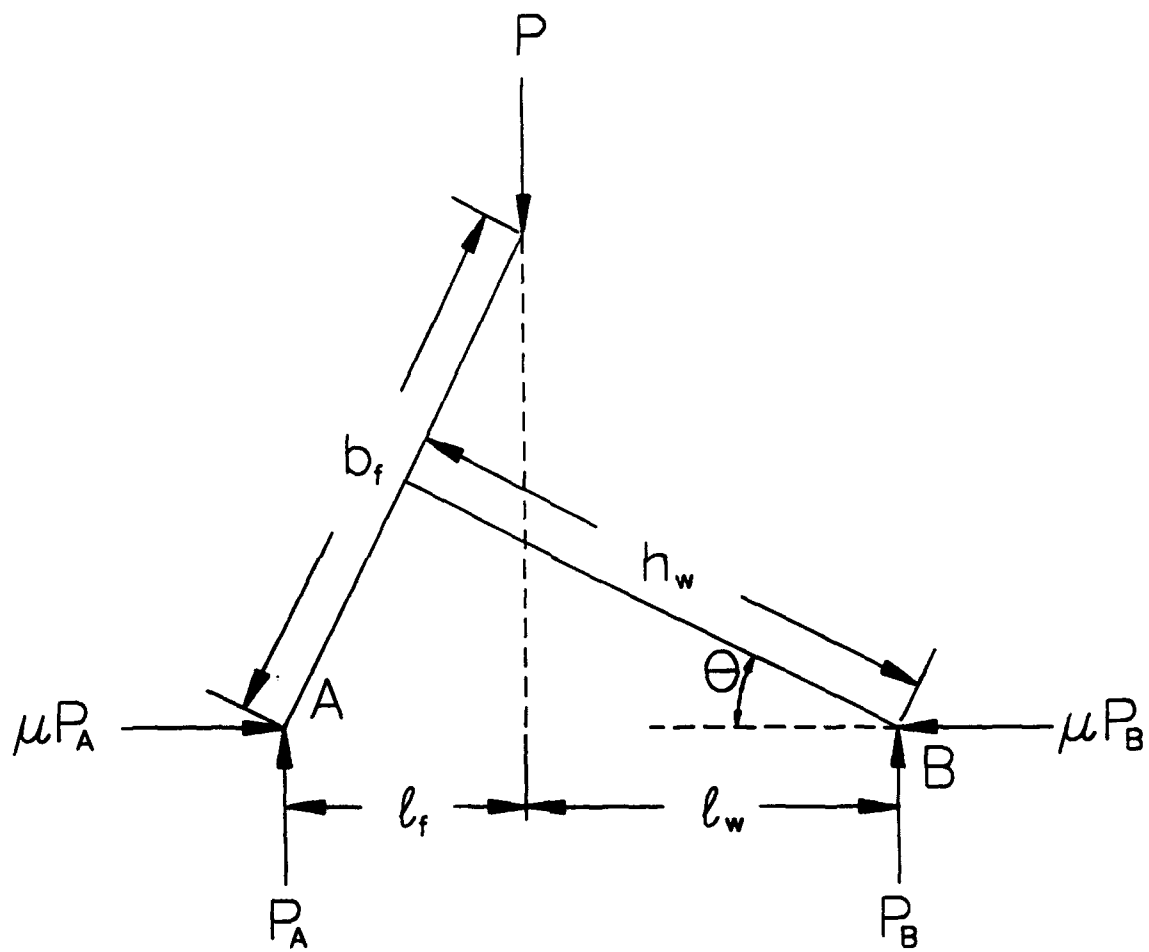


Figure D.1 T-Stiffener Geometry and Free Body Diagram.

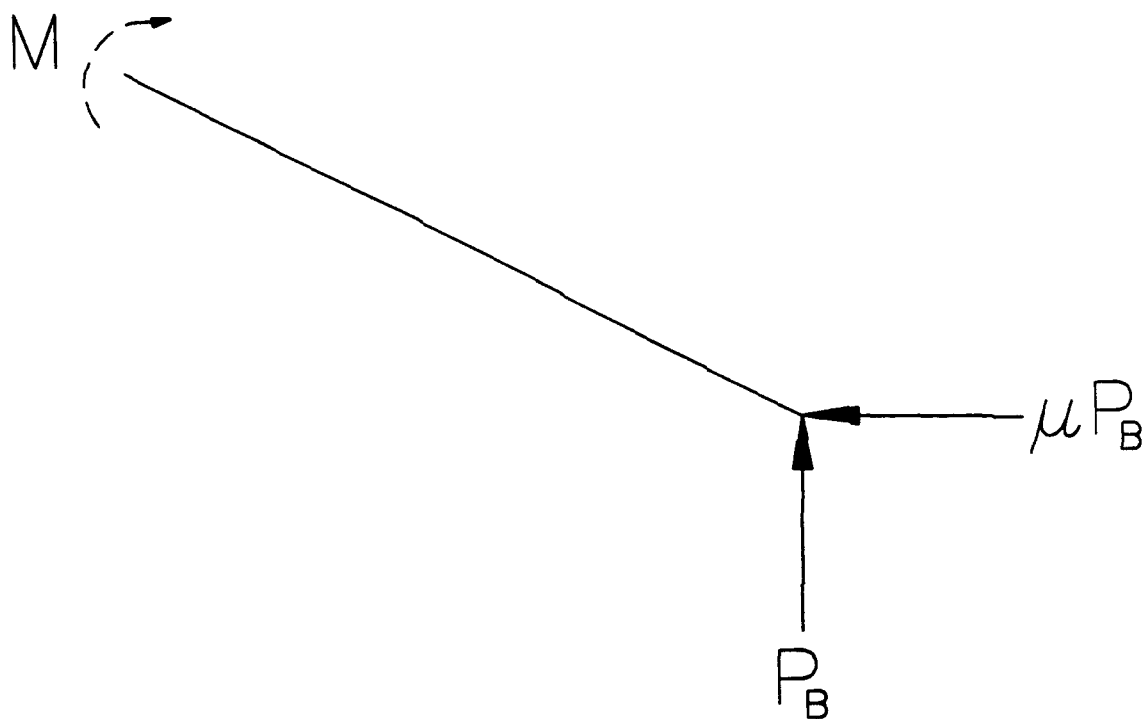


Figure D.2 Bending Moment at the Web Joint.

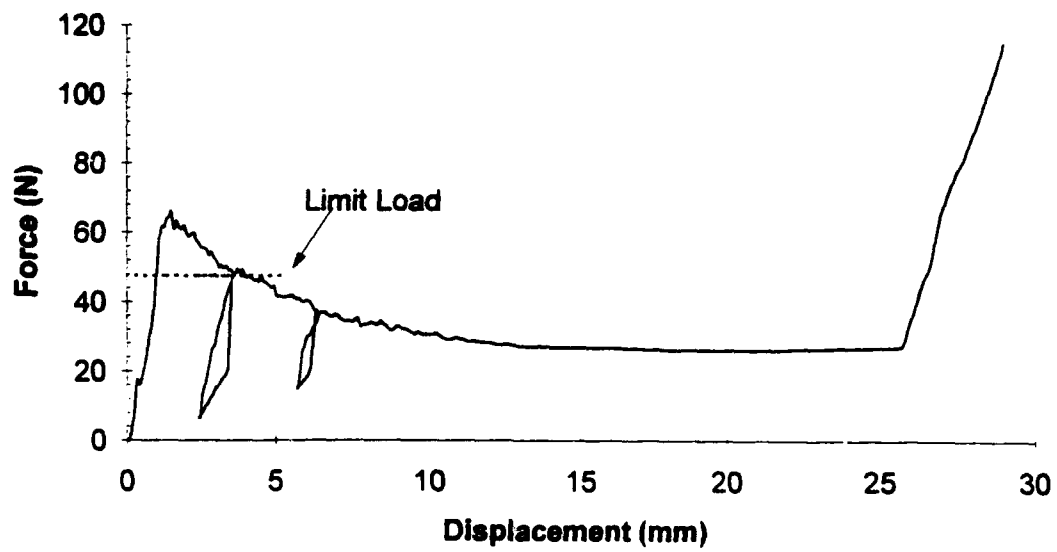


Figure D.3 Lazy-T Test Results for Specimen #1.

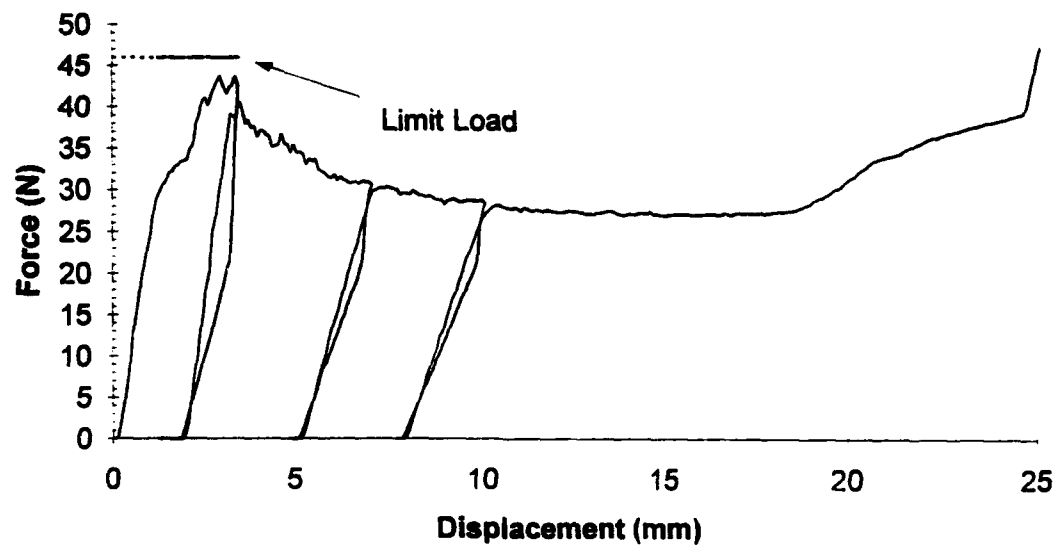


Figure D.4 Lazy-T Test Results for Specimen # 2.

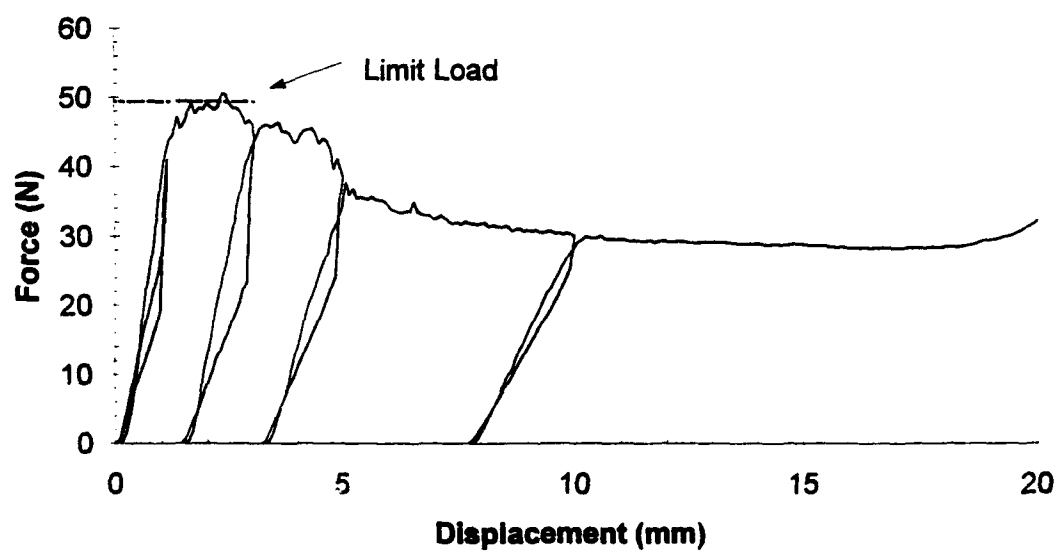


Figure D.5 Lazy-T Test Results for Test #3.